AN ANALYTICAL MODEL OF NON-UNIFORMLY DOPED SILICON SOLAR CELL FOR ALL ILLUMINATION CONDITION

A thesis submitted to the Department of Electrical and Electronic Engineering
Of
Bangladesh University of Engineering and technology
In partial fulfillment of the requirements for the degree of
MASTER OF SCIENCE IN ELECTRICAL AND ELECTRONIC ENGINEERING

by
Bishwajit Debnath

Roll No. 0412062256 F
M. Sc. Engineering (EE)

DEPARTMENT OF ELECTRICAL AND ELECTRONIC ENGINEERING
BANGLADESH UNIVERSITY OF ENGINEERING AND TECHNOLOGY
August, 2014

APPROVAL

The thesis titled "**An Analytical Model of Non-Uniformly Doped Silicon Solar Cell for All Illumination Condition**" submitted by **Bishwajit Debnath**, Roll No. **0412062256 F**, Session: **April 2012** has been accepted as satisfactory in partial fulfillment of the requirement for the degree of Master of Science in Electrical and Electronic Engineering on 10th August, 2014.

BOARD OF EXAMINERS

1. Dr. Md. Ziaur Rahman Khan

Professor
Department of Electrical and Electronic Engineering
Bangladesh University of Engineering and Technology,
Dhaka-1205, Bangladesh

Chairman
(Supervisor)

2. Dr. Taifur Ahmed Chowdhury

Professor and Head of the Department
Department of Electrical and Electronic Engineering
Bangladesh University of Engineering and Technology,
Dhaka-1205, Bangladesh

Member
(Ex-officio)

3. Dr. Sharif Mohammad Mominuzzaman

Professor
Department of Electrical and Electronic Engineering
Bangladesh University of Engineering and Technology,
Dhaka-1205, Bangladesh

Member

4. Dr. Mohammad Mojammel Al Hakim

Associate Professor,
Department of Electrical and Electronic Engineering
East West University,
Dhaka-1205, Bangladesh

Member
(External)

DECLARATION

It is hereby declared that this thesis or any part of it has not been submitted elsewhere for the award of any degree or diploma. Any material reproduced in this project has been properly acknowledged.

BISHWAJIT DEBNATH

Roll No: 0412062256 F

ACKNOWLEDGEMENT

I would like to express my earnest gratitude to my thesis supervisor Dr. Md. Ziaur Rahman Khan, Professor, Department of Electrical and Electronic Engineering, BUET, for his insightful suggestions, enthusiastic support and continuous help throughout the entire thesis work. I want to thank him for spending many hours with me in discussion about my research. I am also grateful to him for offering me the perfect balance of freedom and guidance. His passion for research will always be an inspiration to me.

I also want to thank my friend M. M. Chowdhury for his valuable suggestions. I am grateful to him for those hour-long, over-the-phone conversations. My special thanks goes to my brother, Topojit Debnath for helping me throughout this research endeavor. I want to thank him for his stimulating discussions about this research.

I also thank the members of my thesis committee: Professor Dr. Sharif Mohammad Mominuzzaman, Professor Dr. Taifur Ahmed Chowdhury, and Dr. Mohammad Mojammel Al Hakim, for their feedback on my work. Their kind suggestions have improved this thesis.

I want to acknowledge the renowned authors in the analytical research of solar cell for their published articles, journals and books. My thanks goes to BUET Research Library and Departmental Library for providing me numerous thesis papers and journals.

I am expressing my heartiest gratitude to my parents for their unconditional support; without their kindness, it was not possible to even start this research. Thanks to my well-wishers, colleagues and friends who inspired me various ways by their appreciations.

Bishwajit Debnath
August, 2014

ABSTRACT

A mathematical model of a non-uniformly doped silicon solar cell for all illumination condition has been developed. The drift-diffusion equation has been solved under low injection approximation for the derivation of the model. The model is iteration-free and integration-free, so it offers an elegant way to study the wide variation of several transport parameters, their individual contributions and interdependence. This analytical expression can successfully describe the mobility and lifetime variation, variation of surface recombination, positional dependence of parameters, effect of biasing, the contribution from dark and light response, and the response from standard terrestrial solar spectrums. For the validation of the derived model, a COMSOL Finite Element Model of solar cell has been developed. Along with that, a physically-based (TCAD) model in Silvaco/ATLAS is constructed for checking the results. The proposed model is in good agreement with both of the numerical models. The model is further improved so that the same model can also analyze the effect of individual wavelength, the addition of multiple emitter/base layers, and the inclusion of other non-uniform doping variation. The solution even works for non-Silicon photovoltaic materials, when the material properties are tailored properly. All the aforementioned effects and transport physics have been aggregated in a compressed expression, but with an added complexity of Bessel and Hypergeometric function. This analytical model can be helpful in optimizing solar cell designs by providing direct relationship of the physics with the device dimensions.

TABLE OF CONTENTS

LIST OF FIGURES

LIST OF TABLES

LIST OF SYMBOLS

λ = Wavelength (nm)

α = Exponential Doping gradient: $N = N_0 \exp(-\alpha x)$ (unitless)

α_{Si} = Absorption Coefficient (m^{-1})

n, p = Excess Minority Carrier Density in p- and n-type semiconductor, respectively (m^{-3})

D_n, D_p = Diffusion coefficient for electron and hole, respectively (m^2s^{-1})

μ_n, μ_p = Mobility for electron and hole, respectively (m^2/vs)

τ_n, τ_p = Minority carrier lifetime for electron and hole, respectively (s)

S_n, S_p = Surface recombination velocity for electron and hole, respectively (ms^{-1})

L_n, L_p = Diffusion length for electron and hole, respectively (m)

N_d, N_a = Density of ionized donor or acceptor respectively (cm^{-3})

N = Density of ionized impurity (either donor or acceptor) (cm^{-3})

$N_{ph}(\lambda)$ = Monochromatic photon flux ($cm^{-2}s^{-1}\mu m^{-1}$)

x = Distance from the top surface, where light is exposed (μm)

z = Variable transformation of x,
$z = \exp[-\alpha(m+k)x/2]$

X_j = Distance from the light exposed surface to the p-n junction depletion edge (μm)

X_E = Distance from the light exposed surface to the interface between region 1 and region 2 of emitter (μm)

$J_{n\text{-Drift}}$, $J_{p\text{-Drift}}$ = Drift component of current density for electron and hole, respectively ($\mathrm{Am^{-2}}$)

$J_{n\text{-Diff}}$, $J_{p\text{-Diff}}$ = Diffusion component of current density for electron and hole, respectively ($\mathrm{Am^{-2}}$)

$J_{n\text{-Totol}}$, $J_{p\text{-Totol}}$ = Total current density for electron and hole, respectively ($\mathrm{Am^{-2}}$)

$J_{n\text{-Drift}}(\lambda)$, $J_{p\text{-Drift}}(\lambda)$ = Drift component of monochromatic current density for electron and hole, respectively ($\mathrm{Am^{-2}\mu m^{-1}}$)

$J_{n\text{-Diff}}(\lambda)$, $J_{p\text{-Diff}}(\lambda)$ = Diffusion component of monochromatic current density for electron and hole, respectively ($\mathrm{Am^{-2}\mu m^{-1}}$)

$J_{n\text{-Total}}(\lambda)$, $J_{p\text{-Total}}(\lambda)$ = Total monochromatic current density for electron and hole, respectively ($\mathrm{Am^{-2}\mu m^{-1}}$)

V = Applied voltage across the cell (V)

E = Strength of Electric field ($\mathrm{Vm^{-1}}$)

E_G = Energy Band gap (eV)

q = Electronic Charge = 1.6×10^{-19} (A·s)

k_B = Boltzmann Constant =1.38×10^{-23} ($\mathrm{m^2\ kg\ s^{-2}\ K^{-1}}$)

h = Planck's constant = 6.626×10^{-34} (J.s)

c = Velocity of light = 3×10^{8} ($\mathrm{ms^{-1}}$)

T = Absolute temperature (K)

V_T = Thermal voltage = k_BT/q (V)

a_i = Coefficient of approximated generation, $G(x) = \Sigma\, a_i \exp(-b_i x)$ ($\mathrm{m^{-3}s^{-1}}$)

b_i = Coefficient of approximated generation, $G(x) = \Sigma\ a_i \exp(-b_i x)$ (m^{-1})

K = Parameter in empirical equation of lifetime: $\tau = KN^{-k}$ ($cm^{-6}s$)

k = Parameter in empirical equation of lifetime: $\tau = KN^{-k}$ (unitless)

M = Parameter in empirical equation of mobility: $\mu = MN^{-m}$ ($cm^{-0.86}V^{-1}s^{-1}$)

m = Parameter in empirical equation of mobility: $\mu = MN^{-m}$ (unitless)

f = Coefficient in expression of BGN (unitless)

LIST OF ACCRONYM

AM	Air Mass
ARC	Anti-Reflection Coating
ASTM	American Society for Testing and Materials
BGN	Band Gap Narrowing
BSF	Back Surface Field
DF	Drift Field
EHP	Electron-Hole-Pair
EQE	External Quantum Efficiency
FEM	Finite Element Method
FF	Fill Factor
FSF	Front Surface Field
FSRV	Front Surface Recombination Velocity
IBC	Interdigitated Back Contact
MPP	Maximum Power Point
PDE	Partial Differential Equation
PV	Photovoltaics
QE	Quantum Efficiency
QNQE	Quasi-Neutral Quasi-Equilibrium
QT	Quasi-Transparent
SRH	Shockley-Read-Hall
SRV	Surface Recombination Velocity
TCAD	Technology Computer Aided Design
TCO	Transparent Conductive Oxide
T	Transparent (model)

CHAPTER 1

INTRODUCTION

1.1. Introduction

An accurate and closed-form analytical or semi-analytical expression for the minority carrier concentration and current in solar cell has been searched over a long time [1-8]. Quasi-neutral silicon regions have been the subject of extensive investigation, due to its relevance in determining the electrical behavior of many photovoltaic and bipolar devices. For example, it is well established that the minority-carrier injection and storage into the heavily doped emitter may strongly affect dc as well as transient device performance. This holds particularly true for modem polysilicon bipolar transistors, where the minority-carrier current injected into the emitter represents the dominant component of the base current.

An extensive study of minority carrier profile is essential for successful understanding of the performance and efficiency of the solar cell [9, 10]. The dark and illumination current-voltage characteristics, which can be calculated from the carrier concentration, determine the overall behaviour of the solar cell. To predict the performance of a semiconductor device, the analytical and numerical models has been very reliable tools, as well as in providing an elegant alternative to costly experimental procedures. An obvious step in modelling solar cell is to analyse the transport phenomena of minority carrier [6] to obtain the saturation & collection current densities as a function of doping profile and surface recombination velocity. As the understanding of heavily doped semiconductors has gradually evolved, the transport properties of minority carriers injected into heavily doped emitters and other types of semiconductor devices has been extensively studied. For a non-uniformly doped emitter, heavy doping effects, such as bandgap narrowing, Auger lifetime, and minority-carrier diffusion, all becomes position dependent. Thus an intuitive understanding of the minority-carrier transport becomes complex. Besides, the presence of minority carrier recombination greatly complicates the situation to the point where, in spite of decades of effort, no completely general and mathematically-compact solution for the emitter and base region has been found that can offer a compromise between accuracy and analytical simplicity.

There has been several attempts though, to propose general analytical models that can use full-dependency of the transport parameters (e.g. lifetime, mobility, and bandgap narrowing), are simple enough for transistor design, can predict both emitter and base current, can retain a direct functional dependence of the transport parameters on impurity concentration in their formulation. It is advantageous to keep general functional forms for the transport parameters because these parameters are known to be very dependent upon process conditions, doping variation, and of course, the semiconductor material. Quite a number of authors have resorted to different simplifying assumptions that result in approximated analytical solutions. These models can describe minority-carrier transport in highly doped emitter region, in spite of the inherent complexity and the failure of these approximations outside the valid zone. Certainly, these approximations are the weakness towards achieving one unified analytical model.

On the other hand, obtaining a one dimensional numerical solution for low level injection, using basic numerical techniques [11] and considering today's widely available computing power, is essentially a trivial exercise. Simple, extremely efficient numerical models [12-14] are available that can provide solutions in very short computational time. But, analytical expressions present an advantage over numerical approaches by providing insight into the physics and electrical behavior, and by presenting an elegant way of device optimization. Unlike numerical simulation, the mathematical analysis offers an excellent means to study the effects from specific contributions, which can be invaluable in computer aided design. Besides, the analytical modelling has added advantages of faster calculation time and no convergence issues [15]. Along with that, the search for analytic solutions, which can provide engineers and scientists with an accurate "mental model", is more appealing in quantitatively and qualitatively interpreting experimental results, proposing more robust equivalent circuits and improving existing solar cell designs.

1.2. Literature Review

The difficulty in developing analytical model for non-uniformly doped solar cell arises from the fact that the minority transport parameters, specifically mobility, lifetime and band structure become dependent on position. Incorporation of these non-linear dependencies in the continuity equation and the minority carrier current equation makes the analysis intractable. Hence, numerical modelling has become a common approach for describing the behaviour of minority carriers in solar cells. Though numerical model of solar cell [16, 17], TCAD-based models [13, 14, 18-21] and efficient computer codes like PC-1D [12], AMPS [22] can address the photovoltaic physics reliably, a complete analytical model has no alternatives to understand the physical phenomena and to gain more comprehension for designing.

Several authors have attempted to analytically solved the minority carrier transport taking into account the position dependencies under dark condition [6, 15] and illuminated conditions [2]. In these works, they have used several physical assumptions [23-25] to simplify the functional dependence on doping profile.

Taking the assumption of doping-independent diffusion coefficient and neglecting drift component, Dumke [23] has proposed a Hermite polynomial expression for Gaussian profile. This hypothetical simplification results in inappropriate analytical solution since the approach considers only the diffusion mechanism due to the gradient of minority carrier concentration. In practical device, the induced electric field arising from the doping gradients and band gap narrowing is also a significant factor on device performance.

de Graff *et al.* [26] has considered the band gap narrowing due to high doping concentrations, doping-dependent Auger lifetime, built-in electric field, and finite surface-recombination velocity at the emitter contact. They included field dominant and diffusion dominant components in the emitter, but their expressions are based on computer simulation.

Amantea [24] took similar approach to [26] by dividing the emitter region in specific sections and solved the transport equations as boundary value problem which avoids the need for iteration. This solution differs from previous results by showing exactly when Auger recombination must be included in the analysis. Effects such as Shockley-Read-Hall (SRH) recombination, Auger recombination, bandgap narrowing, graded impurity profile, and position-dependent mobility have been included in that study. This analytic model is developed by using approximate models of the physical effects and by applying a variation of the regional-approximation method [27]. The emitter is divided into two separate regions: a field-dominated region adjacent to the junction and a diffusion-dominated region adjacent to the surface. In diffusion dominated region, they assumed constant diffusion coefficient, constant SRH and approximated the impurity profile by piecewise exponential grades near the surface. Besides, this model has another conspicuous limitation that it is a model for dark current (basically for bipolar transistor) and hence, does not apply for solar cell under light.

Assuming a thin and transparent emitter, Shibib *et al.* [28] proposed another analytical model, including majority-carrier degeneracy and finite surface-recombination velocity. They assumed *rigid-band approximation* that indicates to the bandgap narrowing without changing the parabolic dependence on energy of the density of states. They also considered *transparent approximation* which is valid for shallow emitter junction only. For this assumption, the minority carriers are assumed to be able to cross the quasi-neutral emitter without appreciable bulk recombination and, recombine only at the emitter surface. This assumption of infinite carrier lifetime is acceptable [29, 30] for very thin solar cell with high recombining contact. Hence, the applicability of their model is limited to specific p-n structure under dark condition, provided that the emitter recombination is low enough for the Auger process to dominate over the Shockley-Read-Hall process.

Later, Fossum *et al.* [31, 32] improved the analytical model by dividing the emitter into two or three regions: in first region, BGN, Auger recombination and Fermi-Dirac Statistics are considered; in second region, Boltzmann statistics and negligible BGN are considered; and with very high surface doping density, the third region is considered opaque to minority carriers. They considered diffusion-dominant current near the surface like [24], where effective doping is constant and the drift-dominant current at base-emitter junction, where the doping concentration gradient is large. Along with all that approximations, they have also taken “field-free” approximation, which they claim to be the basis for their model [32]. Hence, the net "effective" electric field acting on minority carriers (in the heavily doped or gradient-doped region) is assumed small enough so that the carriers flow mainly by diffusion. This assumption certainly makes this model invalid for drift-field solar cell.

The Transparent (T) Model in [28, 32] has been revisited by other authors [33, 34] taking the advantage from "no bulk recombination" approximation. Later, the T model is improved by del Alamo and Swanson [11] by incorporating the bulk recombination effect on the distribution of minority carrier. Their version of Quasi-Transparent (QT) analytical model offers a fast converging numerical method of calculating excess minority carrier density. QT model becomes increasingly inaccurate as the magnitude of bulk recombination increases with respect to the surface recombination. This situation occurs when the overall doping level or emitter thickness increases.

Selvakumar [10, 25] derived the analytical solution by using special functional dependence. The success of [10] is that a close form solution is presented, which crucially depends on the assumed empirical relationship of carrier lifetime.

So far, the objective of these abovementioned models was to develop a compact expression by solving the transport equations directly. But, along with them, another group of authors has been working on iterative approach of solving the drift-diffusion equations. Park *et al.* [15] presented a general closed-form analytical solution of the minority-carrier transport equations for non-uniformly doped emitter. Their solution is in the form of a multiple integral series and applicable for heavy doping profile and for any value of surface recombination velocity. Moreover, by truncating higher order terms, they simplified the analytical solution as known as three lowest-order approximations: the zeroth-order quasi-neutral quasi-equilibrium approximation (QNQE), and the 1st-order and 2nd-order approximations. The shortcoming of this model is that it needs at least two iterations to get accurate results [15]. Moreover, their model is rife with nested integration that does not give direct relationship with the transport parameters, rather makes the model obscure and certainly, it is not in compact form.

Rinaldi [7] extended the iterative and integral solution [6, 15] and rigorously obtain a new succession of approximate expressions for the minority-carrier current. As a solution of transport equations, that work also contain multiple integral asymptotic series, which is not in closed form and only accurate after certain number of iteration.

Verhoef *et al.* [8] has developed a complete closed-form expression for minority carrier transport by proposing new empirical expression of minority carrier mobility and lifetime; but the expression is developed excluding the generation rate in the transport equations, rather focusing on evaluating the dark current of solar cell.

Not to mention that, these previous models are neglecting sunlight in their derivation. They are already complex in nature, even without the inclusion of solar spectrum. Very few models have been proposed for illumination conditions [2]. The attempt to solve the solar cell under solar irradiation starts with the work of Wolf [35-37]. This model can predict the behaviour of single layer and two-layer solar cell under different monochromatic light source. The solution is based on directly solving the differential equation. But the limitations of this model are many [35, 36]. The solution by Wolf takes the assumption of constant lifetime, constant mobility and avoids the heavy doping effects. Hence this model, although includes the effects of incident light, is still basic in nature.

The method to model the solar cell with light is explored latter by [6]. This model actually extends the Dark current model of Park *et al.* [15]. Hence the solution given by them contains infinite sum of nested integrals, whose application to practical cases is prone to computational error [2]. Cuevas *et al.* [38] attempted to improve the model by incorporating the third-order approximations, which offers a compromise between the accuracy and computational efforts.

Along with these development, Daliento *et al.* [2, 9] proposed an extension of previous Dark current model in [39] to incorporate the effect of light. The solution is in approximate close-form and applicable for opaque heavy doped emitter. The downside of this model is that their solution suddenly introduces a constant factor in transport equation, which has to be determined by calculating mean-square-error with actual solution. The value of this constant determine the accuracy of their solution and this assumed constant does not stay constant for all cases of emitter width and surface recombination. Moreover, the expression of this constant contains integrals that have to be evaluated beforehand.

In summary, there has been very active research over a long time to find out one general model that can explain solar cell, with all its inherent physics and non-ideal behaviour.

1.3. Motivation Behind This Research

From the comprehensive literature review presented in previous section, it can be concluded that compact analytical model of solar cell under illumination is not complete. Previous models mainly focused on the dark current component and the impact of the dark saturation current when different physics is added to it. Their trend was gradually converging towards numerical integration and iteration. Similarly, some authors indeed have developed illumination models, but they have resorted to iterative approach too. It is clear that no one has yet developed a model that –

- is compact in nature
- does not need any iteration, numerical integration or numerical fitting
- shows direct relationship with the physics
- does not take unnecessary approximations to make the equation easier to solve
- is applicable over a wide range of surface recombination velocities and widths.

This thesis has got its motivation from this everlasting struggle of finding one generalized model of solar cell. Previous models rely heavily on several assumptions in the pursuit of getting analytical models. Their approximations were of wide varieties, including the assumptions for –

- Depth of emitter (Shallow or thick) [11, 28, 32-34]
- Different ranges of surface recombination velocity (high, low or medium) [2, 9, 24, 28]
- Photo-excitation (under dark condition or under light) [1-3, 15]
- Loss mechanism (either Auger or, SRH or, not recombination at all) [11, 33, 34]
- Transport Dominant Regions (dividing in either drift-dominant or diffusion-dominant) [24, 31, 32]

- Specific doping profile (constant [36], exponential [8] or Gaussian[2])
- Simplifying transport parameters (Constant mobility or lifetime) [35, 36]
- Neglecting heavy doping effect (BGN, band tailing, rigid band shift etc.) [37]

These are the approximations to simplify the physics only. Along with that, the previous works have taken assumption in solving the differential equation too. These includes –

- Taking some terms in the differential equation as constant [4, 36]
- Introducing new constant parameters that actually tries to fit the solution with numerical solution [2, 9]
- Resorting to iterative approach that uses coupled equations to be solved with an initial assumed value [3]
- Employing infinite integral series and taking only some terms as the solution (Zeroth order, 1st order, 2nd order etc.) [4, 7, 15, 39]

The limitations of the existing works have motivated this thesis to work on a new analytical model that can overcome those weaknesses. Hence, the main focus of this thesis will be to solve the fundamental transport equations directly with "as little as possible" approximations.

It is interesting to note the trend of the existing research endeavour. The initial attempts of modelling solar cell do involve the effort to directly solve the transport equations. As more physics are introduced into modelling, this direct approach gets complicated and gradually neglected by the authors; rather they resort to iteration and numerical integration, although this direct attempt promises the possibility of getting a compact solution. Adding the solar spectrum makes the direct attempt more unpleasant because it makes differential equations intractable to solve. To the author's knowledge, no one have attempted to solve the resulting complex differential equation directly with lifetime, mobility, wavelength and heavy doping effect. This thesis wants to explore this unexplored section of analytical modelling for the potential and the promises it offers.

1.4. Specific Research Objective

The main research objective of this thesis is to present a new closed-form analytical model, which does not have the need for iteration or integration. The model will try to achieve the following objectives –

A compact model	⇒	This is the primary objective of this whole endeavour. Our model will avoid all iterative schemes, any expression with integrations and any kind of numerical steps. Moreover, this solution will not try to solve the differential equation by comparing and fitting the solution with numerical models of solar cell. The sole purpose of this work is to avoid any approximated technique in solving the system of differential equations. This strict approach may warrant the use of advance mathematical functions. Previous models have already used convoluted iterating expressions to address the dark current. Hence, if necessary, this thesis will also use complex mathematical functions, for the sake of getting one general model.
Doping and Positional Dependency	⇒	Functional dependence of transport parameters for wide range of doping variation will be included in the solution. Unlike previous works, parameters like mobility and lifetime will not be taken as constant or region-wise constant. The positional variation of lifetime along the device depth, which arises from the Auger and SRH mechanism, will be considered into the derivation.

Effect of Incident Light	⇒	The solution will be general enough to include the effect from monochromatic wavelength. This work will try to present a complete model that can address the dark and illumination current simultaneously. When the generation terms are forced to zero, the same model will transform into a dark current model. Moreover, the contribution of the dark and light component and how directly other parameters interact to their influence will be studied from the derived expression.

Valid for Wide Range of Devices	⇒	The model will be developed without restricting it for certain values of emitter/base width. Some of the previous models work only for swallow emitter. Our model will try to be a general model for all emitters by overcoming this issue of thickness. Besides, existing models shows that some models are only good at low or high surface recombination and some works well in the middle. Hence, this will be a concern for our model to find out how robust our model is when surface recombination velocity varies.

Heavy Doping Effects	⇒	Some of the Dark models have included the band gap narrowing (BGN) in the transport equations. BGN will be also included in our illumination model. All the heavy doping effects will be considered, including rigid band shift, band tailing, Fermi-Dirac Statistics and degeneracy.

Effect of Biasing	⇒	The effect of biasing will be integrated in the final expression. This will be helpful in obtaining the Current-Voltage (I-V) characteristics and in finding the key parameters of solar cells (e.g. efficiency)
Expandable to multi-layer regions	⇒	An expansion of the model will be presented so that the same model can be used elegantly for multi-layered emitter regions. Besides, the base region is often followed by a back surface field (BSF). This highly-doped region improves the performance of solar cell. The expanded model will be able to handle this type of solar cell too.
Expandable to other non-Silicon material	⇒	The model will be versatile enough so that the analytical expression can be easily applied to other photovoltaic material.
Simplified model	⇒	Possible ways to simplify the proposed analytical model will be explored. But no approximation will be taken that may hamper the included physics. Only approximation related to the mathematical functions will be explored.
More General Model with standard solar spectrum	⇒	The initial version of our analytical solution uses an elegant approximated generation rate in the differential equation. An improvement of this model will use the absorption profile and actual solar spectrum, which will certainly be more accurate.

		The standard solar spectrum for the Earth surface (terrestrial) and for the Space (Extra-terrestrial) will be incorporated in the model.
Expandable to other non-uniform doping profile	⇒	The model developed here is based on exponential doping profile. Since Gaussian profile is also common in diffused regions, the model will be expanded for Gaussian profile. This will make our model complete in handling any types of non-uniform doping profile.

No previous model has tried to include so much physics, options and generality in one compact analytical model before.

1.5. Thesis Organization

The thesis hierarchy begins with this chapter, which has extensively reviewed the previous research and development in the field of analytical modeling of solar cell. This chapter has also presented the objectives to be achieved.

Chapter 2 will focus on the semiconductor device physics that is pertinent to the photovoltaic physics. Besides the fundamentals, some of the significant models will be discussed to familiarize the reader with the existing analytical approaches so far.

Chapter 3 is the crucial chapter that will develop the core analytical model. This chapter will lead the way to gradual development of the model and hence fulfilling the objectives one by one.

Chapter 4 provides the basic of TCAD modeling of solar cell. It explains the ATLAS and COMSOL numerical model, which is developed in this thesis to support and verify the analytical model.

The results and analysis are presented in chapter 5. The developed analytical model is applied for various device structures here. Besides, this chapter runs a series of analysis to check how robust the model is when the several device parameters are widely varied.

The conclusion based on the analysis is drawn in chapter 6. Besides, this chapter offers the future scope and focuses on the possibilities from this research.

Finally, Appendices A to E provides the mathematical details, briefly introduces to special mathematical functions, refers to the standard solar spectrums and documents the numerical coding of solar cell used in ATLAS device simulator.

CHAPTER 2

DEVICE PHYSICS OF SOLAR CELL

2.1. Introduction

A solar cell is just a simple p-n junction that can absorb solar irradiation and transform the photo-excitation into electricity. The performance of the solar cell depends on the material used for photovoltaic action and the inherent physics that comes with it. To increase the comparative performance of a cell, several key parameters (e.g. efficiency) have to be studied meticulously and tailored wisely. Again, these parameters depend on the minority carrier transport and the current density. Therefore, the principles of carrier drift, diffusion, generation, and recombination, as well as their contribution in the transport equations and the current-voltage characteristics will be the focus of this chapter. Gradually, other non-ideal physics of photovoltaic operation will be introduced step-by-step. Understanding these parameters will certainly pave the way to designing more efficient solar cell.

One way to comprehend the solar cell is to develop analytical models that can predict the optical and electrical behavior reliably. These models can offer us the insight in optimizing the photovoltaic devices. Hence, some of existing prominent models will be discussed here.

In summary, this chapter will serve two purposes: at one side, it will laid the foundation of photovoltaic physics to help the evolvement of this thesis; on the other hand, it will introduce some of the well-established analytical models, focusing on their individual strength, development technique, approximations, advantage, applicability and limitation.

2.2. Solar Cells: Operating principle

The photovoltaic effect is the process of converting the light energy into electrical energy. The solar cell is the semiconductor device that employs this photovoltaic conversion technique to make use of the terrestrial and extraterrestrial solar spectrum. A solar cell has three essential components:

- Light absorbing material
- A built-in electric field
- A conductive contact layer e.g. transparent conducting oxide (TCO) layer

When photons are absorbed in a material, a pair of electron and hole (EHP) is generated inside the absorbing material. After EHP generation, a built-in field will act differentially on this pair and pull out these excited EHP, before they are lost by recombining together. The presence of separating electric field is a crucial mechanism for all kinds of solar cell. The separated carriers are then fed to an external circuit via conductive contacts to get electrical work.

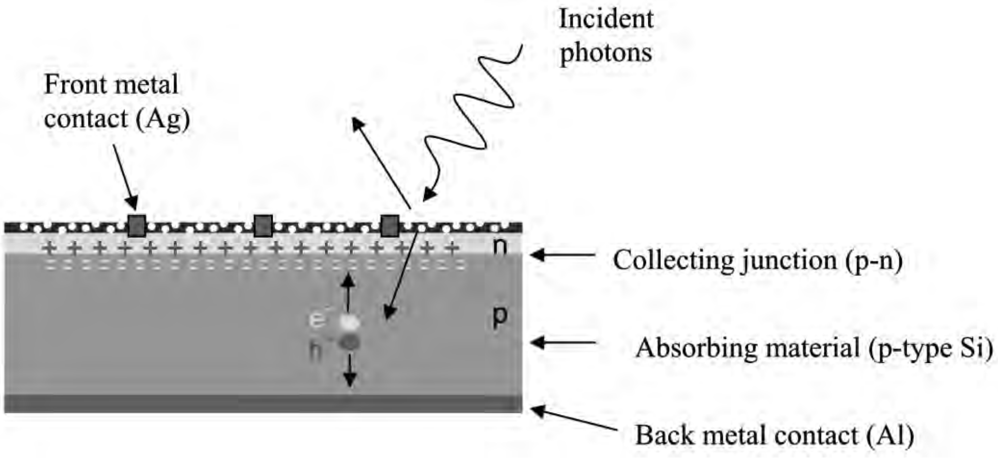

Fig. 2.1 The essential components of a typical solar cell [40]

The energy of photons depends on the color (wavelength) of light. The material, which makes up the solar cell, determines the photovoltaic properties when light is applied. When light is absorbed by matter, such as metal, photons provide the energy for electrons to move to higher energy states within the material. Afterwards the excited electrons return to their original energy state. However, in semiconductor materials, there is a built-in asymmetry (band gap). This allows the electrons to be transferred to an external circuit before they can return to their original energy state. An electromotive force can be used to direct the electrons through a load in the external circuit to perform electrical work (fig 2.2).

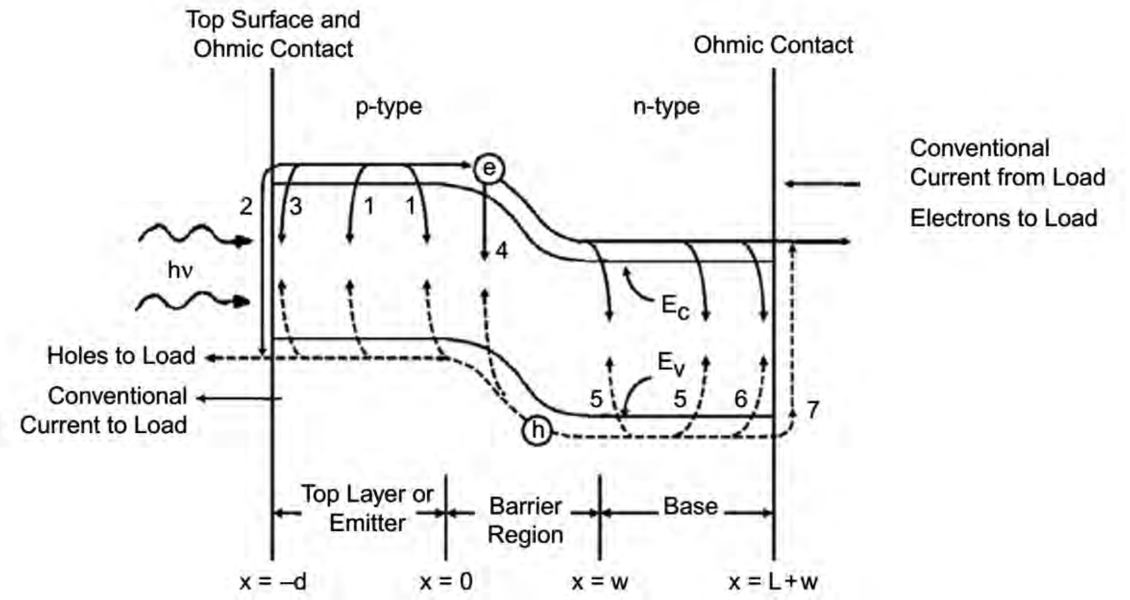

Fig. 2.2 Photo-generation and recombination in a simple p-n solar cell [41]

2.3. Performance parameters

The performance of any solar cell module is determined by measuring some specific quantities. The most prominent parameters, which are generally used for comparing photovoltaic devices, are introduced here briefly.

2.3.1. Dark and Light J-V Characteristics

It is useful to characterize a solar cell in terms of the current it produces at a given voltage, which is typically represented as a current density vs. voltage (J-V) curve. The total current is normalized via the area of the solar cell to obtain a current density J. A typical J-V curve is shown in Fig. 2.3.

Dark current (J_{Dark}) and illumination current (J_L) together determine the current-voltage characteristics of solar cell. Dark current is the current of p-n junction without any external photo-excitation. It is evident from fig. 2.3 that the illuminated J-V curve can be found simply by adding a photogeneration current to the dark J-V curve. In other words, the dark J-V curve gets shifted from the first quadrant (power dissipating mode) to the fourth quadrant (power generating mode) when light is incident on the cell. Hence, it can be said that typical solar cell exhibit superposition of currents [42].

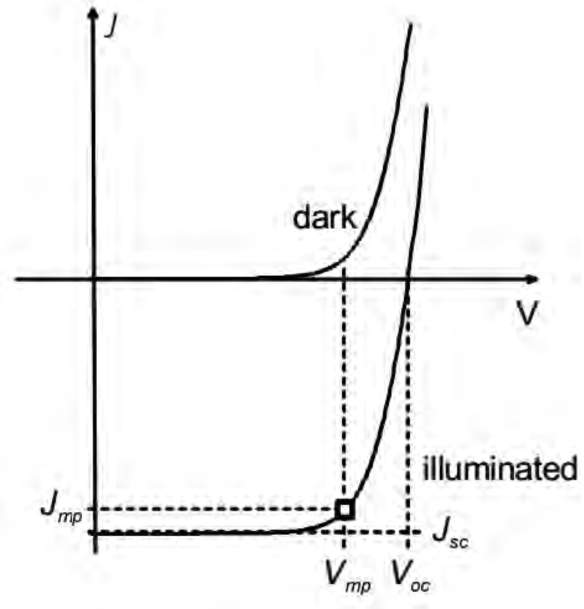

Fig. 2.3 Typical J-V characteristics of a p-n junction diode in the dark and under illumination

The dark current flows in the opposite direction to the illumination current. So, the net current is reduced from total generated photo-current. That's why, one of the main concerns of improving solar cell design is to reduce dark current component. The equation for the dark current is identical to the p-n junction current [43].

$$J_{Dark} = J_0 \left[\exp\left(\frac{qV}{K_B T} \right) - 1 \right] \tag{2.1}$$

Where, J_0 is the dark saturation current density [44]. Fundamentally, J_0 corresponds to the recombination current of the solar cell, when the cell is in thermal equilibrium with the ambient temperature. On the other hand, the illumination current depends on the incident photon-flux on the surface of the cell per unit time for a band of wavelength (dλ). The equation of light current [35] is given by equation (2.2)–(2.3).

$$I_L = q\int_0^\infty N_{ph}(\lambda)\cdot\gamma(\lambda)\cdot\lambda d\lambda = \underbrace{\left(\frac{q}{hc}\right)}_{\text{Energy per Photon}} \int_0^\infty P_{in}(\lambda)\gamma(\lambda)\cdot\lambda d\lambda \tag{2.2}$$

$$P_{\text{in}} = \int_0^\infty P_{in}(\lambda) d\lambda = \int_0^\infty N_{Ph}(\lambda)\left(\frac{hc}{\lambda}\right) d\lambda \tag{2.3}$$

Here, $N_{ph}(\lambda)$ $d\lambda$ is the number of photon incident on the surface of the cell per unit time in a range of $d\lambda$. $\gamma(\lambda)$ is the overall collection efficiency, as will be defined later in equation (2.12). The other symbols have their usual meanings (see 'List of Symbols'). The actual current density (J) is a superposition of the contributions from both dark and light response of equation (2.1)–(2.3).

$$J = J_0\left[\exp\left(\frac{qV}{K_B T}\right) - 1\right] - J_L \tag{2.4}$$

The J-V characteristic of fig. 2.3 is generally represented as in fig. 2.4, which is an inversion of J-V curve about the voltage axis. Several important parameters, that reflects the performance of photovoltaic conversion, can be extracted from the curve of fig. 2.4.

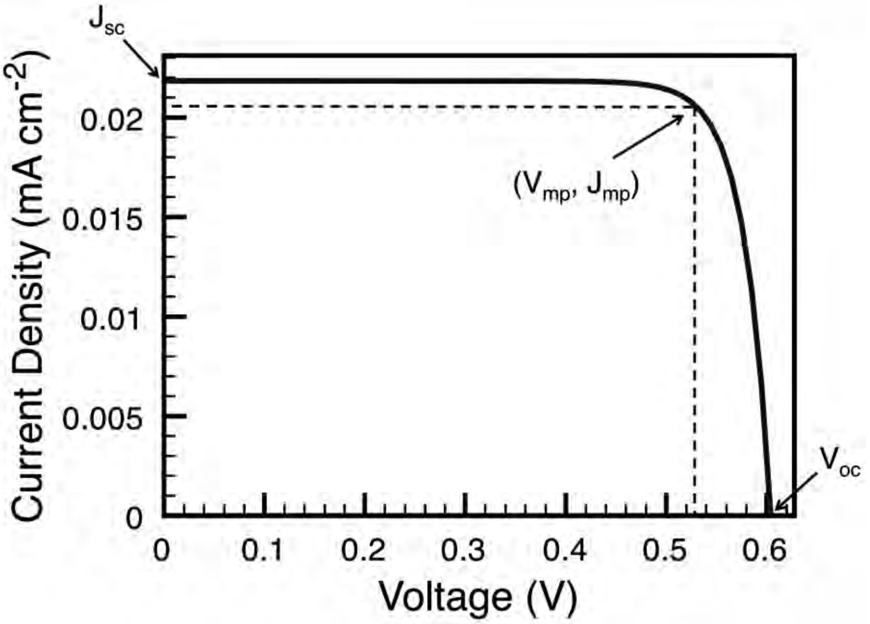

Fig. 2.4 A Typical J-V curve [45] with the open circuit voltage, V_{oc}, short circuit current density, J_{sc}, and maximum power operating point (V_{mp}, J_{mp}) labeled

2.3.2. Open Circuit Voltage (V_{OC})

The open circuit voltage is the voltage across the solar cell when the net current is zero (or, alternatively when the load resistance R→∞). For this condition, the generated photocurrent is balanced by the forward-biased junction current, as indicated by equation (2.5).

$$J_0\left[\exp\left(\frac{qV_{OC}}{K_BT}\right)-1\right]=J_L \quad \text{; Open circuit condition} \tag{2.5}$$

Low values of V_{OC} are valuable indicator of material defects and inferior quality of semiconductor. V_{OC} is also temperature dependent and decreases linearly with increasing T.

2.3.3. Short Circuit Current Density (J_{SC})

The short circuit condition is another limiting case which occurs when the load resistance is zero. In other words, when the terminals are connected to one another with no external load; hence the voltage across the cell, V=0 in equation (2.4).

$$J_{SC}=J_L \qquad \text{; Short circuit condition} \tag{2.6}$$

The short circuit current is an indicator how well the device can absorb the incident photons. I_{SC} increases linearly with increasing temperature (T). Besides, the short circuit current increases with band gap narrowing (BGN). BGN changes the absorption coefficient and hence changes the I_{SC}.

The relationship between the V_{oc} and I_{sc} is given in [44],

$$V_{OC}=\frac{kT}{q}ln\left(\frac{J_{SC}}{J_o}+1\right) \tag{2.7}$$

2.3.4. Maximum Power Point (MPP)

The output power (P) of the solar cell can be determined for any point of the J-V curve. The Maximum Power Point (MPP) represents the point over the P–V curve, which gives best possible power. This corresponds to an optimum voltage (V_{mp}) and current density (J_{mp}), as indicated in fig. 2.3–2.4. MPP can be easily located by differentiating the P-V curve. Ideally, this maximum power point should be the operating point of the device. It has been reported that maximum power point (V_{mp}, I_{mp}) shows parabolic variation with T [37].

2.3.5. Fill factor (FF)

The fill factor is defined as the ratio of maximum power and total available power. Fill factor (FF) measures how "square" the output I-V characteristics are.

$$FF = \left(\frac{V_{mp} J_{mp}}{V_{OC} J_{SC}} \right) \tag{2.8}$$

The fill factor degrades if emitter layer is too shallow and doping in emitter is too small.

2.3.6. Efficiency (η)

The efficiency of a solar cell is the ratio of the output power to the incident optical power (P_{in}).

$$\eta = \left(\frac{V_{oc} J_{sc} FF}{P_{in}} \right) \tag{2.9}$$

The input power (P_{in}) for standard solar spectrum is specified in Appendix D. The efficiency of photovoltaic solar cells gets limited because of several losses and non-idealities [37]. Some major factors are –

I. **Reflection losses on the surface**

The reflection loss is generally negligible in typical solar cells [37]. Most of the cases, the reflection coefficient r(λ) is small enough to be neglected; nonetheless the loss can be accounted in the generation term easily. Besides, the device structure with Anti-reflection coating (ARC) can further minimize the reflection loss.

II. **Incomplete absorption of incident photon**

There is a cut-off wavelength beyond which the absorption coefficient rapidly decreases [46]. This limitation results from the bandgap of the material after which the photon energy is not sufficient enough to generate EHP. The limit of spectral utilization for silicon (and others) is illustrated in fig. 2.5.

III. Utilization of only part of the photon energy for the creation of EHP

The energy of an incident photon that creates EHP may exceed the bandgap energy. This excess energy is dissipated to lattice vibration as heat (phonon). For the high frequency part of the spectrum, the heat loss is more dominant. It is already reported from the numerical evaluation that maximum 46% of the incident solar energy can be used in generating EHP for a band gap of 0.9eV [37]. This result is based on the assumption that all photons having higher energy than the bandgap will be absorbed in semiconductor to generate one EHP.

IV. Incomplete collection of the EHPs by diffusion to the p-n junction

The EHP has to be separated for collection. The electric field at the space-charge region works as the central mechanism for separating carrier pairs. Since not all the generated EHP are at the space-change region, only EHPs that are within diffusion length of the junction will be collected. The EHP can recombine before reaching the junction, which will, in turns, hamper the collection efficiency. Successful collection depends on the location of EHP, carrier diffusion, carrier recombination and lifetime. It has been demonstrated that optimum collection efficiency will be obtained if the layer between the light exposed surface and the p-n junction is as thin as possible, and if at the same time the minority carrier diffusion length is as large as possible [41].

V. The ratio of V_{OC} to Energy Bandgap (E_G)

The band gap determines the energy available for photovoltaic action. The highest achievable voltage, which is V_{OC}, is generally smaller than E_G. The reason behind this is apparent bandgap narrowing (BGN) and the typical operating condition of the solar cell at low injection level. It is obvious that better V_{OC} can be achieved when the semiconductor with large bandgap is used as solar cell. On the downside, high band gap material will reduce the percentage of spectrum utilization. Fig. 2.5 shows that GaP ($E_G \approx 2.25$eV) can only use the high frequency portion, while Silicon solar cell gets benefit from most of the spectrum.

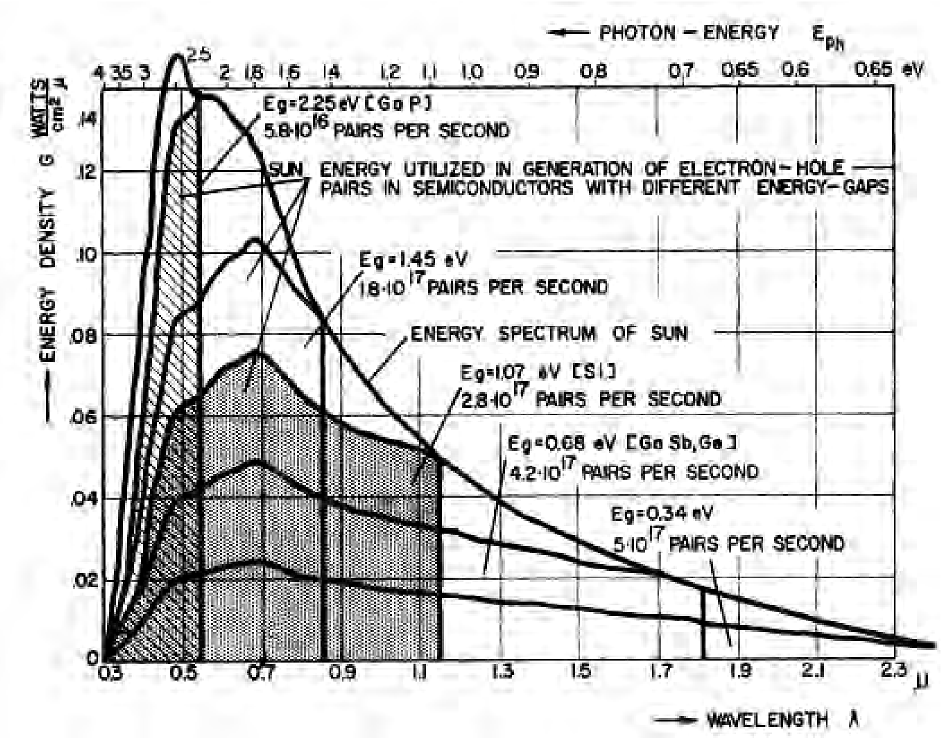

Fig. 2.5 The energy spectrum of the sun, and the parts of this spectrum utilizable in the generation of electron-hole pairs in semiconductors with energy gaps. An abrupt absorption edge with complete absorption and zero reflection on its high energy side are assumed [37]

VI. Dependence on the values of fill factor (FF)

Geometrically, FF indicates the position of Maximum Power Point (MPP) for which a largest square can be inscribed into the J-V curve. Like V_{OC}, higher FF can be obtained for high bandgap material [37] and by tailoring the impurity concentration.

VII. Degradation of the performance due to internal series resistance

The presence of series resistance will degrade the J-V curve (and, hence the efficiency). Carefully designing the emitter layer thickness and the doping level, as well as resorting to proper technique of contact formation, the negative effect of series resistance can be minimized.

2.3.7. External Quantum Efficiency (EQE)

External Quantum efficiency (EQE) is the probability that an incident photon of energy E_{ph} will be absorbed in the solar cell and excite one EHP that will be collected before recombining. In mathematical terms,

$$\eta_{QE}(\lambda) = \frac{\text{Rate of charge carriers collected under Short circuit condition, } n_q(\lambda)}{\text{Total Incident photon rate, } n_{ph}(\lambda)} \tag{2.10}$$

EQE determines the short-circuit photocurrent density (J_{SC}) by relation (2.11).

$$J_{SC} = q\int \underbrace{I_{spec}(\mathrm{E_{ph}})}_{\text{Incident Specturm}} \ \mathrm{EQE(E_{ph})\,dE_{ph}} \tag{2.11}$$

2.3.8. Collection Efficiency

The collection efficiency is defined as the ratio of EHPs separated by the space-charge electric field to the total number of *generated* EHPs (only for absorbed photons), as given in equation (2.12).

$$\eta_{\mathrm{Coll}} = \frac{\text{number of minority carrier collected by the junction}}{\text{Number of photons absorbed}} \tag{2.12}$$

The effectiveness of a photovoltaic device can be understood by the emitter collection efficiency (η), which depends on the actual photogeneration current $J_{ph}(x)$ and integrated carrier generation current, $J_{gen}(x)$. The collection efficiency of the cell can be calculated from the minority carrier current density $J_n(\lambda)$ and $J_p(\lambda)$, as shown in relationship (2.13) – (2.14).

$$\eta_{coll} = \frac{J_{ph}}{J_{gen}} = \frac{J_{ph}}{q\int_0^w G(x)dx} \tag{2.13}$$

$$\eta_{coll} = \frac{J_n(\lambda) + J_p(\lambda)}{qN_{Ph}(\lambda)\ \underbrace{\left(1 - \mathrm{e}^{-\alpha(\lambda)d}\right)}_{\substack{\text{Fraction of} \\ \text{Transmitted Photon}}}} \tag{2.14}$$

It is noteworthy that the high collection efficiency does not necessarily mean high output efficiency. Improving the collection efficiency may increase the losses in series resistance and this may offset the improvement in collection efficiency [36].

When the collection efficiency considers the reflection losses, it is called overall collection efficiency (γ).

$$\gamma(\lambda)=\left[1-r(\lambda)\right]\left(1-\mathrm{e}^{-\alpha(\lambda)d}\right)\eta_{coll} \tag{2.15}$$

To achieve higher overall collection efficiency, it is apparent from equation (2.15) that reflection losses have to be minimized. Over some specific spectrum (near 5000 A°–7000 A°), scattering reflection loss is significant e.g., losses from direct reflection. As seen in fig. 2.6, more than 6% loss is observed towards long wavelength (after 1100 A°). As stated before, this reflection loss can generally be neglected [35] because of its small value.

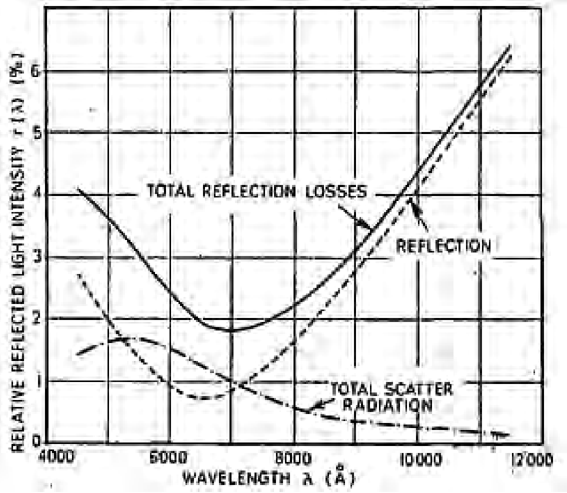

Fig. 2.6 Light reflection from a solar cell surface at different wavelength [35]

2.3.9. Spectral Response

The spectral response S(λ) of a solar cell is defined as,

$$S(\lambda)=\frac{J_{SC}(\lambda)}{E_{spec}(\lambda)} \tag{2.16}$$

Here, $E_{spec}(\lambda)$ is the spectral irradiance (see appendix D).

2.4. Models for Describing Solar cell

To understand the real-time performance and optimization of solar cell, both optical and electrical part have to be focused on. The behavior of the solar cell can be predicted by developing a comprehensive model which self-consistently treat the physics behind the optical and electrical performance. Some of the prominent models are introduced here.

2.4.1. Optical Models

There are several optical models that can predict the optical absorption inside the device. The major goal of these models is to determine the amount of light absorbed inside the device. Each of the models employs some underlying assumptions that may not be applicable to all, rather suitable to specific device structures. A general assumption is that the photon with energy greater than the semiconductor bandgap will generate one EHP. This actually indicates that the absorption rate along the device is equivalent of generation rate. The generation rate of EHP, for a certain optical frequency inside the absorbing semiconductor, can be calculated from the divergence of the poynting vector [45],

$$G_{Optical}(\vec{r},\omega)=\frac{\varepsilon''(\omega)\left|E(\vec{r},\omega)\right|^2}{2\hbar} \tag{2.17}$$

Here, $\varepsilon''(\omega)$ stands for the imaginary part of the complex permittivity of the semiconductor. The complete discussion of the optical models is beyond the scope of this thesis; only some important optical models are summarized in this section –

Beer-Lambert Law	This is a basic model that describes the exponential absorption (α_{Si}) of light intensity (I) by – $I(x)=I_0\exp\left(-\alpha_{Si}x\right)$ This 1D relationship is useful for calculating absorption in simple structures. On the contrary, the applicability of this model is limited when thin-film anti-reflection effects or Fabry-Perot type standing wave pattern is dominant [45].

Ray Tracing	This technique is based on ray optics that uses Beer-Lambert law to calculate the reduction of rays' intensity inside the structure. It also incorporates the ray reflection and Snell's law of refraction inside any multidimensional structure [47]. One limitation of this approach is from basic optics that demands the feature size of the structure has to be greater than the wavelength. Another concern of this method is that dense beams of rays have to be considered for accurate modeling of the absorption of multiple photons.
Numerical (FTDT)	This numerical approach uses Maxwell's equations (see below) and is applicable when the feature size is comparable to or smaller than the wavelength. $\frac{\partial \overrightarrow{D}}{\partial t} = \nabla \times \overrightarrow{H}$ and, $\frac{\partial \overrightarrow{H}}{\partial t} = -\frac{1}{\mu_0} \nabla \times \vec{E}$ This method uses the classical electrodynamics to simulate the electromagnetic light wave inside a structure in time domain. Although the model can solve wide range of device, solving large geometry using FTDT can be computationally intensive.

2.4.2. Electrical Models

To understand the electrical performance of the solar cell, there exists several electrical models that can shed the light on the underlying physics. The general equivalent circuit proposed for the solar cell can predict the basic behavior of the cell under illumination. One common equivalent circuit [44] is shown in fig. 2.7 below,

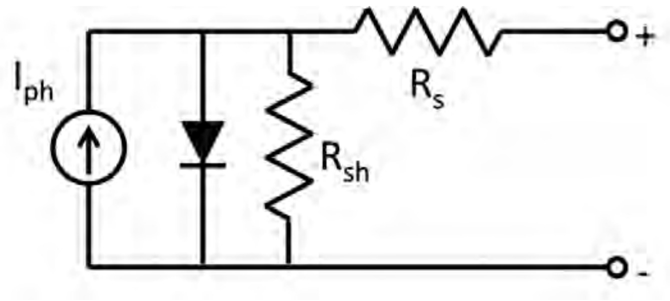

Fig. 2.7 An equivalent circuit [45] that models the J-V behavior of a solar cell

The parameters of this circuit and the contribution from their presence are summarized in table 2.1.

Table 2.1 The parameters in Equivalent circuit of Solar cell

photocurrent source, I_{ph}	This represents the illumination current which does not depend on biasing and remain constant for a certain spectrum.
Ideal Diode	The forward biased diode is here to model the dark current.
Series resistance (R_s)	This characterizes the internal losses from contact resistance which dissipate power parasitically. The origin of this resistance is the internal resistance of the device, sheet resistance of the emitter, BSF and TCO [45].
Shunt resistance (R_{sh})	This represents the current leakages in the device. The origin of this parameter is to account for the conductive pathways in the device, e.g. edge and cracks.

The current-voltage characteristic [41] of the above circuit is given by equation (2.18).

$$I = I_{ph} - I_0 \exp\left(\frac{V - IR_s}{n_D V_T} - 1\right) - \left(\frac{V - IR_s}{R_{sh}}\right) \tag{2.18}$$

It is true that this equivalent circuit offers an intuitive understanding of the current-voltage characteristics, and can address the problems caused by poor contacts and shunt resistances. But this thesis is more focused on the physics-based modeling and the microscopic description of electrical performance. This work will explore the underlying equations behind these types of equivalent circuits. Hence, to aid the development of our model that will be developed in the next chapter, the rest of this chapter will discuss the fundamental device transport equations and the prominent physics behind the transport mechanism.

2.5. Fundamental Transport Physics of Solar Cell

2.5.1. Mobility Models

On the macroscopic level, the carrier can be approximated to move at constant drift velocity (v_d) under the influence of electric field. For typical operation of solar cell, the effect of electric field on carrier mobility is not that significant. Lattice and ionized impurity scattering are the dominant factors of carrier mobility, which depends on lattice temperature (equation (2.19) below).

$$\mu_L = C_L T^{-3/2}, \qquad \mu_I = \frac{C_I T^{3/2}}{N_D^+ + N_A^-} \tag{2.19}$$

Phonon scattering, impurity scattering and carrier-carrier scattering are important mechanism in solar cell. Hence, Klaassen Mobility Model [48] can be quite useful in modeling solar cell, especially for simulation purpose.

Empirical expression of mobility vs. doping is also available in literature. For example, hole mobility can be describe by the equation (2.20) [49] or equation (2.21) [9].

$$\mu_P(x) = \frac{315}{1+\left[\frac{N(x)}{10^{17}}\right]^{0.9}} + 155\ (cm^{-3}) \tag{2.20}$$

$$\mu = \mu_{\min} T_n^{\beta_1} + \frac{\left(\mu_{\max} - \mu_{\min}\right) T_n^{\beta_2}}{\left(1+\frac{N(x)+N_a(x)}{N_{ref} T_n^{\beta_3}}\right)^{\alpha T_n^{\beta_4}}} \tag{2.21}$$

The values of these parameters can be found in [9]. Another simplified empirical relationship is proposed in [50]. They have assumed a power-law variation of mobility on the doping density (N), as in equation (2.22).

$$\mu(\mathrm{N}) = \mathrm{MN}^{-\mathrm{m}} \tag{2.22}$$

As seen in fig. 2.8, equation (2.22) is reasonably good over wide range of doping for the fitting parameters listed in table 2.1. The fit is even better for electron mobility.

Table 2.2 Values of M and m [8] for best predicting the experimental mobility

Electron Mobility	$M = 1.1 \times 10^{10}\ \mathrm{cm}^{-0.86}\ \mathrm{V}^{-1}\ \mathrm{s}^{-1}$	$m = 0.42$
Hole Mobility	$M = 1.4 \times 10^{9}\ \mathrm{cm}^{-0.86}\ \mathrm{V}^{-1}\ \mathrm{s}^{-1}$	$m = 0.38$

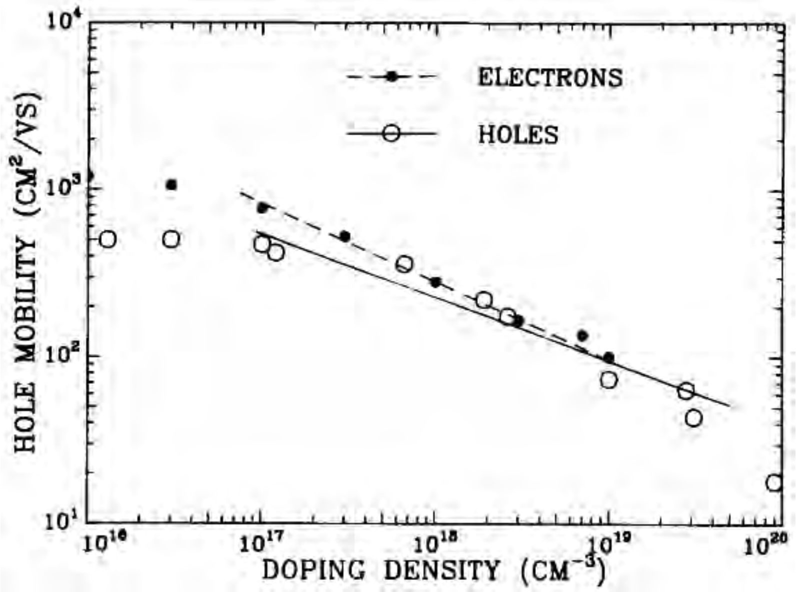

Fig. 2.8 Hole mobility vs. doping variation [8]: lines represent the empirical relationship and the symbols stands for the experimental data

2.5.2. Carrier Recombination

Carriers recombine both in the bulk and at defective interfaces. Typical sources of recombination in solar cells include –

- Band-to-band radiative recombination
- Auger recombination
- Trap-mediated (Shockley-Read-Hall) recombination

The recombination mechanisms are summarized in the fig. 2.9.

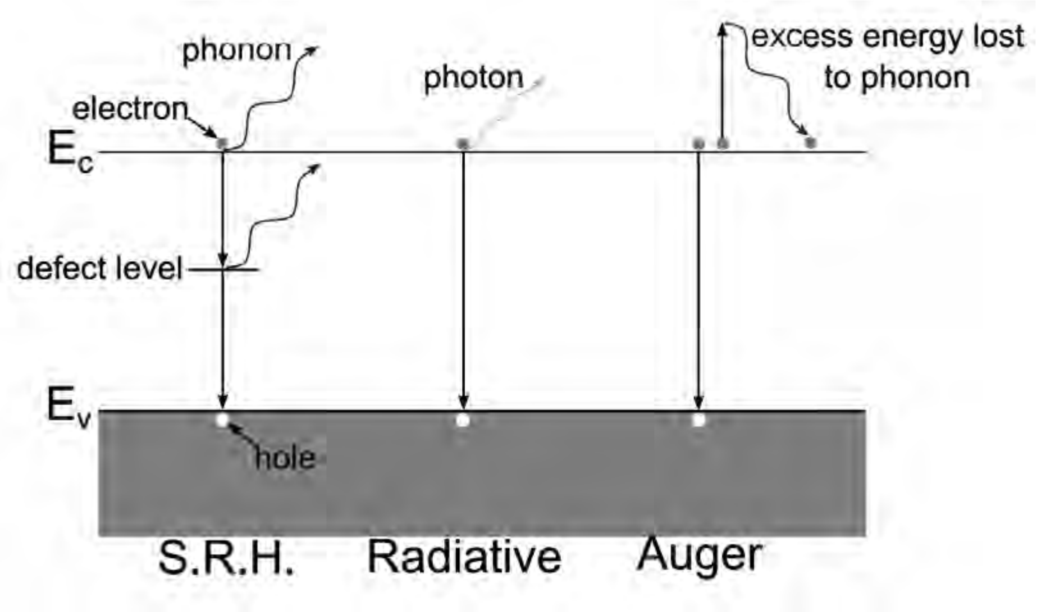

Fig. 2.9 The process of S.R.H., Radiative and Auger recombination [51]

2.5.2.1. Shockley-Read-Hall recombination

Trap-mediated recombination is the dominate recombination mechanism in the photovoltaic materials. Traps are localized electronic states in the energetic band-gap of the semiconductor. Typical sources of traps include chemical impurities and crystallographic defects in the material. The statistics of recombination through such states is described by Shockley-Read-Hall statistics. For a trap located at energy E_T, the valence band of the material, the recombination rate is given by –

$$R_{SRH} = \frac{pn - n_i^2}{\tau_{SRH.n}\left[p + n_i^{(E_i - E_T)/KT}\right] + \tau_{SRH.p}\left[n + n_i^{(E_T - E_i)/KT}\right]} \tag{2.23}$$

$$\tau_{SRH} = \left(\frac{1}{\sigma \upsilon_{th} N_T}\right) \tag{2.24}$$

Where σ is the trap capture cross-sections for electrons and holes, respectively, N_T is the concentration of trap states, n_i is the intrinsic carrier concentration and τ_{SRH} is carrier lifetime. According to Scharfetter relation [47], SRH lifetime can be related with the doping density by equation (2.25).

$$\tau_{SRH} = \tau_{\min} + \frac{\tau_{\max} - \tau_{\min}}{1 + \left(\frac{N_A + N_D}{N_{ref}} \right)^{\gamma}} \tag{2.25}$$

Where γ and N_{ref} are fit parameters, τ_{max} and τ_{min} are the best and worst case carrier lifetimes, and N_A and N_D are the bulk acceptor and donor doping.

2.5.2.2. Radiative Recombination

This recombination is a dominant recombination mechanism of direct band gap materials. In this process, the electron in conduction band and the hole in valance band recombine together, and emit a photon having the energy difference of the carriers. Hence this recombination is actually the opposite mechanism of photon absorption. The recombination rate under radiative recombination is expressed by the following equation [51],

$$R_{\text{Radiative}} = \underset{\substack{\text{Material} \\ \text{Constant}}}{B} \left(pn - n_i^2 \right) \tag{2.26}$$

For low injection condition in N-type material, the radiative recombination can be approximated by equation (2.27)

$$R_{Radiative} = \left(\frac{p - p_0}{\tau_{p.\text{radiative}}} \right) \tag{2.27}$$

Since Silicon is an indirect bandgap semiconductor, radiative recombination will not be dominant in Silicon solar cell. But for other photovoltaic material with indirect band, this recombination will be a significant mechanism for EHP loss.

2.5.2.3. Auger Recombination

When electron and hole recombine, an energy equal to the difference of their individual energy states is released. Unlike radiative recombination, if the energy is passed to another electron (or hole), the electron (or hole) becomes excited. Afterwards, the excited carrier can lose the energy through phonon emission. This is the process of Auger recombination. From the discussion, it is clear that Auger recombination is the inverse process of impact ionization. Auger recombination rate can be expressed mathematically by equation (2.28).

$$R_{Auger} = \left(C_n n + C_p p\right)\left(pn - n_i^2\right) \tag{2.28}$$

Where, C_n and C_p are temperature dependent coefficients. Under low injection condition, $C_n \approx C_p$. This reduces equation (2.28) to a simplified form, as shown below –

$$R_{\text{Auger}} \approx \left(\frac{p - p_0}{\tau_{p.\text{Auger}}}\right) \qquad \text{when, } \tau_{p.\text{Auger}} = \left(\frac{1}{C_n n_0^2}\right) \tag{2.29}$$

The Auger recombination is a dominant recombination mechanism for the heavily doped regions of solar cells [51].

In particular it is important to note that Si, the most widely used photovoltaic material, is fundamentally limited by SRH and Auger recombination due to its indirect band gap and correspondingly low radiative efficiency [52]. The net recombination rate is the contribution from all the above mechanisms.

$$R_{\text{Total}} = R_{SRH} + R_{\text{Radiative}} + R_{\text{Auger}}$$
$$\text{or, } \frac{1}{\tau_{\text{Total}}} = \left(\frac{1}{\tau_{\text{SRH}}}\right) + \left(\frac{1}{\tau_{\text{Radiative}}}\right) + \left(\frac{1}{\tau_{\text{Auger}}}\right) \tag{2.30}$$

The empirical relationship of lifetime of minority carrier exists in literature [49], e.g. –

$$\tau_P(x) = \frac{1}{50 + 2\text{x}10^{-13} N(x) + 2.2x10^{-31} N^2(x)} \tag{2.31}$$

Another author [8] presented a comparative study of several experimental data of minority carrier lifetime and proposed a power-law dependence of lifetime. This doping dependent lifetime [8, 31] is more straightforward to apply in analytical models. The empirical relation of mobility is shown in equation (2.32).

$$\tau(N) = KN^{-k} \tag{2.32}$$

The fitting values of K and k are shown in table 2.2 and the fitting is illustrated in fig. 2.10. K is known as Band-to-band Auger recombination coefficient. For these parameters, the empirical lifetime has good match with existing models and experimental data [50, 53].

Table 2.3 Values of K and k for best predicting the experimental lifetime [8]

Hole recombination lifetime	$10^{15} < N < 5 \times 10^{18} cm^{-3}$	K = 1.3 × 10^{12} cm^{-3}/s	k = 1
	$5 \times 10^{18} < N < 10^{20} cm^{-3}$	K = 5.5 × $10^{30}$$cm^{-6}/s$	k = 2
Electron recombination lifetime	$10^{15} < N < 10^{20} cm^{-3}$	K = 1.0 × 10^{31} cm^{-6}/s	k = 2

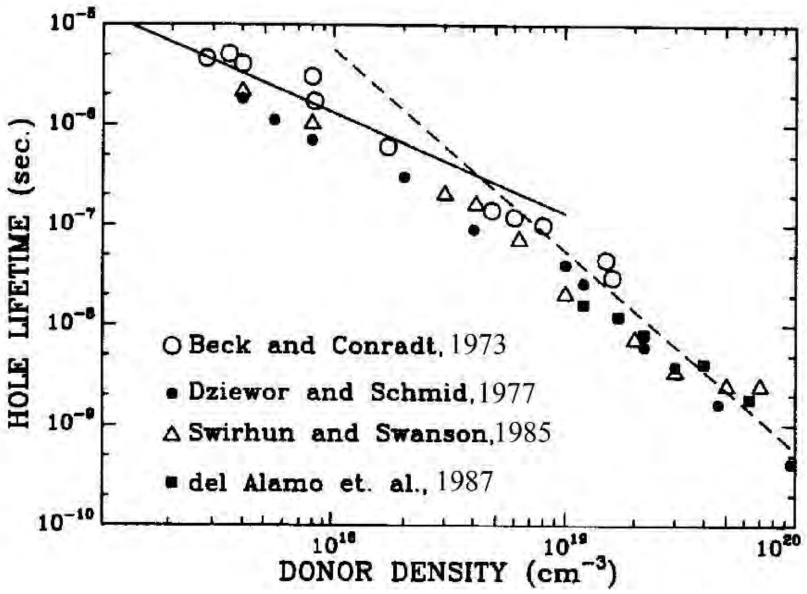

Fig. 2.10 Data for minority-hole lifetime versus doping density. The solid line is a fit according to equation (2.32).

2.5.2.4. Surface Recombination

This is basically SRH recombination through the surface defect states. The EHP can recombine at the material-interface or at the grain boundaries. Simple defects inside the semiconductor create discrete energy levels inside the band gap. Hence, it is expected that abrupt termination of the material surface will result in several defect energy levels (as seen in fig. 2.11).

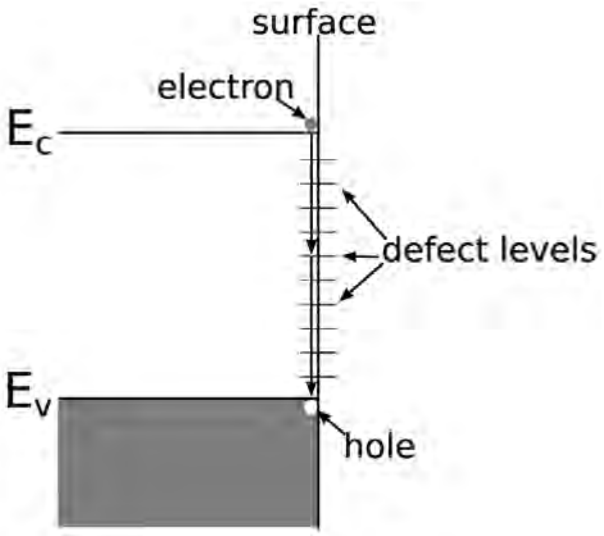

Fig. 2.11 Surface recombination in semiconductors [51]

The SRH expression in equation (2.24) has already revealed that the carrier lifetime is inversely proportional to the defect density, N_T. Therefore, the higher defect density at the surface will certainly reduce the minority carrier concentration through recombination. The modified SRH Equation that includes the surface states will be equation (2.33).

$$R_{SRH\bullet surf} = \frac{pn - n_i^2}{\left(\frac{n+n_1}{S_P}\right) + \left(\frac{p+p_1}{S_n}\right)} \tag{2.33}$$

$$\text{with,} \quad n_1 = n_{ieff} exp\left(\frac{E_{trap}}{KT}\right), \quad p_1 = n_{ieff} exp\left(\frac{-E_{trap}}{KT}\right)$$

S_n and S_p are the surface recombination velocities (SRV) of electron and hole. SRV is a measure of the diffusion process which arises from the carrier gradient between the surface and the bulk [43]. The diffusion towards the surface can be described by the following equation –

$$-D_P \left[\hat{n} \bullet \frac{d\,\mathrm{p}}{dx} \right]\Bigg|_{Surf} = S_P\, \mathrm{p}\big|_{Surf} \tag{2.34}$$

2.6. Basic Equations for modeling Solar Cell

The behavior of any semiconductor device, under equilibrium or under excitation (light, electric field etc.) can be described by using five differential equations [43]. These inter-dependent equations of (2.35)-(2.39) are the basic of semiconductor device analysis. They are –

A. Poisson's Equation

This expresses the relationship between the electric field E (or, electrostatic potential, φ) and the space-charge density, ρ.

$$\frac{d^2\varphi(x)}{dx^2} = -\frac{dE(x)}{dx} = -\frac{\rho(x)}{\varepsilon} \tag{2.35}$$

ε is the static relative permittivity of the medium.

B. Electron and Hole Current Density

The current density equations describe the carrier transport mechanisms, which consist of drift mechanism driven by an electrostatic field and diffusion mechanism driven by the random thermal motion of individual carriers. The equations are –

$$J_p(x) = J_{Diffusion}(x) + J_{Drift}(x) = -qD_p(x)\frac{dp(x)}{dx} + q\mu_p(x)p(x)E(x) \tag{2.36}$$

$$J_n(x) = J_{Diffusion}(x) + J_{Drift}(x) = qD_n(x)\frac{dn(x)}{dx} + q\mu_n(x)n(x)E(x) \tag{2.37}$$

Here, n and p are electron and hole densities respectively, μ represents mobility, and D stands for the diffusivity constants. Both hole and electron current have drift component and diffusion component. The electric field contributes in the drift, while the carrier concentration gradient causes the diffusion according to Fick's law.

C. Continuity Equation

The continuity equation consists of derivatives of current density, carrier generation term and recombination term.

$$\frac{1}{q}\frac{dJ_p(x)}{dx} = -R_p(x) + G_p(x) \tag{2.38}$$

$$-\frac{1}{q}\frac{dJ_n(x)}{dx} = -R_n(x) + G_n(x) \tag{2.39}$$

Combining the above equations will result in transport equations of carriers, as shown in (2.40)-(2.41) below. These differential equations are the core equations in deriving analytical solution and finite element based simulation. Several difficulties arises in solving these coupled equations without any approximations. Besides, the accuracy of incorporating different approximations is also a major concern.

$$D_n(x)\frac{d^2n(x)}{dx^2}+\mu_n(x)E(x)\frac{dn(x)}{dx}+\mu_n(x)n(x)\frac{dE(x)}{dx}-R_n(x)+G_n(x)=0 \quad (2.40)$$

$$D_P(x)\frac{d^2p(x)}{dx^2}-\mu_p(x)E(x)\frac{dp(x)}{dx}-\mu_p(x)p(x)\frac{dE(x)}{dx}-R_p(x)+G_p(x)=0 \quad (2.41)$$

Since all the fundamental equations and necessary physics are introduced, the next section will discuss some prominent solar cell models, as well as present the recent analytical solutions under dark and light response.

2.7. Basic Model of p-n Junction

The limiting case of efficiency from unified optical and electrical idealization of a Silicon solar cell is calculated by Shockley and Queisser [54] using the principle of detailed balance. The assumption behind this maximum efficiency is that the solar cell absorbs all the incident photons, and no electron-hole pair is lost from radiative emission. The model developed by Shockley is rudimentary in nature. The approach of his work will be presented here briefly.

2.7.1. Shockley p-n Junction model Under Equilibrium

An abrupt-junction p-n solar cell under thermal equilibrium is taken for this simple model; so, there is no external photo-excitation or biasing. The abrupt junction approximation works fine for epitaxial growth of the junction, but gives significant error for diffused layers [51]. For this simplified structure (fig. 2.12), the calculation of carrier density, electric field and electrostatic potential are the prime interest.

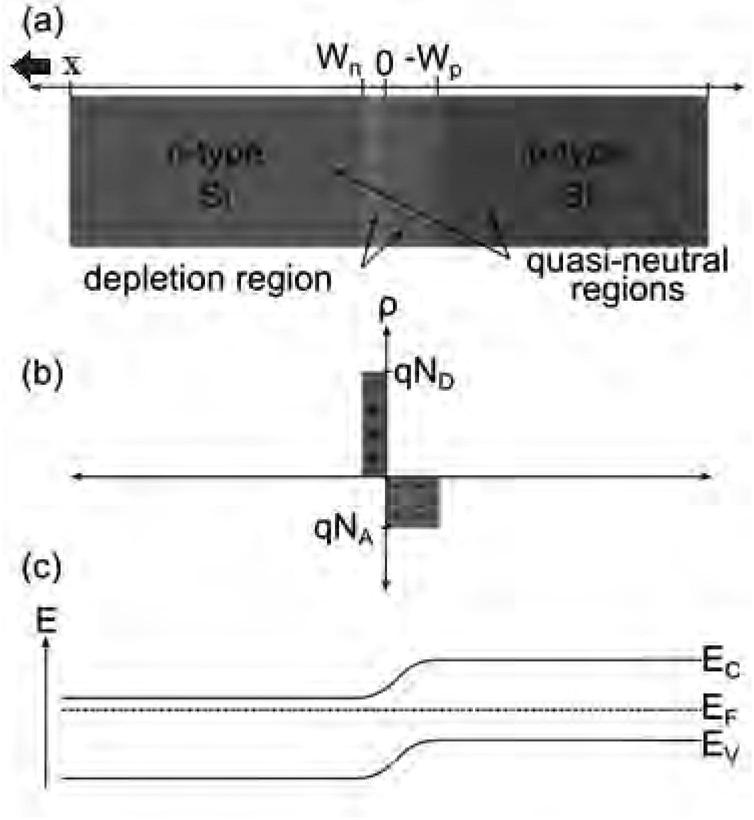

Fig. 2.12 (a) Simple p-n junction structure, (b) The space-charge density ρ across the junction, (c) Band bending across the junction

When p-type and n-type materials are contacted, the Fermi levels become identical across the junction (fig. 2.12). The mobile charge carriers from one side of the junction travel to the other side. This introduces band bending of the conduction band-edge energy and valence band-edge energy. A diffusion current of electrons from the n-doped to the p-doped semiconductor leads to a positively charged region in the n-type semiconductor. Similarly a layer of positive charge is accumulated in the p-type layer. The space-charge region is almost completely depleted of mobile charge carriers, hence the name ‘Depletion region’. The resulting electric field produces a drift force that stops the diffusion current. The diffusion and drift forces are equal at equilibrium conditions. For quasi-neutral region beyond the depletion region, the donor and acceptor charges are balanced by electrons and holes, so the space-charge density there is zero.

One of the assumptions that is commonly used in modeling solar cell is *low injection condition*. This condition requires that the majority carriers are the dominant carrier types. This can be expressed by the following conditions –

$$n_n\text{(Majority Carrier)} \gg p_n\text{(Minority Carrier) : in n-type material}$$
$$p_p\text{(Majority Carrier)} \gg n_p\text{(Majority Carrier) : in p-type material}$$

In other words, the minority carriers can be neglected when compared to the majority carriers. Inside the quasi-neutral region, the majority carriers are almost equal to the dopant density, if the donors/acceptors are fully ionized. Under low injection approximation and with thermal equilibrium, the carrier concentration follows the Boltzmann statistics [43].

$$n = N_c \exp\left(-\frac{E_c - E_F}{kT}\right) \tag{2.42}$$

$$p = N_v \exp\left(-\frac{E_F - E_v}{kT}\right) \tag{2.43}$$

Where N_c and N_v are effective density of states for conduction band and valance band, respectively. To find out the potential profile inside the depletion region, rectangular charge density approximation is used in Shockley's derivation (see fig. 2.12(b)). The space charge density inside the depletion region is –

$$\rho(x) = qN_D \qquad \text{for,} \quad 0 \le x \le W_n \tag{2.44}$$

$$\rho(x) = -qN_A \qquad \text{for,} \quad -W_P \le x \le 0 \tag{2.45}$$

Here, W_n and W_p stand for the depletion edge at the n and p side respectively (see fig. 2.12).

$$W_n = \sqrt{\frac{2\varepsilon_{Si}V_{bi}}{q}\left(\frac{N_a}{N_d}\right)\left(\frac{1}{N_a + N_d}\right)} \tag{2.46}$$

$$W_p = \sqrt{\frac{2\varepsilon_{Si}V_{bi}}{q}\left(\frac{N_d}{N_a}\right)\left(\frac{1}{N_a + N_d}\right)} \tag{2.47}$$

Using Poisson's law from equation (2.35), the electric field can be obtained by integrating (2.44)-(2.45).

$$E(x) = -\frac{qN_A}{\varepsilon_{Si}}(W_P + x) \qquad \text{for,} \quad -W_P \le x \le 0 \tag{2.48}$$

$$E(x) = -\frac{qN_D}{\varepsilon_{Si}}(W_n - x) \qquad \text{for,} \qquad 0 \le x \le W_n \tag{2.49}$$

Finally, using the electric field variation, the potential profile inside the depletion region can be derived [44]. As seen in equation (2.50)–(2.51), the potential shows quadratic dependence on distance. Fig. 2.13 shows the electric field and potential variation.

$$\phi(x) = \frac{qN_A}{2\varepsilon_{Si}} \mathrm{x}(2W_P + x) \qquad \text{for,} \quad -W_P \le x \le 0 \tag{2.50}$$

$$\phi(x) = \frac{qN_D}{2\varepsilon_{Si}} \mathrm{x}(2W_P - x) \qquad \text{for,} \qquad 0 \le x \le W_n \tag{2.51}$$

The explicit relation of the built-in potential, which results from the charge inside the depletion region, can be derived from (2.50)–(2.51).

$$V_{bi} = \frac{q}{2\varepsilon}\left(N_D W_n^2 + N_A W_p^2\right) \tag{2.52}$$

Under equilibrium, the diffusion current of one carrier is compensated by the drift current of same type. Hence, at thermal equilibrium, there is no net current flow. The electron diffusion current from the n-doped side recombine with the holes in p-doped side, and the electron drift current from the p-doped side to the n-doped side is supplied by the thermally generated electron at the p-doped side.

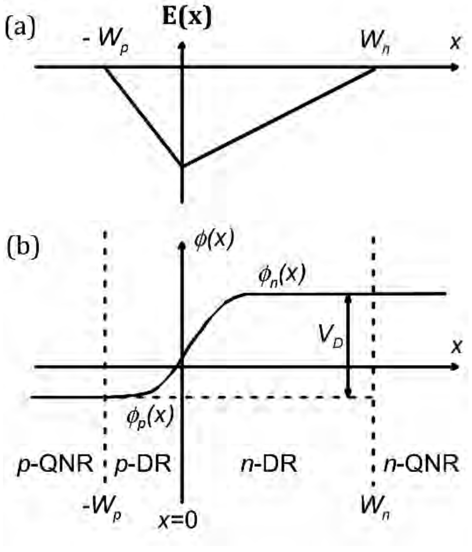

Fig. 2.13 (a) Space-charge density ρ(x); (b) electric field, E(x); (c) potential φ(x) across junction [42]

2.7.2. Shockley p-n Junction model Under non-Equilibrium

When external voltage (V_a) is applied in forward bias, the equilibrium condition is disturbed and the potential barrier across the junction changes. A forward bias decreases the potential barrier and increases the recombination current with the Boltzmann factor $\exp(V_a/V_T)$. But the thermal generation is not influenced by the applied voltage [42]. In summary, the generation-recombination current density under non-equilibrium will be –

Generation Current Density:
$$\begin{cases} J_{e.gen}\big|_{V=\mathrm{V_a}} = J_{e.gen}\big|_{Equilibrium} \\ J_{h.gen}\big|_{V=\mathrm{V_a}} = J_{h.gen}\big|_{Equilibrium} \end{cases} \tag{2.53}$$

Recombination Current Density:
$$\begin{cases} J_{e.rec}\big|_{V=\mathrm{V_a}} = J_{e.rec}\big|_{Equilibrium} \exp\left(\dfrac{V_a}{V_T}\right) \\ J_{h.rec}\big|_{V=\mathrm{V_a}} = J_{h.rec}\big|_{Equilibrium} \exp\left(\dfrac{V_a}{V_T}\right) \end{cases} \tag{2.54}$$

Total Current Density: $J = J_e + J_h = \left(J_{e.rec} - J_{e.gen}\right) - \left(J_{h.rec} - J_{h.gen}\right)$

$$\text{or,} \quad J = J_0\left[\exp\left(\frac{V_a}{V_T}\right) - 1\right] \tag{2.55}$$

Equation (2.55) is the Shockley equation. In case of high reverse bias ($V_a < 0$), the exponential term in (2.54)–(2.55) can be neglected and total current is only the reverse saturation current (J_0).

The Shockley model described the ideal p-n junction with the emphasis on the recombination mechanism. This basic model does not consider any special semiconductor physics, e.g. variable carrier lifetime etc. Hence, more elaborate models under both dark and light conditions will be the topic of subsequent sections.

2.8. General Analytical models of solar cell

There are several analytical models [1, 7-9, 15, 53, 55] that consider more physical phenomena in their derivations. Being unable to solve the transport equation in a compact form, these works have either assumed constant lifetime/mobility [36]; or assumed special functional relationship [8]; or taken an iterative approach [2, 5, 9]; or used coordinate transformation [3]; or resort to numerical approach [13, 56]; or discarded the generation term altogether [7, 15]. To focus on the limitations of these previous models and to comprehend the accomplishment of our work (in chapter 3), two of the prominent models for dark current and one model for the illumination current are presented here briefly.

2.8.1. General Analytical models of solar cell Under Dark Condition

To get a good idea about the model under the dark condition, a solar cell structure of fig. 2.14 can be considered.

The n-type emitter is non-uniform and p-type substrate has constant doping. The steady state transport equations for this quasi-neutral n-type emitter region are –

$$J_n(x) = qD_n(x)\frac{dn(x)}{dx} + q\mu_n(x)n(x)E(x) \tag{2.56}$$

$$J_p(x) = -qD_p(x)\frac{dp(x)}{dx} + q\mu_p(x)p(x)E(x) \tag{2.57}$$

$$\frac{1}{q}\frac{dJ_p(x)}{dx} = -\frac{q(p-p_0)}{\tau_P} \tag{2.58}$$

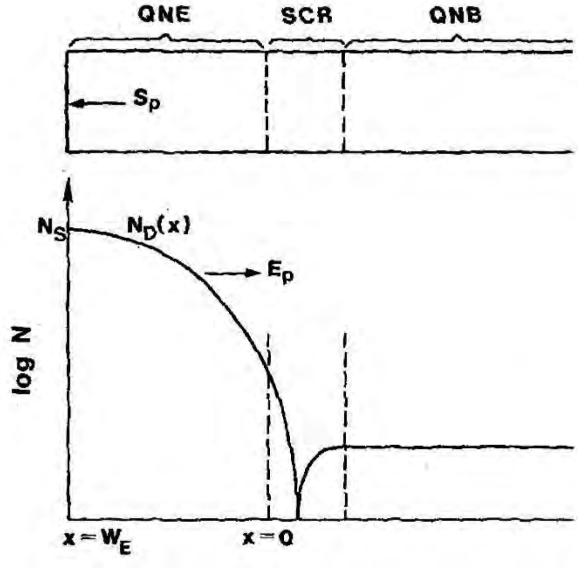

Fig. 2.14 A one-dimensional quasi-neutral n-type emitter region with graded doping profile

There is no generation term in the continuity equation, which makes this a dark current model. Under full ionization and low injection, n(x) ≈ N_D. For equilibrium condition, $P_0(x) = n_{io}^2/N_{Deff}$. Here n_{io} is the intrinsic carrier concentration and N_{Deff} is the effective doping concentration. The hole quasi-electric field is given by –

$$E_P = -\left(\frac{KT}{q}\right)\frac{d}{dx}\ln\left(N_{Deff}\right) \tag{2.59}$$

Equation (2.59) results in the following equation for minority carrier current,

$$J_p(x) = -qD_p(x)\left[p\frac{d\ln(N_{Deff})}{dx} + \frac{dP}{dx}\right] \tag{2.60}$$

The boundary conditions at the top surface and at the junction are –

$$p(0) = \frac{n_{io}^{\;2}}{N_{Deff}(0)}\left[\exp\left(\frac{V_{BE}}{V_T}\right) - 1\right] \tag{2.61}$$

$$J_P(W_E) = qS_P\left[p(W_E) - P_0(W_E)\right] \approx qS_P p(W_E) \tag{2.62}$$

Up to now, the equations introduced are common in all the approaches taken by the authors. But to solve the equations, several approximations are employed to make the solution easy.

Previous analytical works have shown heavy dependence on iterative approach [7, 15]. Beside this technique, coordinate transformation approach has also been used. These two models will be discussed here.

2.8.1.1. Integral and Iterative Approach

Iterative solutions are one of the attempts to address the system of differential equations for solar cell. Park *et al.* [15] has proposed a systematic integral approach of analytical solution by integrating (2.60) from 0 to x,

$$p'(x) = p_0(x)\left[1 - \frac{1}{q}\int_0^x dx'\frac{1}{D_P(x')p_0(x')}J'(x')\right] \tag{2.63}$$

In the above equation, p′(x) and J′(x) are normalized quantities [15]. Equation (2.63) expresses the dependence of current density on the minority carrier concentration. Now, integrating (2.58),

$$J'(x) = J'(0) - q\int_o^x \frac{p'(x')}{\tau_P(x')}dx' \tag{2.64}$$

Substituting the above equation back into (2.63) gives –

$$p'(x) = p_0(x)\left[1 - \frac{1}{q}\int_0^x \frac{dx'}{D_P(x')p_0(x')}\left\{J'(0) - q\int_o^{x'} \frac{p'(x")}{\tau_P(x")}dx"\right\}\right] \tag{2.65}$$

After substituting repeatedly, an iterative analytical expression can be obtained.

$$p'(x) = p_0(x)\left[1 - \frac{J'(0)}{q}\sum_{i=1}^{\infty} A_{2i-1}(x) + \sum_{i=1}^{\infty} B_{2i}(x)\right] \tag{2.66}$$

Where,

$$\begin{aligned} \mathrm{A}_{2\mathrm{i}-1}(\mathrm{x}) &= \int_0^x dx_1 \frac{1}{D_P(x_1)p_0(x_1)}\int_0^{x_1} dx_2 \frac{p_0(x_2)}{\tau_P(x_2)} \\ &\quad \ldots\int_0^{x_{2i-2}} dx_{2i-1} \frac{1}{D_P(x_{2i-1})p_0(x_{2i-1})} \end{aligned}$$

$$\begin{aligned} \mathrm{B}_{2\mathrm{i}}(\mathrm{x}) &= \int_0^x dx_1 \frac{1}{D_P(x_1)p_0(x_1)}\int_0^{x_1} dx_2 \frac{p_0(x_2)}{\tau_P(x_2)} \\ &\quad \ldots\int_0^{x_{2i-1}} dx_{2i} \frac{p_0(x_{2i})}{\tau_P(x_{2i})} \end{aligned}$$

As seen from equation (2.66), the current and carrier concentration are coupled together. Park *et al.* has proposed different approximations by truncating the solution at finite order:

Zeroth Order Approximation	The simplest approximation is to take only the first term in (2.66)

First Order Approximation	This approximation takes A_1 term in (2.66)

Second Order Approximation	This approximation keeps both A_1 and B_2 term

The expression developed here are not explicit in nature, rather obscure in terms of repetitive integration. Besides, the expression has to maintain a convergence criterion [15]. The fast convergence is obtained if hole quasi-Fermi potential is nearly spatially independent in the Quasi Neutral Emitter. This extended QE is satisfied in the small S, and W_E << Lp. For emitters with large S, or for emitters with W_E >> Lp, deviations from this condition increase with distance from x = 0. Hence, their model is not strictly satisfactory for large S_p or thicker emitter [7].

The above analytical model also does not consider the effect from the solar spectrum. The solution from each approximation of this integral approach and the exact simulation shows the region where the model fails (see fig. 2.15).

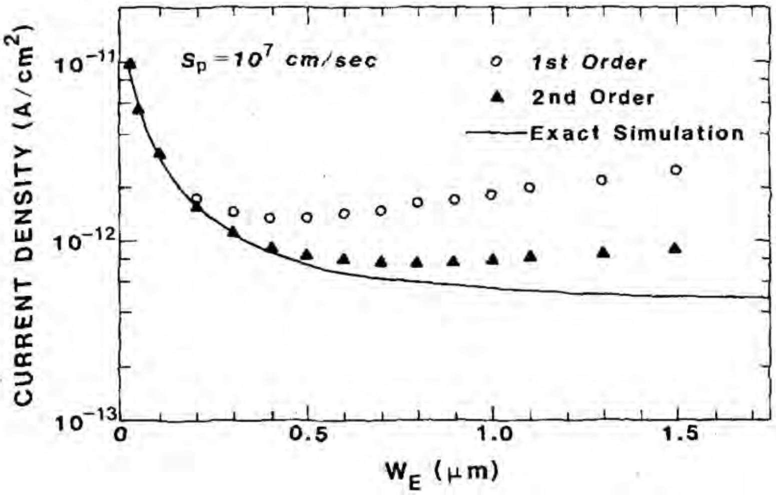

Fig. 2.15 Comparison of exact numerical solution with the first- and second order approximation for various emitter width [7].

Along with Park [15], the work of Cuevas [4, 5, 38] and Rinaldi [7, 55] fall in the same category. The approach of Rinaldi is similar to integral technique, where the iterative solution is improved by adding another approximation (by considering the third term in the expansion).

2.8.1.2. Coordinate Transformation Approach

This attempt is taken by Burger *et al.* [3]. A coordinate transformation technique is applied to simplify the transport parameter. Moreover, this transformation shows advantageous symmetry in the developed equation. This method uses two first-order non-linear differential equations for the dimensionless surface recombination velocity s and its reciprocal r [3]. The drawback of this work is that an approximate initial solution has to be taken, which is obtained from solving a uniformly doped emitter. Besides, this is actually an incarnation of previously described iterative approach.

The underlying transport equations are same as (2.58)-(2.62). The important step in the derivation is the introduction of a new coordinate y(x) as follows –

$$y(x) = \int_0^x \frac{d\xi}{L_n(\xi)} \tag{2.67}$$

This coordinate transformation results in the following differential equations for a P-type emitter layer,

$$J_n = \left(q\frac{D_n}{L_n} n_0 \right) \frac{d\nu}{dx} = J_{0c}\nu' \tag{2.68}$$

$$\frac{dJ_n}{dx} = \left(q\frac{D_n}{L_n} n_0 \right) \nu = J_{0c}\nu \tag{2.69}$$

Where, $\nu = [n(x) - n_0(x)] / n_0(x)$ and $L_n^2 = D_n\tau_n$. The equations (2.68)-(2.69) form a symmetrical set of equations. The diffusion length L_n is required for the transformation. Their work takes the assumption that for every y coordinate an effective surface recombination velocity S(y) is defined.

$$S(y) = \frac{J_n(y)}{q\Delta n(y)} \tag{2.70}$$

By introducing a dimensionless quantity $s = S(y)L_n(y)/D_n(y)$ & its reciprocal $r = 1/s$, equation (2.68) and (2.69) can be decoupled and reduced to first order equations (see below).

$$\nu' = s\nu$$

$$J_n' = \mathrm{r}J_n$$

From the above development, it is now possible to deploy a set of 2 linear second-order differential equation for J_n & ν, and two equivalent first-order non-linear differential equations for s and r [3].

linear second-order differential equation	Equivalent first-order non-linear differential equations
$\nu'' + \nu'\left(\frac{J'_{0c}}{J_{0c}}\right) - \nu = 0$	$s' = 1 - s^2 - s\left(\frac{J'_{0c}}{J_{0c}}\right)$

$J_n'' + J_n'\left(\frac{J'_{0c}}{J_{0c}}\right) - J_n = 0$	$r' = 1 - r^2 + r\left(\frac{J'_{0c}}{J_{0c}}\right)$

It is noteworthy to mention that their final expressions, those obtained after solving the above differential equations, are also in asymptotic series like equation (2.66) of Park *et al.* [15]. Besides, first-order Newton approximation is used to get the improved initial solution by linearizing the differential equation of s (or, r).

In summary, the approach taken by Burgers *et al.* is just a derivatives of previous iterative model. Not to mention that, their work is limited to dark condition only.

2.8.2. General Analytical model of solar cell Under Illumination

Previous models discussed so far assumed an extreme assumption that has made those model inapplicable to solar cell. That assumption is the elimination of generation term (G) completely. Although those dark response models are useful for many practical devices, they cannot predict the electrical behavior of solar cell. This section will briefly introduce the analytical works that attempted to model the effect from solar spectrum.

In the literature, the models for illumination conditions are very few. Even those few works have considered several assumptions, depending on the emitter thickness W with respect to the minority carrier diffusion length (L_P). Three common models are –

Models	Condition
Transparent Model (T model)	$W < L_P$, accurate only for very thin regions, with a highly recombining contact and negligible bulk recombination
Quasi-Transparent Model (QT model)	$W \approx L_P$
Opaque Model	$W > L_P$

To discuss the traditional approach of solving solar cell under illumination, the model of Daliento *et al.* [2] will be introduced here briefly. Their model actually follows the steps of coordinate transformation, as discussed in previous section. From the traditional transport equations and defining the normalized excess hole concentration u(x) = (p-p_0)/p_0, they transformed the differential equation as follows,

$$\frac{d^2u'}{dy^2}-\underbrace{\left(\frac{p_0D_p}{L_p}\right)}_{C_S}^2u'=-\underbrace{\left(\frac{p_0D_p}{L_p}\right)}_{C_S}L_p\left[\frac{G}{u(0)}\right] \tag{2.71}$$

At this point, they defined a quantity C_s, and assumed C_s to be constant so that the differential equation can be solved. The value of C_s is obtained by minimizing the mean-square error with the exact numerical solution under dark condition [2].

$$\overline{Cs}=\left[\frac{\int_0^w\frac{p_0(x)}{\tau_p(x)}\exp\left(-2\int_0^x\frac{d\xi}{L_p(\xi)}\right)dx}{\int_0^w\frac{1}{p_0(x)D_p(x)}\exp\left(-2\int_0^x\frac{d\xi}{L_p(\xi)}\right)dx}\right]^{\frac{1}{2}}$$

This is certainly a huge limitation of their model which first needs the exact numerical solution to get C_S. Besides, the error in assumed value of C_s strongly hampers the accuracy of the model.

The authors have compared the efficiency of their model with the Silvaco/Atlas simulation and another previous model [6] (see fig. 2.16). Although they are claiming that the final expression of efficiency directly relates the technological parameters of emitter, actually the relationship is obscure and not in direct form; besides, it is based on unsound approximations and contains a lot of integrals. Moreover, their model works well for high surface recombination velocity; while for lower surface recombination, it shows significant deviation. Other models e.g. that of Bisschop [6] or Wolf [36] has taken direct approach, but they assumed constant lifetime and mobility in solving the differential equations.

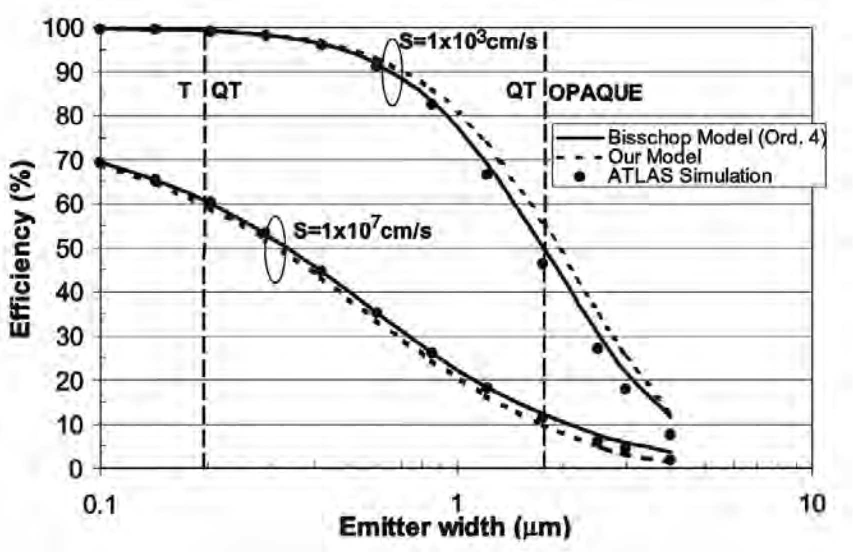

Fig. 2.16 Comparison between the emitter efficiency evaluated by [2] and that by the fourth-order truncation of the Bisschop series [6], with the actual solution given by the numerical simulator ATLAS

2.9. Conclusion

The objective of this chapter is to offer the necessary background of the transport physics behind solar cell that will aid the development of subsequent chapters. Along with that, this chapter presents several prominent optical and electrical models briefly to point out the limitation of previous analytical approaches; this will be helpful in clearly understanding the success of our analytical model over the existing ones.

CHAPTER 3

DEVELOPMENT OF THE ANALYTICAL MODEL

3.1. Introduction

The aim of this chapter is to develop a complete analytical model of minority carrier profile for a non-uniformly doped silicon solar cell. It is the *first time* for an iteration-free and integral-free compact analytical expression, which includes solar spectrum, positional dependence of doping, lifetime and mobility variation, all in one model. The position-dependent doping turns the transport parameters (e.g. minority carrier mobility and lifetime) into a function of position, which leads to an analytically intractable differential equation. However, the proposed work will try to overcome the problem and offer a complete analytical solution by adopting various mathematical functions. Afterwards, the mathematical model will be improved gradually to achieve more general solution. The validity of this solution by numerical (TCAD & FEM) models will be the topic of subsequent chapter.

This chapter is organized and developed to achieve the following objectives –

- Establishing the analytical model for *Hole concentration* in n-type region, where the donor doping is *exponentially decreasing*
- Establishing the analytical model for *Electron concentration* in P-type region, where the acceptor doping is *exponentially decreasing*
- Modifying the analytical model of *Hole concentration*, if the donor doping is *exponentially Increasing*
- Developing a More general analytical model *without using any approximations in generation term G*
- Developing a *Two layer model* for multi-layer Solar Cell
- Extending the analytical solution *for Gaussian doping* profile

In obtaining the solution for doping non-uniformity, exponential doping will be considered. The reason behind is that exponential variation in doping is quite common in device fabrication. When the emitter region of p^+n junction is fabricated by implantation followed by a drive-in anneal, the doping profile follows an exponential dependence with depth [8]. Hence, exponential doping will be our choice.

3.2. Analytical Model For Minority Carrier Hole Density

An exponentially-doped n(x)–p drift field (DF) silicon solar cell is shown in Fig. 3.1. The analytical solution for DF solar cell structure with non-uniformly doped region is presented in [36]; but their derivation assumed constant lifetime or piece-wise linear lifetime, which made the resulting differential equations easy to solve. This assumption certainly is not valid when there is concentration gradient in impurity. To establish our model, similar DF solar cell structure of fig. 3.1 will be used. Unlike previous work, doping-dependent lifetime and mobility under solar spectral irradiance will be used in the transport equations. Besides, the solution will avoid any kind of iterative approach. At first, the expression of hole concentration in an n-type emitter will be investigated.

In solar cell modelling, the transport parameters are generally assumed as a function of depth (x) only. This assumption is very common is literature [9, 15, 55] and also verified by numerical simulation [18]. Since the length and width dimensions are extremely large compared to a diffusion length for minority carriers, this assumption is reasonable. Our TCAD simulation also supports this assumption (see ATLAS 2-D simulation of electron and hole concentration in chapter 4). Hence the analysis here will be confined to one dimension. Besides, the minority carrier continuity and current equations will be solved considering the quasi-neutrality and low-injection conditions [3] under steady state.

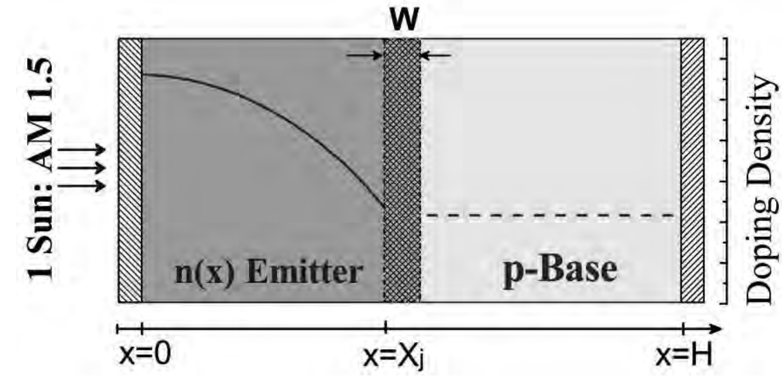

Fig. 3.1. A DF (Drift Field) solar cell structure

The transport equations [9] for minority carriers in the emitter region are already presented in chapter 2 and repeated here for easy access,

$$J_p(x) = J_{diffusion}(x) + J_{drift}(x) = -qD_p \frac{dp}{dx} + q\mu pE \tag{3.1}$$

$$\frac{dJ_p}{dx} = -q\frac{p}{\tau_p} + qG \tag{3.2}$$

Here, J_P denotes hole-current density, τ_P is the minority carrier recombination lifetime, D_P is hole diffusivity, p is the minority carrier (Hole) density and E is the electric field introduced due to non-uniform doping in emitter. Another important parameter is carrier generation rate (G), which is the result of exposed solar illumination. Generation rate is a function of depth into the material (x) and wavelength (λ) of incident solar spectrum. $G(\lambda, x)$ is generally considered as a sum of individual contributions over the whole solar spectrum, but it can be well-approximated by a series of three to five exponential terms [57, 58]. The validity of this approximation is well-established in literature [57] for different material and different solar spectrum. The approximated generation rate [59] of minority carrier can be expressed by,

$$G(x) = \sum_{i=1}^{n} a_i e^{-b_i x} \tag{3.3}$$

Since the emitter is non-uniformly doped, lifetime (τ) and mobility (μ) will depend on doping profile (N). For our purpose, the empirical equation of mobility [8] will be used.

$$\mu(N) = MN^{-m} \tag{3.4}$$

Equation (3.4) can predict the minority carrier hole mobility when $M = 1.4 \times 10^9$ $\mathrm{cm}^{0.86}\mathrm{V}^{-1}\mathrm{s}^{-1}$ and $m = 0.38$. This gives very good approximations of actual experimental data. Power-law dependence of lifetime [8, 31] will also be used in this analysis. The empirical relation of lifetime is given by equation (3.5).

$$\tau(N) = KN^{-k} \tag{3.5}$$

Carefully calculated values of K and k shows good match (see chapter 2) with the existing experimental data [53]. Hence, the above power-law dependence of lifetime will be used in the drift-diffusion equation.

The important thing to note here is that our model will use all these general parameters (K, k, M, and m) to address the position dependency of mobility and lifetime in the solution. Hence, the same model will be able to analyse a wide range of photovoltaic materials if the parameters are tailored appropriately for other doping profile & material properties.

The electric field associated with the exponential doping is taken into account by equation (3.6) under quasi-neutrality condition. Equation (3.6) includes the effects from doping gradient in the first term and the effects of band gap narrowing in second term.

$$E = -V_T \frac{d \ln N}{dx} + \frac{1}{q} \frac{d \Delta E_G}{dx} \tag{3.6}$$

$$\Delta E_G = efV_T \ln\left(\frac{N}{N_0} \right) \tag{3.7}$$

Equation (3.7) represents the apparent band gap narrowing data [53], where $N_o = 7 \times 10^{17}$ cm^{-3}. When doping (N) is below N_0, there is no BGN and hence, $f = 0$. However, for $N > N_0$, the BGN is significant and $f = 0.75$. This equation is a good approximation to include the heavy doping effects like Fermi-Dirac statistics, rigid band shift, band tailing and degeneracy.

The doping profile in the emitter is given by equation (3.8). The peak emitter doping concentration (N_{d0}) and exponential decay (α) are positive quantities.

$$N(x) = N_{d0} e^{-\alpha x} \tag{3.8}$$

Considering equations (3.1)-(3.4), (3.5)-(3.7), the minority carrier hole concentration p(x) can be expressed in terms of doping (N),

$$\frac{d^2 p}{dx^2} + (1-m-f) \frac{d \ln N}{dx} \frac{dp}{dx} - \left[m(1-f) \left(\frac{d \ln N}{dx} \right)^2 + (f-1) \frac{d^2 \ln N}{dx^2} + \frac{N^{m+k}}{KMV_T} \right] p = -\left(\frac{N^m}{MV_T} \right) \sum_{i=1}^{5} a_i e^{-b_i x} \tag{3.9}$$

This is a second order non-homogeneous differential equation. By inserting N(x) from equation (3.8) into (3.9), the differential equation can be expressed as a function of device depth x.

$$\frac{d^2p}{dx^2}+\alpha(m+f-1)\frac{dp}{dx}-\left(m(1-f)\alpha^2+\frac{N_{d0}{}^{m+k}e^{-\alpha(m+k)x}}{KMV_T}\right)p$$
$$=-\left(\frac{N_{d0}{}^{m}e^{-\alpha m x}}{MV_T}\right)\sum_{i=1}^{5}a_i e^{-b_i x} \tag{3.10}$$

Finally, substituting z = $e^{-\alpha(m+k)x/2}$ in (3.10) results in equation (3.11).

$$z^2\frac{d^2p}{dz^2}+(1-2A)z\frac{dp}{dz}-\left(\beta^2z^2+\kappa^2\right)p=-\sum_{i=1}^{5}C_i z^{D_i} \tag{3.11}$$

Here,

$$A=\left(\frac{f+m-1}{m+k}\right) \tag{3.12}$$

$$\beta=\frac{2}{\alpha(m+k)}\sqrt{\frac{N_{d0}{}^{m+k}}{KMV_T}} \tag{3.13}$$

$$\kappa=\frac{2\sqrt{m(1-f)}}{m+k} \tag{3.14}$$

$$C_i=\frac{4N_{d0}{}^{m}}{MV_T\alpha^2(m+k)^2}a_i \tag{3.15}$$

$$D_i=\frac{2(b_i+\alpha m)}{\alpha(m+k)} \tag{3.16}$$

Introducing $p(z)=z^A u(z)$ will reduce equation (3.11) to a non-homogeneous Bessel equation of order ν.

$$z^2\frac{d^2u}{dz^2}+z\frac{du}{dz}-\left(\beta^2z^2+\nu^2\right)u=-\sum_{i=1}^{5}C_i z^{\gamma} \tag{3.17}$$

Here, $\nu=\sqrt{A^2+\kappa^2}=\sqrt{4m(1-f)+(f+m-1)^2}\Big/(m+k)$, which is a non-integer number and $\gamma=\left(D_i-A\right)$. The homogeneous solution of (3.17) can easily be obtained in terms of modified Bessel function of first kind.

$$u(z)=C_1I_\nu(\beta z)+C_2I_{-\nu}(\beta z) \tag{3.18}$$

If the contribution from spectrum is not included, then the right hand side (RHS) of (3.17) will be zero and (3.18) will be the solution of dark condition. This is exactly the approach of [8]. Finding the particular solution with RHS (i.e., under solar illumination) is avoided by the previous works. Several authors [15, 49, 60] rather resorted to iterative scheme. But we insist on finding the particular solution of equation (3.17).

To obtain the complete solution $\mathrm{u}(\mathrm{z})$ considering the non-homogeneous term in the RHS of equation (3.17), the variation of parameter [61-63] will be employed. Presence of Bessel function in the complementary solution of equation (3.18) warrants the use of Hypergeometric function. The computation of this part is straightforward albeit moderately time consuming. The mathematical details are presented in the appendix A and skipped here for the readability. After applying variation of parameter and re-substituting $\mathrm{p}(\mathrm{z}) = z^A u(z)$, the minority carrier profile $\mathrm{p}(\mathrm{z})$ can be expressed as follows,

$$p(z) = \underbrace{P_1(z)\,C_1 + P_2(z)\,C_2}_{\text{Dark Response}} + \underbrace{P_3(z)}_{\text{Light Response}} \tag{3.19}$$

With,

$$P_1(z) = z^A I_\nu(\beta z); \qquad P_2(z) = z^A I_{-\nu}(\beta z)$$

$$\begin{aligned} P_3(z) &= -\sum_{i=1}^{5} \frac{E_i \pi}{2\sin(\pi\nu)} \times z^A \\ &\left[I_\nu(\beta z) \frac{2^\nu (\beta z)^{\gamma-\nu}}{(\gamma-\nu)\Gamma(-\nu+1)}\, {}_1F_2\left(\frac{\gamma-\nu}{2}; -\nu+1, \frac{\gamma-\nu+2}{2}; \frac{\beta^2 z^2}{4} \right) \right. \\ &\left. -I_{-\nu}(\beta z) \frac{2^{-\nu} (\beta z)^{\gamma+\nu}}{(\gamma+\nu)\Gamma(\nu+1)}\, {}_1F_2\left(\frac{\gamma+\nu}{2}; \nu+1, \frac{\gamma+\nu+2}{2}; \frac{\beta^2 z^2}{4} \right) \right] \end{aligned} \tag{3.20}$$

Here, I_ν and $I_{-\nu}$ are the modified Bessel functions of the first kind and ${}_1F_2$ is the Generalized Hypergeometric function. C_1 and C_2 are constants which will be determined by using proper boundary conditions of certain type of solar cell.

If the n-type emitter of fig. 3.1 is considered as an example, then the boundary conditions [8] for this DF solar cell will be,

$$p(x_j) = \frac{n_i^2}{N(x_j)} \exp\left(\frac{V}{V_T} \right) \tag{3.21}$$

$$\left[\mu(x) E p(x) - D_p(x) \frac{dp(x)}{dx} \right]_{x=0} = S_p\, p(0) \tag{3.22}$$

The boundary conditions can easily be modified for z using the transformation $z = \exp\left[-\alpha(m+k)x/2\right]$. The 1st boundary condition in (3.21) is evaluated at $z = z_j = \exp\left[-\alpha(m+k)x_j/2\right]$. The 2nd boundary condition in (3.22) describes front-surface characteristics through surface recombination velocity (S_p). Equation (3.22) involves the derivatives of p(z), which means the derivatives of Bessel function and Hypergeometric function has to be calculated first. Using the identities of differentiating Bessel and Hypergeometric function, $dp(z)/dz$ can be obtained as follows (see Appendix A).

$$\frac{dp(z)}{dz} = X_1(z)\, C_1 + X_2(z)\, C_2 + X_3(z) \tag{3.23}$$

Here,

$$X_1(z) = Az^{A-1} I_\nu(\beta z) + z^A \frac{\beta}{2}\left[I_{\nu-1}(\beta z) + I_{\nu+1}(\beta z)\right] \tag{3.24}$$

$$X_2(z) = Az^{A-1} I_{-\nu}(\beta z) + z^A \frac{\beta}{2}\left[I_{-\nu-1}(\beta z) + I_{-\nu+1}(\beta z)\right] \tag{3.25}$$

$$X_3(z) = -\sum_{i=1}^{5} \frac{E_i \pi}{2\sin(\pi\nu)} \times \left[F_{+\nu}(z) - F_{-\nu}(z)\right] \tag{3.26}$$

$F_{+\nu}(z)$ is defined in (3.27) which strongly depends on transport constants (K, k, M, m) and generation coefficients (a_i, b_i). $F_{-\nu}(z)$ is similar to (3.27) with ν replaced by –ν and vice versa.

$$\begin{aligned} F_{+\nu}(z) = {} & \frac{2^\nu \beta^{\gamma-\nu} z^{\gamma-\nu+A}}{(\gamma-\nu)\overline{|-\nu+1}} \times \\ & \left[{}_1F_2\left(\frac{\gamma-\nu}{2}; -\nu+1, \frac{\gamma-\nu+2}{2}; \frac{\beta^2 z^2}{4}\right) \left\{\beta I_{\nu+1}(\beta z) + \frac{\gamma+A}{z} I_\nu(\beta z)\right\} \right. \\ & \left. + {}_1F_2\left(\frac{\gamma-\nu+2}{2}; -\nu+2, \frac{\gamma-\nu+4}{2}; \frac{\beta^2 z^2}{4}\right) \frac{\beta^2 z}{2} \frac{(\gamma-\nu)(-\nu+1)}{(\gamma-\nu+2)} I_\nu(\beta z) \right] \end{aligned} \tag{3.27}$$

Replacing the derivative in (3.22) and after some mathematical manipulations, the following equation can be obtained:

$$C_1\, T_{21} + C_2\, T_{22} = T_{23} \tag{3.28}$$

Where,

$$T_{21}(z)=\left[MN_{d0}^{-m}V_T\alpha z^{\left(\frac{-2m}{m+k}\right)}\left\{(1-f)P_1(z)+\left(\frac{m+k}{2}\right)zX_1(z)\right\}-S_pP_1(z)\right] \tag{3.29}$$

$$T_{22}(z)=\left[MN_{d0}^{-m}V_T\alpha z^{\left(\frac{-2m}{m+k}\right)}\left\{(1-f)P_2(z)+\left(\frac{m+k}{2}\right)zX_2(z)\right\}-S_pP_2(z)\right] \tag{3.30}$$

$$T_{23}(z)=\left[S_pP_3(z)-MN_{d0}^{-m}V_T\alpha z^{\left(\frac{-2m}{m+k}\right)}\left\{(1-f)P_3(z)+\left(\frac{m+k}{2}\right)zX_3(z)\right\}\right] \tag{3.31}$$

The simplified equations obtained from the boundary conditions give the coefficient C_1 and C_2.

$$C_1=\frac{\left(\frac{n_i^2}{N(z_j)}\exp\left(\frac{V}{V_T}\right)-P_3(z_j)\right)T_{22}(z_0)-P_2(z_j)T_{23}(z_0)}{P_1(z_j)T_{22}(z_0)-T_{21}(z_0)P_2(z_j)} \tag{3.32}$$

$$C_2=\frac{P_1(z_j)T_{23}(z_0)-T_{21}(z_0)\left(\frac{n_i^2}{N(z_j)}\exp\left(\frac{V}{V_T}\right)-P_3(z_j)\right)}{P_1(z_j)T_{22}(z_0)-T_{21}(z_0)P_2(z_j)} \tag{3.33}$$

These simplified equations obtained from the boundary conditions give the coefficient C_1 & C_2. Replacing C_1 & C_2 back in equation (3.19) results in a complete analytical expression of Hole profile p(z) for non-uniformly doped emitter of DF solar cell.

$$\begin{aligned} p(z)=&\overbrace{\left[\underbrace{\frac{\frac{n_i^2}{N_d(z_j)}\exp\left(V/V_T\right)}{P_1(z_j)-\frac{T_{21}(z_0)}{T_{22}(z_0)}P_2(z_j)}}_{\text{Contribution from Biasing}}+\underbrace{\frac{T_{23}(z_0)+\frac{T_{22}(z_0)}{P_2(z_j)}P_3(z_j)}{T_{21}(z_0)-\frac{T_{22}(z_0)}{P_2(z_j)}P_1(z_j)}}_{\text{Contribution from Spectrum}}\right]}^{C_1}z^AI_v(\beta z)\\ &+\overbrace{\left[\underbrace{\frac{\frac{n_i^2}{N_d(z_j)}\exp\left(V/V_T\right)}{P_2(z_j)-\frac{T_{22}(z_0)}{T_{21}(z_0)}P_1(z_j)}}_{\text{Contribution from Biasing}}+\underbrace{\frac{P_1(z_j)\frac{T_{23}(z_0)}{T_{21}(z_0)}+P_3(z_j)}{\frac{T_{22}(z_0)}{T_{21}(z_0)}P_1(z_j)-P_2(z_j)}}_{\text{Contribution from Spectrum}}\right]}^{C_2}z^AI_{-v}(\beta z)\\ &+\underbrace{P_3(z)}_{\text{Illumination term}} \end{aligned} \tag{3.34}$$

Equation (3.34) is the final expression of minority carrier obtained in terms of z. This is the key equation of our compact analytical model.

3.3. Analytical Model For Minority Carrier Electron Density

The model that describes the minority carrier hole can be extended for electron by modifying the equations (3.1)–(3.7). The drift-diffusion equations for excess electron is–

$$J_n(x) = J_{diffusion}(x) + J_{drift}(x) = qD_n \frac{dn}{dx} + q\mu n E \tag{3.35}$$

$$\frac{dJ_n}{dx} = q\frac{n}{\tau_n} - qG \tag{3.36}$$

The lifetime and mobility for electron have similar equations as that of for hole, but obviously the fitting parameters K, k, M and m will be different for equation (3.4)-(3.5). For successful matching of electron recombination lifetime in p-type silicon with available experimental data [31], K = 10^{31} cm^{-6}s and k = 2 results in a reasonably good fit. Similar fitting parameter is reported in [64] for electron mobility (M = 1.1×10^{10} $\text{cm}^{0.74}$ $\text{V}^{-1}\text{s}^{-1}$ and m = 0.42). As already discussed in chapter 2, these fitting parameters give good approximation for wide range of doping and hence this equation will be used in our derivation too. The induced electric field inside the device due to non-uniform acceptor doping and band gap narrowing will be considered by the following equation:

$$E = V_T \frac{d\ln N}{dx} + \frac{1}{q}\frac{d\Delta E_G}{dx} \tag{3.37}$$

Considering above equations, the minority carrier electron concentration (n) can be expressed in terms of doping N.

$$\begin{aligned} &\frac{d^2 n}{dx^2} + \underbrace{(1+f-m)}_{\text{Different}} \frac{dn}{dx}\frac{d\ln N}{dx} - \left(\underbrace{m(1+f)}_{\text{Different}} \left(\frac{d\ln N}{dx}\right)^2 \underbrace{-(1+f)}_{\text{Different}} \frac{d^2 \ln N}{dx^2} + \frac{N^{m+k}}{KMV_T} \right) n \\ &\qquad = -\left(\frac{N^m}{MV_T}\right)\sum_{i=1}^{5} a_i e^{-b_i x} \end{aligned} \tag{3.38}$$

This second-order non-homogeneous differential equation is slightly different to that of hole equation. As compared to hole transport equation in (3.9), the terms that have changed is indicated in equation (3.38). It should be noted that the difference is mainly in the expression of the electric field. Placing the expression of exponential doping N(x) into the continuity equation (3.38) results in equation (3.39).

$$\frac{d^2n}{dx^2}-\alpha(1+f-m)\frac{dn}{dx}-\left(m(1+f)\alpha^2+\frac{N_{d0}{}^{m+k}e^{-\alpha(m+k)x}}{KMV_T}\right)n \\ =-\left(\frac{N_{d0}{}^{m}e^{-\alpha mx}}{MV_T}\right)\sum_{i=1}^{5}a_i e^{-b_i x} \tag{3.39}$$

After substituting $z=\exp\left[-\alpha(m+k)x/2\right]$ in (3.39) and then $\mathrm{n}(\mathrm{z})=z^{-A}u(z)$, a modified Bessel Equation is obtained in equation (3.40), with non-integer order of $\nu=\sqrt{4m(1+f)+(m-f-1)^2}\big/(m+k)$.

$$z^2\frac{d^2u}{dz^2}+z\frac{du}{dz}-\left(\beta^2z^2+\nu^2\right)u=-\sum_{i=1}^{5}C_i z^\gamma \tag{3.40}$$

Here, all the constants are same as those for Hole concentration, except the following three constants –

$$A=\left(\frac{m-f-1}{m+k}\right) \tag{3.41}$$

$$\kappa=\frac{2\sqrt{m(1+f)}}{m+k} \tag{3.42}$$

$$\gamma=\left(D_i+A\right) \tag{3.43}$$

The complete solution of this inhomogeneous equation is obtained in terms of modified Bessel function of first kind.

$$n(z)=n_1(z)\;C_1+n_2(z)\;C_2+n_3(z) \tag{3.44}$$

With,

$$n_1(z)=z^{-A}I_\nu(\beta z)\,;\;n_2(z)=z^{-A}I_{-\nu}(\beta z)$$

$$n_3(z)=-\sum_{i=1}^{5}\frac{E_i\pi}{2\sin(\pi\nu)}\times z^{-A}$$

$$\left[I_\nu(\beta z)\frac{2^\nu(\beta z)^{\gamma-\nu}}{(\gamma-\nu)\Gamma(-\nu+1)}\,{}_1F_2\left(\frac{\gamma-\nu}{2};-\nu+1,\frac{\gamma-\nu+2}{2};\frac{\beta^2z^2}{4}\right)\right.$$
$$\left.-I_{-\nu}(\beta z)\frac{2^{-\nu}(\beta z)^{\gamma+\nu}}{(\gamma+\nu)\Gamma(\nu+1)}\,{}_1F_2\left(\frac{\gamma+\nu}{2};\nu+1,\frac{\gamma+\nu+2}{2};\frac{\beta^2z^2}{4}\right)\right]$$

Note that $n_3(z)$ is the almost same as $p_3(z)$ in (3.20), except z^{-A} term. If a p-type emitter of p-n DF solar cell is considered for analysis now, the modified boundary condition will be –

At Emitter-Base Junction: $n\left(x_j\right)=\frac{n_i^2}{N(x_j)}\exp\left(\frac{V}{V_T}\right)$ (3.45)

At the Emitter Surface: $\left[\mu(x)En(x)+D_n\left(x\right)\frac{dn(x)}{dx}\right]_{x=0}=-S_n n\left(0\right)$ (3.46)

$\left[dn(z)/dz\right]$ will have the same form as (3.23), except that constant A will be replaced by –A in X_1, X_2 and X_3.

$$\frac{dn(z)}{dz}=X_1(z)\,C_1+X_2(z)\,C_2+X_3(z) \tag{3.47}$$

Application of above identity of (3.47) in boundary condition of (3.46) results in the following equation –

$$C_1\,T_{11}+C_2\,T_{12}=T_{13} \tag{3.48}$$

The coefficient C_1 and C_2 are almost identical to (3.32)-(3.33). Of course, T_{11}, T_{12} and T_{13} will have slight change because of the difference in electric field and electron current equation, when compared to the expression of hole concentration.

$$T_{11}(z)=\left[MN_{d0}^{-m}V_T\alpha z^{\left(\frac{-2m}{m+k}\right)}\left\{-(1+f)n_1(z)-\left(\frac{m+k}{2}\right)zX_1(z)\right\}+S_n n_1\left(z\right)\right] \tag{3.49}$$

$$T_{12}(z)=\left[MN_{d0}^{-m}V_T\alpha z^{\left(\frac{-2m}{m+k}\right)}\left\{-(1+f)n_2(z)-\left(\frac{m+k}{2}\right)zX_2(z)\right\}+S_n n_2(z)\right] \tag{3.50}$$

$$T_{13}(z)=\left[-S_n n_3(z)-MN_{d0}^{-m}V_T\alpha z^{\left(\frac{-2m}{m+k}\right)}\left\{-(1+f)n_3(z)-\left(\frac{m+k}{2}\right)zX_3(z)\right\}\right] \tag{3.51}$$

From the above derivation for electron concentration, it can be concluded that the expression for electron concentration is quite similar to hole concentration, with some change in constants and signs. Hence from now on, any discussion on hole concentration will be equally applicable to electron concentration without the loss of generality and vice versa. But if for any case, the analysis of electron and hole transport needs separate attention, then both analysis will be discussed distinctively.

3.4. Carrier Concentration For Exponentially Increasing Doping

The analytical model developed for exponentially decreasing doping profile can be easily expanded for exponentially increasing profile. But it is not that simple like replacing $-\alpha$ with α, as that might result in negative values of certain constants and imaginary arguments of special functions. Hence, properly addressing this modification is necessary. This section will investigate this modified expression when doping is exponentially increasing.

The exponentially increasing doping can be converted into exponentially decreasing doping by reversing the x axis, as evident from fig. 3.2 below. In that case, the solution developed in the previous section seems to work fine for this case too. But one approximation needs to be revisited. The carrier generation approximation is defined by exponentially dependent terms, i.e., $G(x) = \sum a_i e^{-b_i x}$, which works for *increasing x* only. The alternative way is to re-derive the whole solution taking $N(x) = N_{d0}\exp(\alpha x)$. Hence, there are actually two ways to solve the problem:

- Reverse the x axis. Consequently, calculate the 10 coefficients (a_1, a_2, a_3, a_4, a_5, and b_1, b_2, b_3, b_4, b_5) of exponentially increasing G(x), which is tough to calculate.
- Re-derive and make some change in constants.

This thesis will take the second approach. Since all the derivations are at hand, inserting this increasing doping profile and changing the corresponding Bessel and Hypergeometric equation seem easier.

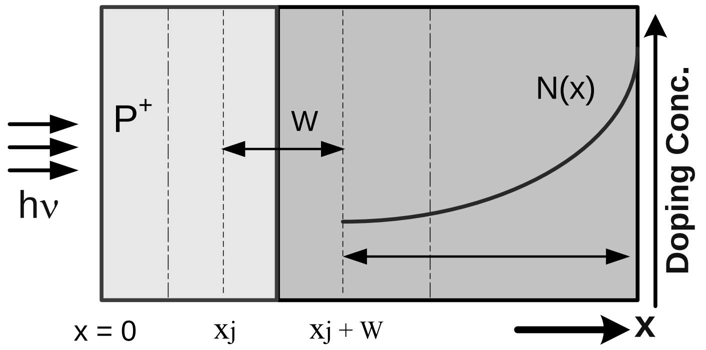

Fig. 3.2. Exponentially increasing doping in base region of a p^+-n(x) cell

It is quite straightforward to get the following transport equation,

$$\frac{d^2p}{dx^2}+\alpha(1-m-f)\frac{dp}{dx}-\left(m(1-f)\alpha^2+\frac{{N_{d0}}^{m+k}e^{\alpha(m+k)x}}{KMV_T}\right)p=-\left(\frac{{N_{d0}}^{m}e^{\alpha mx}}{MV_T}\right)\sum_{i=1}^{5}a_ie^{-b_ix}$$

The variable transfer will now be z = exp[α(m+k)x/2]. The solution is same as (3.19), with the change in following constants –

$$D_i=\frac{2(-b_i+\alpha m)}{\alpha(m+k)}$$

$$\gamma=\left(D_i+A\right)$$

Besides, all occurrence of A will be replaced with –A. The boundary conditions for the device in fig. 3.2 are for the base junction-edge and the back interface. The surface boundary condition will need the derivatives of p(z). The second condition will end up in same equation with the following slight change –

$$T_{21}(z)\Big|_{\text{Back Surface}}=\left[MN_{d0}^{-m}V_T\alpha z^{\left(\frac{-2m}{m+k}\right)}\left\{-(1-f)P_1(z)-\left(\frac{m+k}{2}\right)zX_1(z)\right\}-S_pP_1(z)\right]$$

$$T_{22}(z)\Big|_{\text{Back Surface}}=\left[MN_{d0}^{-m}V_T\alpha z^{\left(\frac{-2m}{m+k}\right)}\left\{-(1-f)P_2(z)-\left(\frac{m+k}{2}\right)zX_2(z)\right\}-S_pP_2(z)\right]$$

$$T_{23}(z)\Big|_{\text{Back Surface}}=\left[S_pP_3(z)-MN_{d0}^{-m}V_T\alpha z^{\left(\frac{-2m}{m+k}\right)}\left\{-(1-f)P_3(z)-\left(\frac{m+k}{2}\right)zX_3(z)\right\}\right]$$

The analysis for electron concentration is similar and hence will not be discussed here.

3.5. Close Inspection of the Derived Solution

The solution for hole concentration is repeated here for discussion:

$$
\begin{aligned}
p(z) = {} & \overbrace{\left[\underbrace{\frac{\frac{n_i^2}{N_d(z_j)}\exp\left(V/V_T\right)}{P_1(z_j)-\frac{T_{21}(z_0)}{T_{22}(z_0)}P_2(z_j)}}_{\text{Contribution from Biasing}} + \underbrace{\frac{T_{23}(z_0)+\frac{T_{22}(z_0)}{P_2(z_j)}P_3(z_j)}{T_{21}(z_0)-\frac{T_{22}(z_0)}{P_2(z_j)}P_1(z_j)}}_{\text{Contribution from Spectrum}} \right]}^{C_1} z^A I_\nu(\beta z) \\
& + \overbrace{\left[\underbrace{\frac{\frac{n_i^2}{N_d(z_j)}\exp\left(V/V_T\right)}{P_2(z_j)-\frac{T_{22}(z_0)}{T_{21}(z_0)}P_1(z_j)}}_{\text{Contribution from Biasing}} + \underbrace{\frac{P_1(z_j)\frac{T_{23}(z_0)}{T_{21}(z_0)}+P_3(z_j)}{\frac{T_{22}(z_0)}{T_{21}(z_0)}P_1(z_j)-P_2(z_j)}}_{\text{Contribution from Spectrum}} \right]}^{C_2} z^A I_{-\nu}(\beta z) \\
& + \underbrace{P_3(z)}_{\text{Illumination term}}
\end{aligned}
\tag{3.52}
$$

As seen from the compact expression above, the contribution from biasing and dark component, variable doping, surface states and spectrum response can be identified and separately analyzed for optimizing cell design. The success of this work is that together all these contributions, as well as their inter-dependence can be explored effectively using one unified expression of minority carrier.

In the results section, the change in the contributions under dark condition and light condition will be discussed. In [8], influence of spectrum is totally overlooked. Our solution simply reduces to the expression developed by Verhoef and Sinke [8], when contribution from spectrum is discarded in equation (3.52).

From the above equation, it is evident that the boundary conditions will change greatly when light in incident on the cell. The amount of change is reflected in the spectrum contribution parts of C_1 and C_2. Aside from these terms, there is also a constant illumination term $P_3(x)$, which is independent of boundary conditions; rather it depends on position x (through z), generation (through ai, bi), and transport parameters (through m, M, k, K). This is important because effects from biasing and surface recombination velocity comes to the compact solution only through boundary condition and affect the constants, not P_3. Hence, $P_3(x)$ will be independent of biasing and surface recombination velocity. This finding is consistent with the existing theory of solar cell. It is obvious from this analytical model that the illumination term can be considered as a superimposed current source with the p-n junction dark current, as normally seen in equivalent circuit of solar cell (see fig. 2.7).

3.6. Minority Carrier Current Density

The minority carrier hole current variation with depth is easily obtainable from equation (3.1). The diffusion component of the current can be obtained using the derivative of solution, as given below –

$$J_{P-Diffusion}(z) = \underbrace{C_1\left[qMN_{d0}^{-m}V_T\alpha z^{\left(\frac{k-m}{m+k}\right)}\left(\frac{m+k}{2}\right)X_1(z)\right] + C_2\left[qMN_{d0}^{-m}V_T\alpha z^{\left(\frac{k-m}{m+k}\right)}\left(\frac{m+k}{2}\right)X_2(z)\right]}_{\text{Dark Component}} + \underbrace{\left[qMN_{d0}^{-m}V_T\alpha z^{\left(\frac{k-m}{m+k}\right)}\left(\frac{m+k}{2}\right)X_3(z)\right]}_{\text{Contribution from Solar Spectrum}} \tag{3.53}$$

The drift component, depending on the E(x), can be described by –

$$J_{P-Drift}(z) = \underbrace{C_1\left[qMN_{d0}^{-m}V_T\alpha z^{\left(\frac{-2m}{m+k}\right)}(1-f)P_1(z)\right] + C_2\left[qMN_{d0}^{-m}V_T\alpha z^{\left(\frac{-2m}{m+k}\right)}(1-f)P_2(z)\right]}_{\text{Dark Response}} + \underbrace{\left[qMN_{d0}^{-m}V_T\alpha z^{\left(\frac{-2m}{m+k}\right)}(1-f)P_3(z)\right]}_{\text{Contribution from Solar Spectrum}} \tag{3.54}$$

Total hole current density will be the summation of drift and diffusion components. As seen in the equations above, the specific contribution from the spectrum can be separately identified in the expression of current. This is noteworthy because we can focus on certain parts of the solution to propose more effective designs and reduce pitfalls that are responsible in reducing current.

The expression for electron current density is not mentioned here, since that is quite similar to hole current density.

3.7. Two Layer Model

The model developed in previous sections covers electron and hole concentration in p-type and n-type emitter/base respectively. But the solar cell structure of fig. 3.1 or fig. 3.2 is quite simple in design. In practical solar cell, the diffusion region of the emitter may be accompanied by another diffusion region having either uniform or non-uniform doping. Similarly, the base region may be followed by a Base Surface Field (BSF) layer that changes the effective surface recombination at the back contact. These improvements are often employed in optimizing the cell performance. So, in this section, a two layer model will be attempted that will make this analysis applicable to multiple-layer solar cells. Besides, uniform doping will be consider for one of the emitter segments, so that the derivation for this case of doping can be presented along the way.

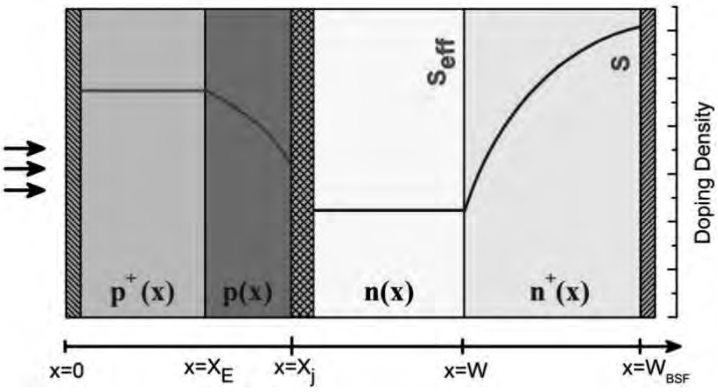

Fig. 3.3. A DF (Drift Field) solar cell structure with additional diffusion layer at the emitter and a BSF layer at the back side: Base (n-type) is uniformly doped and doping density in BSF increases exponentially from n-n+ interface (at x=W) to back surface ($x=W_{BSF}$). S_{eff} is the effective surface recombination velocity for n-n+ interface

The cell structure for the two-layer model is shown in fig. 3.3. The two-segment emitter layer will be considered first. The transport equation for uniform doping can be derived as a special case of equation (3.38), by removing all the derivatives containing doping concentration in it.

$$\frac{d^2n}{dx^2}+(1+f-m)\frac{dn}{dx}-\left(\frac{N_A^{\;m+k}}{KMV_T}\right)n=-\left(\frac{N_A^{\;m}}{MV_T}\right)\sum_{i=1}^{5}a_ie^{-b_ix} \qquad (3.55)$$

The solution of this differential equation is quite simple one, as seen below.

$$n_1(x) = C_1 \exp\left(\beta_u x\right) + C_2 \exp\left(-\beta_u x\right) - \left(\frac{N_A^{\ m}}{MV_T}\right) \sum_{i=1}^{5} \left(\frac{a_i}{b_i^2 - \beta_u^{\ 2}}\right) \exp(-b_i x) \quad (3.56)$$

$$\text{or,} \quad n_1(z) = n_{11}(z)\, C_1 + n_{12}(z)\, C_2 + n_{13}(z) \quad (3.57)$$

Here, $\beta_u = \sqrt{\frac{N_{d0}^{\ m+k}}{KMV_T}}$ is the modified β for uniform case. For the exponential doped part of emitter, the solution in terms of z is same as discussed in equation (3.44), with the unknown constants D_1 and D_2.

$$n_2(z) = n_{21}(z)\, D_1 + n_{22}(z)\, D_2 + n_{23}(z) \quad (3.58)$$

At this point, there are two solutions, $n_1(x)$ and $n_2(x)$, at each segment of the emitters. For determining the four constants C_1, C_2, D_1 and D_2, total 4 equations are necessary. The boundary condition at top surface (x=0) and at the E-B junction ($x=X_j$) are standard boundary conditions used for single-layer solar cell in previous section 3.2. The rest of the conditions are obtained from the continuity of excess minority carrier concentration and continuity of current density at the boundary located at $x=X_E$. Note that S_n will have negative value, since it is opposite to the x direction (S_n is for top surface). All the boundary conditions are –

- At the E-B junction:

$$n_2\left(z_j\right) = \frac{n_i^2}{N_A(z_j)} \exp\left(\frac{V}{V_T}\right) \quad (3.59)$$

- At the top surface:

$$-\left[\mu(x) E n_1(x) + D_n(x) \frac{dn_1(x)}{dx}\right]_{x=0,\, z=z_0} = -S_n n_1\left(z_0\right) \quad (3.60)$$

- Carrier continuity at the intermediate region ($x = X_E$):

$$n_1(z_E) = n_2(z_E) \quad (3.61)$$

- Current continuity at the intermediate region ($x = X_E$):

$$\left[\mu(x) E n_1(x) + D_n(x) \frac{dn_1(x)}{dx}\right]_{x=x_E,\, z=z_E} = \left[\mu(x) E n_2(x) + D_n(x) \frac{dn_2(x)}{dx}\right]_{x=x_E,\, z=z_E} \quad (3.62)$$

By placing (3.56)-(3.58) into equations (3.59)-(3.62) above, four sets of linear equations containing C_1, C_2, D_1 and D_2 can be obtained. T_{11}, T_{12}, T_{13} are same as (3.49)-(3.51), with the only exception that there will be a negative sign before each S_n.

- At the E-B junction:

$$D_1 n_{21}(z_j) + D_2 n_{22}(z_j) = \frac{n_i^2}{N_A(z_j)} \exp\left(\frac{V}{V_T}\right) - n_{23}(z_j) \tag{3.63}$$

- At the top surface:

$$\mathrm{C}_1\,\mathrm{T}_{11}(\mathrm{z}_0) + \mathrm{C}_2\,\mathrm{T}_{12}(\mathrm{z}_0) = \mathrm{T}_{13}(\mathrm{z}_0) \tag{3.64}$$

- Current continuity at the intermediate region ($x = X_E$):

$$\begin{aligned} &C_1\left[\left(\frac{m+k}{2}\right) z_E X_{11}(z_E) + (1+f)n_{11}\right] + C_2\left[\left(\frac{m+k}{2}\right) z_E X_{12}(z_E) + (1+f)n_{12}\right] \\ &+\left[\left(\frac{m+k}{2}\right) z_E X_{13}(z_E) + (1+f)n_{13}\right] = D_1\left[\left(\frac{m+k}{2}\right) z_E X_{21}(z_E) + (1+f)n_{21}\right] \\ &+D_2\left[\left(\frac{m+k}{2}\right) z_E X_{22}(z_E) + (1+f)n_{22}\right] + \left[\left(\frac{m+k}{2}\right) z_E X_{23}(z_E) + (1+f)n_{23}\right] \end{aligned}$$

$$\Rightarrow \quad C_1\,Y_{11} + C_2\,Y_{12} + Y_{13} = D_1\,Y_{21} + D_2\,Y_{22} + Y_{23} \tag{3.65}$$

- Carrier continuity at the intermediate region ($x = X_E$):

$$C_1\,n_{11}(z_E) + C_2\,n_{12}(z_E) + n_{13}(z_E) = D_1\,n_{21}(z_E) + D_2\,n_{22}(z_E) + n_{23}(z_E) \tag{3.66}$$

After some mathematical manipulation, C_1, C_2, D_1 and D_2 can be obtained as follows–

$$\begin{aligned} C_2 = &\frac{\left\lfloor T_{11}\left\{Y_{23} - Y_{13} + \frac{Y_{21}}{n_{21}(Z_j)}\left(\frac{n_i^2}{N_A(Z_j)} e^{V/V_T} - n_{23}(Z_j)\right)\right\} - T_{13}Y_{11}\right\rfloor}{\left(T_{11}Y_{12} - T_{12}Y_{11}\right) - \left\{\frac{\left[T_{11}n_{12}(Z_E) - T_{12}n_{11}(Z_E)\right]\left[n_{22}(Z_j)Y_{21} - Y_{22}n_{21}(Z_j)\right]}{n_{22}(Z_j)n_{21}(Z_E) - n_{22}(Z_E)n_{21}(Z_j)}\right\}} \\ &+ \frac{\left[T_{11}\left\{n_{23}(z_E) - n_{13}(Z_E) + \frac{n_{21}(Z_E)}{n_{21}(Z_j)}\left(\frac{n_i^2}{N_A(Z_j)} e^{V/V_T} - n_{23}(Z_j)\right)\right\} - T_{13}n_{11}(Z_E)\right]}{\left[T_{11}n_{12}(Z_E) - T_{12}n_{11}(Z_E)\right] - \left\{\frac{\left[T_{11}Y_{12} - T_{12}Y_{11}\right]\left[n_{22}(Z_j)n_{21}(Z_E) - n_{22}(Z_E)n_{21}(Z_j)\right]}{n_{22}(Z_j)Y_{21} - Y_{22}n_{21}(Z_j)}\right\}} \end{aligned}$$

$$C_1 = \frac{T_{13} - C_2T_{12}}{T_{11}}$$

$$D_2 = \frac{n_{21}(x_j)\left\{n_{23}(Z_E) - n_{13}(Z_E) + \frac{T_{13}}{T_{11}} n_{11}(Z_E)\right\} + n_{21}(Z_E)\left(\frac{n_i^2}{N_A(Z_j)} e^{v/V_T} - n_{23}(Z_j)\right)}{\left[n_{22}(Z_j)n_{21}(Z_E) - n_{22}(Z_E)n_{21}(Z_j)\right] - \left\{\frac{\left[T_{11}n_{12}(Z_E) - T_{12}n_{11}(Z_E)\right]\left[n_{22}(Z_j)Y_{21} - Y_{22}n_{21}(Z_j)\right]}{\left(T_{11}Y_{12} - T_{12}Y_{11}\right)}\right\}}$$

$$+ \frac{n_{21}(Z_j)\left\{Y_{23} - Y_{13} + \frac{T_{13}Y_{11}}{T_{11}}\right\} + T_{21}\left(\frac{n_i^2}{N_A(Z_j)} e^{v/V_T} - n_{23}(Z_j)\right)}{\left[n_{22}(Z_j)Y_{21} - Y_{22}n_{21}(Z_j)\right] - \left\{\frac{\left[T_{11}Y_{12} - T_{12}Y_{11}\right]\left[n_{22}(Z_j)n_{21}(Z_E) - n_{22}(Z_E)n_{21}(Z_j)\right]}{\left[T_{11}n_{12}(Z_E) - T_{12}n_{11}(Z_E)\right]}\right\}}$$

$$D_1 = \frac{\left(\frac{n_i^2}{N_A(Z_j)} e^{v/V_T} - n_{23}(Z_j)\right) - D_2 n_{22}(Z_j)}{n_{21}(Z_j)}$$

The terms responsible for the effect from solar spectrum are n_{13}, Y_{13} and T_{13}. The other terms in the numerator are from the dark response and the effect from the applied bias. For example, the constant C_2 can be divided into following parts –

$$C_2 = \underbrace{\frac{\overbrace{\left(T_{11}Y_{23} - T_{11}Y_{13} - T_{13}Y_{11} - \frac{T_{11}Y_{21}}{n_{21}(Z_j)} n_{23}(Z_j)\right)}^{\text{Contribution from solar illumination}} + \overbrace{\frac{T_{11}Y_{21}}{n_{21}(Z_j)} \frac{n_i^2}{N_A(Z_j)} e^{V/V_T}}^{\text{Contribution from biasing}}}{\left(T_{11}Y_{12} - T_{12}Y_{11}\right) - \left\{\frac{\left[T_{11}n_{12}(Z_E) - T_{12}n_{11}(Z_E)\right]\left[n_{22}(Z_j)Y_{21} - Y_{22}n_{21}(Z_j)\right]}{n_{22}(Z_j)n_{21}(Z_E) - n_{22}(Z_E)n_{21}(Z_j)}\right\}}}_{\text{From the Dark Response}}$$

$$+ \underbrace{\frac{\overbrace{\left(T_{11}n_{23}(z_E) - T_{11}n_{13}(Z_E) - T_{13}n_{11}(Z_E) - \frac{T_{11}n_{21}(Z_E)}{n_{21}(Z_j)} n_{23}(Z_j)\right)}^{\text{Contribution from solar illumination}} + \overbrace{\frac{T_{11}n_{21}(Z_E)}{n_{21}(Z_j)} \frac{n_i^2}{N_A(Z_j)} e^{V/V_T}}^{\text{Contribution from biasing}}}{\left[T_{11}n_{12}(Z_E) - T_{12}n_{11}(Z_E)\right] - \left\{\frac{\left[T_{11}Y_{12} - T_{12}Y_{11}\right]\left[n_{22}(Z_j)n_{21}(Z_E) - n_{22}(Z_E)n_{21}(Z_j)\right]}{n_{22}(Z_j)Y_{21} - Y_{22}n_{21}(Z_j)}\right\}}}_{\text{From the Dark Response}}$$

Replacing them into (3.56)-(3.58) will result in general equation for minority carrier concentration in a double-layer p-type emitter. For a double layer n-type base, the development will be similar, with the obvious exception of using the constants for hole concentration developed in section 3.1.

3.8. A General Analytical Model

In this section, the previously developed model will be expanded to a more general level. Instead of actual generation rate, our previous approach uses approximated rate. The generation term is approximated by three/five position-dependent terms in $a_i exp(-b_i\, x)$. Although the validity of using approximated G is well-established, inclusion of this approximation is certainly a loss of accuracy. Moreover, the effect of individual wavelength is not explicitly expressed in the compact model. In this section, this idea of incorporating the effect of each wavelength in the general expression will be explored. If correctly developed, this solution will be able to predict the collection efficiency (i.e. the spectral response for constant number of photons) as a function of wavelength.

The traditional approach of obtaining the light generation term G is to use the numerical data for light intensities (ΔE_0) incident on a unit area within a bandwidth ($\Delta\lambda$).

$$\Delta E_0(\lambda) = \frac{dE(\lambda)}{d\lambda}\Delta\lambda \tag{3.67}$$

Here, $dE(\lambda)/d\lambda$ is the spectral irradiance (in $\mathrm{Wcm^{-2}\mu m^{-1}}$). The incident photon density can be calculated from the light intensity [57] by the following relationship –

$$\Delta N_0(\lambda) = \frac{\lambda}{hc}\Delta E_0(\lambda) = \left(\frac{\lambda}{hc}\right)\left(\frac{dE(\lambda)}{d\lambda}\right)\Delta\lambda \tag{3.68}$$

Since the silicon layer will absorb the incident photon density along the depth, the change in photon flux can be expressed by the exponential relationship in equation (3.69),

$$\Delta N(\lambda, x) = \Delta N_0(\lambda)\exp\left[-\alpha_{\mathrm{Si}}(\lambda)x\right] \tag{3.69}$$

The absorption coefficient (α_{Si}) determines the amount of light absorbed by any absorbing material. α_{Si} is generally expressed in $\mathrm{cm^{-1}}$. The rate of change in photon density can be obtained simply by differentiating (3.69). If each absorbed photon produces one electron-hole-pair, then the rate of decreasing photo density is equal to the generation rate (Δg) of EHP for $\Delta\lambda$.

$$\begin{aligned}\Delta g(\lambda,x) &= -\left(\frac{d\Delta N}{dx}\right) = \alpha_{\mathrm{Si}}\ \Delta \mathrm{N}_0 \exp\left(-\alpha_{\mathrm{Si}} x\right) \\ &= \alpha_{\mathrm{Si}} \Delta N_0(\lambda) \exp\left[-\alpha_{\mathrm{Si}}(\lambda) x\right] \\ &= \alpha_{\mathrm{Si}} \left(\frac{\lambda}{hc}\right)\left(\frac{dE_i(\lambda)}{d\lambda}\right) \exp\left(-\alpha_{\mathrm{Si}} x\right) \Delta\lambda \end{aligned} \tag{3.70}$$

The total generation rate G(λ, x) is equal to the sum of all the generation terms from each Δλ range, as given below by (3.71).

$$G(\lambda,x) = \sum_{i=1}^{n} \alpha_{\mathrm{Si}}(i) \overbrace{\left(\frac{\lambda_i}{hc}\right) \underbrace{\left(\frac{dE_i(\lambda)}{d\lambda}\right)}_{\text{Spectral Irradiance}} \Delta\lambda_i}^{\Delta N_0(\lambda)} \exp\left[-\alpha_{\mathrm{Si}}(i) x\right] \tag{3.71}$$

From the above equation, it is clear that the contribution from G(λ, x) can be incorporated in the transport equation by considering each term separately over a certain Δλ range. Afterwards, summing all the contribution will give the total light-generated current.

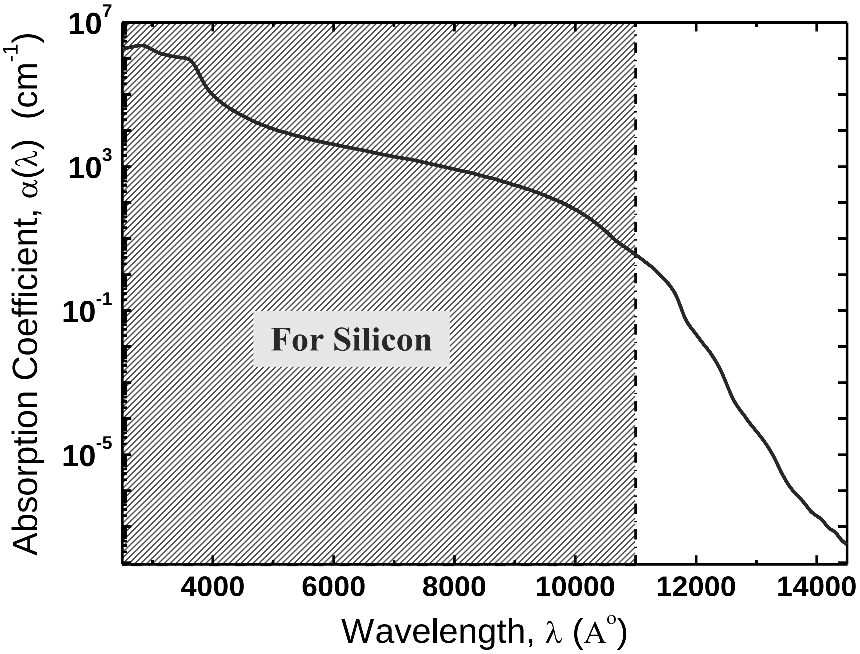

Fig. 3.4. Absorption coefficient for Silicon [65], The green shading indicates the region where the absorption is dominant for Si.

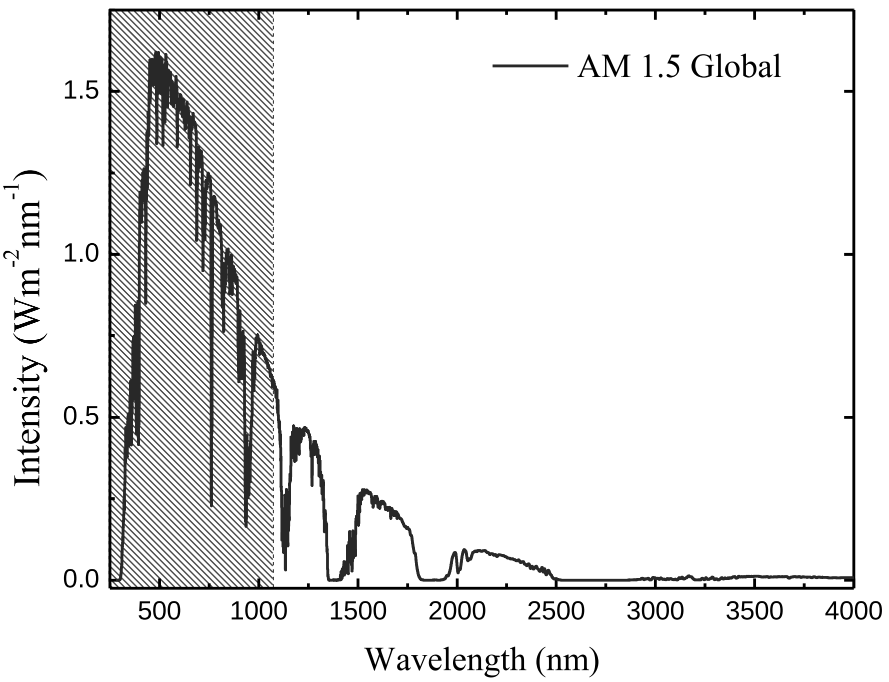

Fig. 3.5. Solar spectral irradiance for AM1.5G [66]. The green shading indicates portion of spectrum mainly used by Si absorbing layer.

As already discussed, the generation term depends on intensity (photon-flux) and absorption coefficient [66]. These quantities are already available (see fig. 3.4-3.5). The generation rate can be calculated using equation (3.71) (see fig. 3.6).

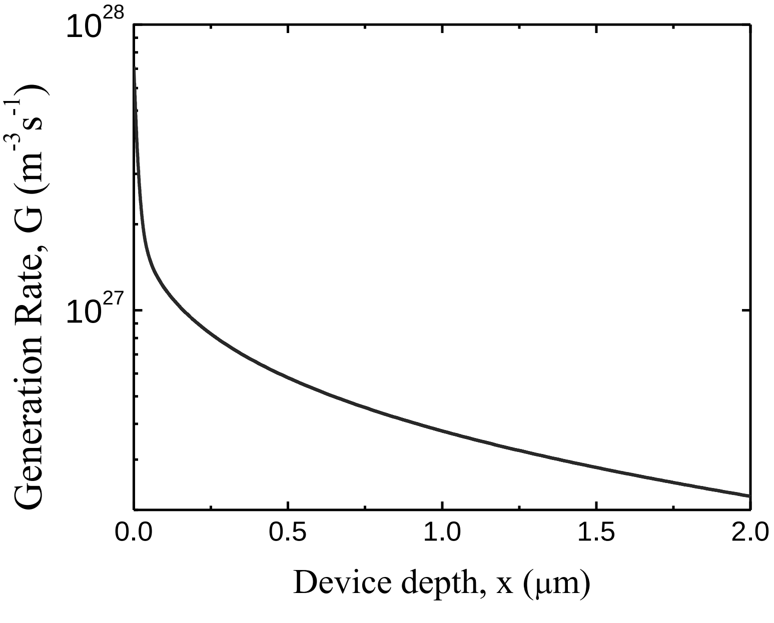

Fig. 3.6. Carrier Generation in Si obtained from the absorption data in fig. 3.4 and from the spectrum data in fig. 3.5.

The important thing to note here is that actual G(λ, x) has similar exponential dependence on x, like approximated G(x) in equation (3.3). The comparison is shown in the table 3.1 below.

Table 3.1. Comparison between Approximated Generation Rate and Actual Generation Rate

Approximated Generation Rate	Actual Generation Rate
$G_{\text{approx.}}(x)=\sum_{i=1}^{5}\mathrm{a}_{\mathrm{i}}\exp\left[-b_i x\right]$	$G(\lambda,x)=\sum_{i=1}^{n}\underbrace{\left[\alpha_{\mathrm{Si}}(i)\Delta N_0(\lambda)\right]}_{\mathrm{a_i}}\exp\left[-\underset{\mathrm{b_i}}{\alpha_{\mathrm{Si}}(i)}\,x\right]$

Instead of 5 terms in $G_{\text{approx.}}$, total number of terms in G(λ,x) will now depend on the considered range of wavelength. Equation (3.71) will now be used in drift-diffusion equation.

$$\frac{d^2p}{dx^2}-(m+f-1)\frac{dp}{dx}\frac{d\ln N}{dx}-\left(m(1-f)\left(\frac{d\ln N}{dx}\right)^2+(f-1)\frac{d^2\ln x}{dx^2}+\frac{N^{m+k}}{KMV_T}\right)p$$
$$=-\left(\frac{N^m}{MV_T}\right)\sum_{i=1}^{N}\alpha_{Si}\Delta N_0(\lambda)e^{-\alpha_{Si}x} \qquad (3.72)$$

This equation is very similar to (3.9), if the following generation constants are redefined (see Table 3.1),

$$a_i=\alpha_{Si}\,\Delta\mathrm{N}_0(\lambda) \qquad (3.73)$$

$$b_i=\alpha_{Si} \qquad (3.74)$$

The solution and the boundary conditions of the previous development will be exactly same. This approach will certainly reduce the error in approximated generation. Although the effect of individual wavelength can be now studied, this solution will take much time at an added benefit of accuracy.

3.9. Extension of the Model to non-Silicon Material

In this section, the analytical models for different materials, other than Si, will be investigated. So far, we have seen that the model developed in the previous section is versatile. The same model can be extended easily for GaAs, Ge, InP and $Al_{0.3}Ga_{0.7}As$. These non-Si materials will have similar solution, but some modifications are needed for these materials. The first change is in the generation rate G. The coefficients (a_i and b_i)

for approximated generation rate have been already reported for the abovementioned materials in our previous publication [59] and repeated below.

Table 3.2. Coefficients a_i ($\times 10^{20} s^{-1} cm^{-3}$) and b_i ($\times 10^{4} cm^{-1}$) For Different Solar Cells [59]

Coeff. a_i, b_i	**Si**	**Si**	**GaAs**	**$Al_{0.3}Ga_{0.7}As$**	**Ge**	**InP**
	AM1.5D	**AM1.5G**				
a_1	28.63	50.63	120	60.63	500.63	110.63
a_2	6.60	10.00	65	30	90	100
a_3	4.20	3.90	3.9	2.5	7	2
a_4	0.511	0.45	0	0.00201	0.25	0.250
a_5	0.0211	0.0201	0	0	0.0200	0.0071
b_1	70.44	65.44	55.44	65.44	55.44	30.44
b_2	3.72	3.72	4.72	3.72	5.72	5.72
b_3	0.35	0.35	0.65	0.9620	0.70	0.935
b_4	0.0720	0.0620	0	0.9161	0.1	0.1720
b_5	0.0055	0.0061	0	0	0.0061	0.0061

Hence the carrier generation rates in other semiconductors are easy to obtain by modifying a_i and b_i. The other properties inherent to the material are the lifetime and mobility. The variation of these parameters with doping is available in literature. Hence using simple curve fitting tool, it is possible to extract power-law dependence empirical relationship of lifetime and mobility. This will produce new coefficients K, k, M, m for that specific material. Approximating the lifetime variation by one power-law curve may produce significant error; hence carefully dividing the doping range into several sub-ranges and using good-matched power-law relationship within those sub-ranges will give more accurate result. Actually this divided approach is used for Silicon, where K and k have two different values depending on doping range [8, 59].

If the solution with actual generation rate is desired, then changing the absorption coefficients by equation (3.73)–(3.74) will be just enough.

3.10. Extension of the model to Other spectrums

Extending the compact solution to other spectrum is also possible. Since different spectrum means different a_i and b_i, same model can be used to predict device operation of solar array under terrestrial spectrum (AM1.5), as well as solar cells on satellite under space spectrum (AM0).

As mentioned before, if actual generation rate is used in the analysis, then incident photon-flux $N(\lambda)$ of equation (3.73) has to be modified. This will accommodate any change in spectral intensity vs. wavelength for new spectrum.

3.11. Extension of the model to Gaussian Profile

The doping profile that is used in this compact modelling is exponential in nature. Another most common doping profile is Gaussian profile; hence the solution will be extended in this section to accommodate Gaussian profile variation.

If the doping profile follows a Gaussian variation, the previously developed solution will certainly not be compatible for this case. Including a Gaussian profile like $N = N_0 \exp[-(x-x_m)^2/\sigma^2]$ in equation (3.9) results in a differential equation that becomes impossible to solve without introducing any simplifying approximations.

To address this issue of Gaussian doping in analytical solution, exponential approximation technique can be used here. It has been reported [67] that approximating the Gaussian doping by an exponential profile causes insignificant error, if the integrated doping concentration is kept same for both cases. Applying this idea to the current analysis, the same exact solution can be used to Gaussian or any other profile, without increasing the mathematical complexity or loss of physical understanding. According this technique, Gaussian doping profile can be well approximated by either one exponential doping term, or by a combination of constant doping and exponential doping. Fig. 3.6 shows the comparison of their approximations for two Gaussian profiles [67].

If Gaussian doping can be replaced by piecewise exponential doping, then the compact model developed in section 3.1–3.10 will be applicable for Gaussian profile too.

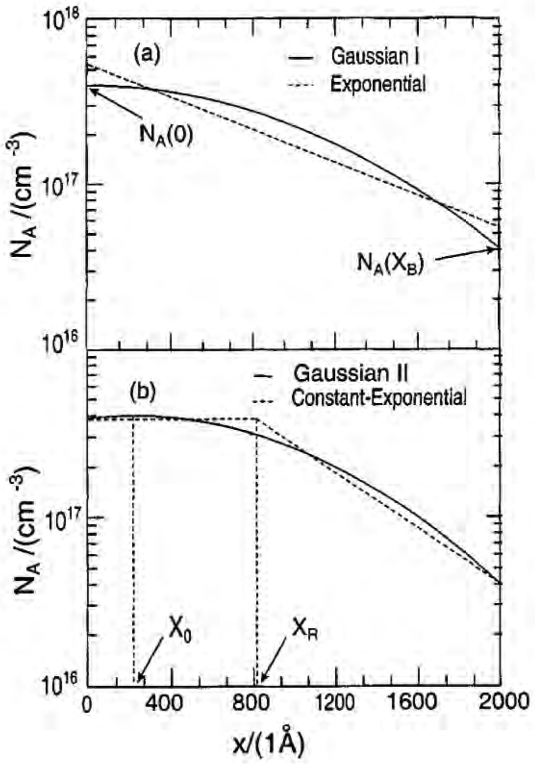

Fig. 3.7. Gaussian doping profile I (solid line) and exponential approximation (dashed line). (b) Gaussian profile II (solid line) and the constant-exponential approximation (dashed line) [67]

3.12. Summary

The aim of this chapter is to develop the analytical model for specific doping profile using advanced mathematical functions. The earlier sections have successfully discussed the development of such compact model by using the approximation in carrier generation rate. The solution is obtained in a closed-form expression of position, surface states, biasing and spectrum, all in one model.

The mathematics used for the development is robust enough to employ the same technique to exponentially increasing doping profile. Complete expression for the current density is also reported for minority carrier (both electron and hole) density.

To increase the applicability of this model for multi-layer solar cell, compact solution for two-layer emitter (and base) is also derived. The analysis further attempts to include the effects from individual wavelength. This time the derivation is done by including the actual generation from absorption and spectrum profile. As a result, the modified solution presents an elegant way to address the variation in spectral response.

The model has been improved to predict the behaviour of other material (including GaAs, AlGaAs, Ge and InP) and other spectrums (AM1.5D, AM1.5G, AM0). At the end, another technique is employed so that the solution can calculate the carrier concentration for other non-uniform doping variation (Gaussian profile).

In summary, a compact mathematical model has been developed and then upgraded to such substantial span that same analytical model can describe the effect of biasing, dark response, light response, solar spectral variation, change in photovoltaic material, mobility and lifetime variation, surface recombination, positional dependence, addition of layer and complex doping variation, but with an added complexity of Bessel and Hypergeometric function.

CHAPTER 4

NUMERICAL MODELING OF SOLAR CELL

4.1. Introduction

The significance of modeling electronic and photonic devices in TCAD simulator are increasing day by day because they make a drastic reduction in testing time and costs involved in fabricating and experimenting semiconductor devices. The focus of this thesis is not to offer the details on numerical simulation techniques for photovoltaic devices; rather this work will use the numerical tools as an effective way to verify the developed analytical solution. Hence a short and only relevant discussion will be presented in this chapter for understanding the results presented in later chapters.

SILVACO (Silicon Valley Company) is one of the most reliable tools for semiconductor devices [14, 20, 21, 68, 69]. It offers technology computer aided design (TCAD) software that simulates the behavior of semiconductor materials efficiently [70]. SILVACO's Atlas will be used in this thesis to simulate the solar cell and compare the results. Along with that, the proposed solution includes several mathematical functions. To clearly understand the physics and the mathematical integrity of the analytical expression, Equation-based-modeling in COMSOL Multiphysics [71] will be employed.

4.2. Silvaco/Atlas Device Simulator

ATLAS is a physically-based device simulator which solves the electrical characteristics at each points of the devices for the provided biasing condition [47]. The device is mapped into a 2D or 3D grid and a set of fundamental equations (derived from Maxwell's laws), which link together electrostatic potential and carriers densities, are solved at each mesh points (node points). Actually the device operation is governed by and described in a set of two coupled, partial differential equations:

- The Poisson equation
- The equation of continuity

ATLAS provides a comprehensive set of advanced models, as mentioned in the table below [47]. The physics that will be used here is highlighted in the table 4.1.

Table 4.1 Important Physical models and numerical methods used in ATLAS

Physical models	**Advanced Numerical Methods**
❖ *DC*, AC small-signal, and full time-dependency. ❖ *Drift-diffusion transport* models ❖ Energy balance and Hydrodynamic transport models. ❖ Lattice heating and heat sinks. ❖ Graded and abrupt hetero-junctions. ❖ Optoelectronic interactions with general ray tracing. ❖ Amorphous and polycrystalline materials. ❖ General circuit environments. ❖ Stimulated emission and radiation. ❖ *Fermi-Dirac and Boltzmann statistics.* ❖ *Advanced mobility models.* ❖ *Heavy doping effects.* ❖ Full acceptor and donor trap dynamics. ❖ *Ohmic, Schottky, and insulating contacts.* ❖ *SRH, radiative, Auger, and surface recombination.* ❖ Impact ionization (local and non-local). ❖ Floating gates. ❖ Band-to-band and Fowler-Nordheim tunneling. ❖ Hot carrier injection. ❖ Quantum transport models. ❖ Thermionic emission currents.	➢ Accurate and robust techniques of calculation in discrete level. ➢ Gummel, Newton, and block-Newton nonlinear iteration strategies. ➢ Efficient solvers, both direct and iterative way for linear problems. ➢ Powerful initial guess strategies. ➢ Small-signal calculation techniques that converge at all frequencies. ➢ Stable and accurate time integration.

4.2.1. Order of Commands

For simulating any semiconductor device, a list of commands has to be delivered to ATLAS. These statements have to follow a certain order so that ATLAS can generate the device after execution. The following five groups of statements that must occur in the correct order (see Figure 4.1).

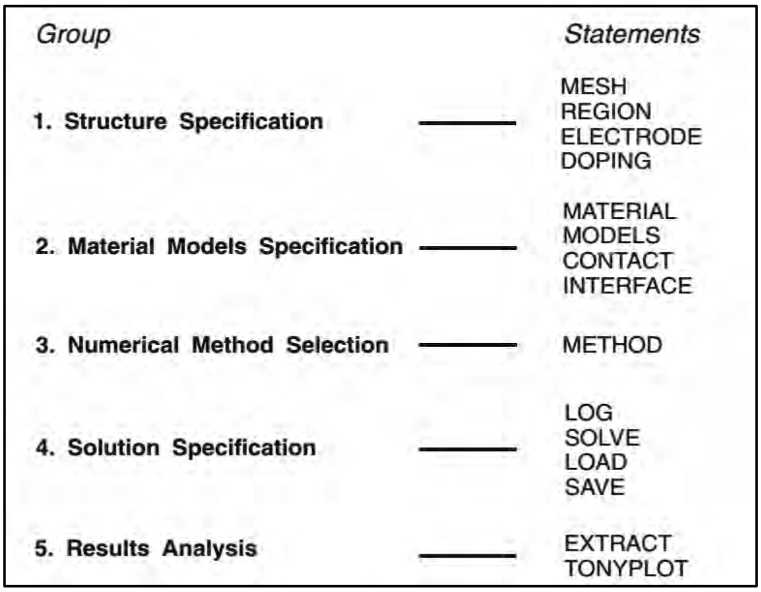

Group	Statements
1. Structure Specification	MESH REGION ELECTRODE DOPING
2. Material Models Specification	MATERIAL MODELS CONTACT INTERFACE
3. Numerical Method Selection	METHOD
4. Solution Specification	LOG SOLVE LOAD SAVE
5. Results Analysis	EXTRACT TONYPLOT

Fig 4.1. ATLAS Command Groups [68]

General format for statements and parameters in ATLAS follows a common syntax rule:

```
<STATEMENT> <PARAMETER>=<VALUE>
```

For example:

```
DOPING UNIFORM CONCENTRATION=1E16 N.TYPE REGION=1
```

The statement is indicating doping profile. The parameters of this command are: uniform, n.type, concentration and region.

The numerical solar cell developed here will be addressed in subsequent sections along with the explanation. The complete code is presented in the Appendix.

4.2.2. Structure and Model Specification

A device structure is specified when the meshing, region, electrodes and doping are explicitly defined for simulation. Afterwards, the created device can be simulated by incorporating the desired physical models and numerical methods. The steps only those necessary for the development and readability of this thesis will be discussed here.

4.2.2.1. Mesh

The mesh is a grid of horizontal and vertical lines over the dimensions of the device. Like finite element simulation, this gridline area is used to define data points and solution points. The general format of defining the mesh is given below:

```
mesh width=<Value>

x.mesh   location=<Value>  spacing=<Value>

y.mesh   location=<Value>  spacing=<Value>
```

The *x.mesh* and *y.mesh* parameters are defined to specify the area of simulation. *mesh width* sets total number of 2D xy-plane solar cell slices along the un-simulated third dimension. The 2D meshing used for modeling solar cell in this work is shown in fig. 4.2 below.

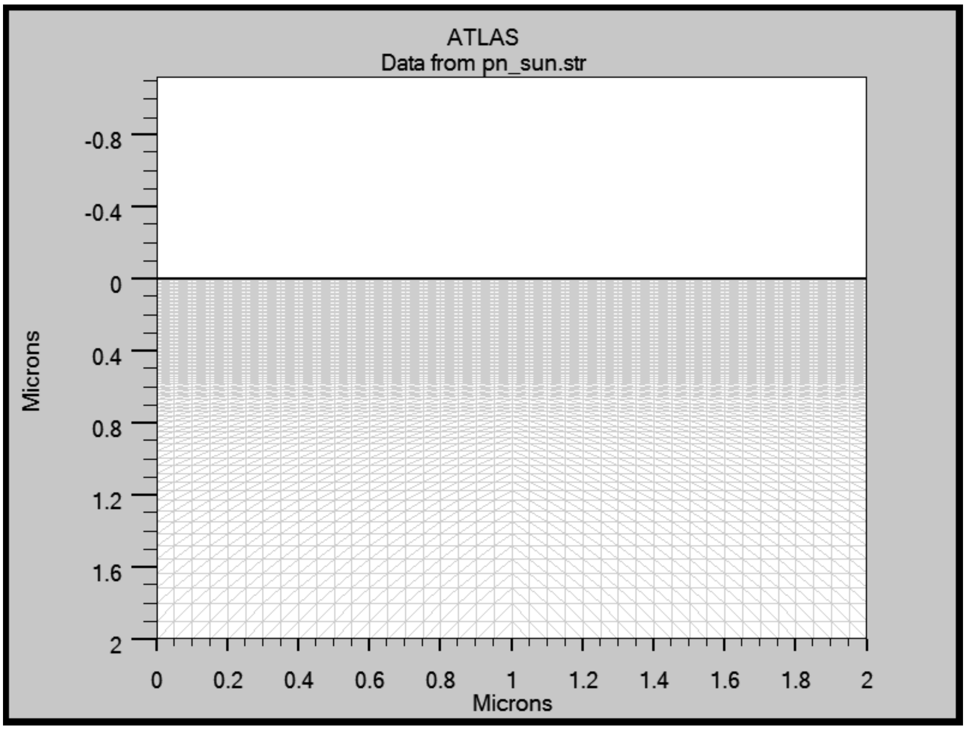

Fig 4.2. 2D Meshing for a 2μm thick solar cell

Since the emitter region (0.5μm) is of primary concern for its small dimension, the solution nodes (or alternatively the mesh density) are finer upto 0.5μm thickness. Moreover, the junction region generally has sharp changes in electric field and doping, hence denser mesh is necessary near the E-B depletion edge (fig. 4.2).

4.2.2.2. Region

Regions have to be defined along the mesh lines. The general syntax of this command is:

```
region number=<value>  material=<name of the material> /
x.min=<value> x.max=<value> y.min=<value> y.max=<value>
```

ATLAS allows the user to define up to 1000 different regions [47]. For this work, only one Silicon region is necessary (fig. 4.3). Hence, the code is quite straightforward–

```
region num=1 material=Silicon y.min=0.00 y.max=2
```

4.2.2.3. Electrode

Electrodes are the external electrical contacts. The electrode can be placed on desired location by specifying the position parameters: x.min, x.max, y.min, y.max. For p-n or p-n-n+ solar cell of this work, only anode and cathode has to be defined as electrodes. ATLAS will use default material as conductors [47], but Aluminum will be used in our simulation (fig. 4.3). The code used for defining electrodes is –

```
electrode num=1 name=anode x.min=0 x.max=0.5 y.max=0.0
material=Aluminum
electrode num=2 name=cathode y.min=2 material=Aluminum
```

4.2.2.4. Doping Profile

The silicon region needs to be exponentially doped for our purpose. Doping can either be n- or p-type with uniform profile, Gaussian profile, or complementary error function profile [13]. Doping statement has no parameter that will define exponential doping. To address the situation, analytically obtained doping profile from equation (3.8) is loaded as an ASCII file. This input data file contains the concentration (in cm^{-3}) vs. depth (in μm) information. The following code will generate the n-type exponential doping of fig. 4.4.

```
DOPING n.TYPE Y.MIN = 0 Y.MAX = 0.5 ASCII INFILE = Exponential_doping
```

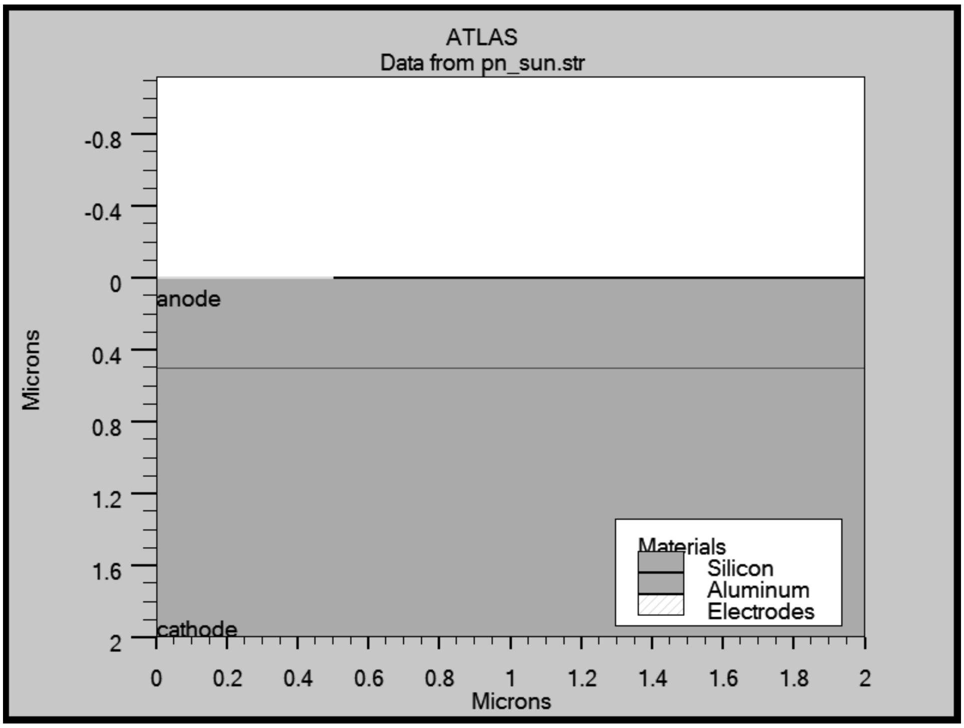

Fig 4.3. Regions and electrode of a simple solar cell

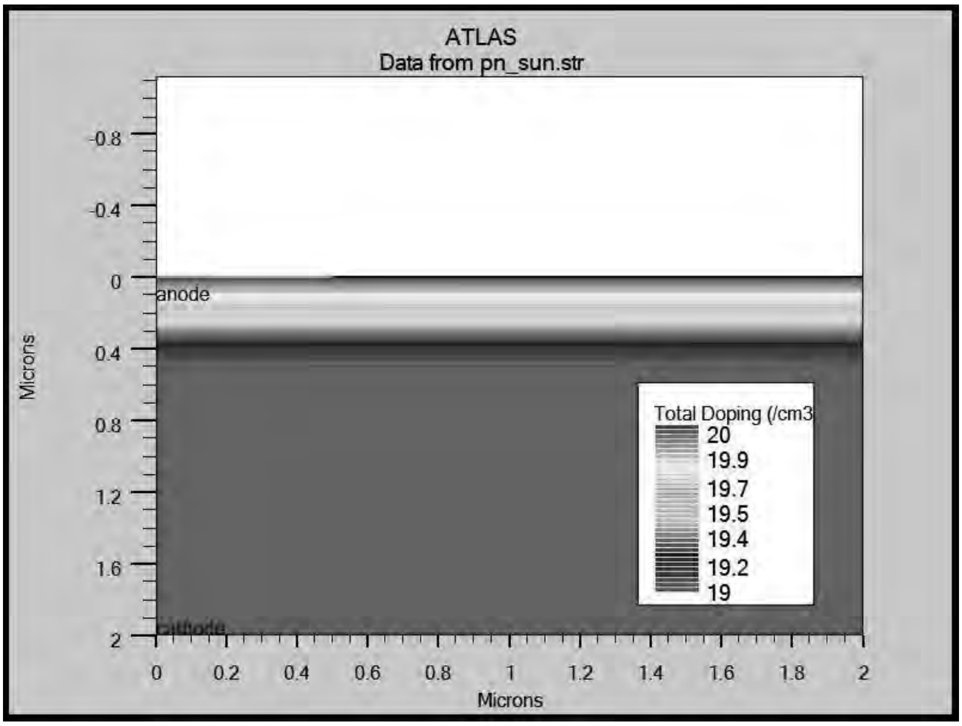

Fig 4.4. 2D variation of total doping. The n-type emitter is exponentially doped and the base region is uniformly doped

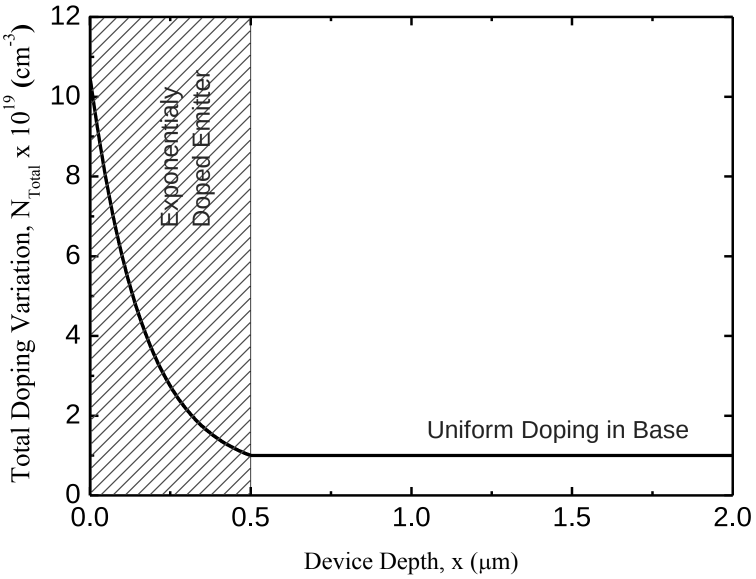

Fig 4.5. Extracted 1D doping variation (total) along the depth of the device

4.2.2.5. Material Model Specification

Once the simulation geometry is designed, the next step is to set the default material properties or override them if necessary. To define the properties for the materials used in the modeling of the device, the command *material* statement is used.

```
material material=Aluminum sopra=Al.nk
```

Here, the complex refractive index as a function of temperature and composition for Aluminum is incorporated in the simulation by the SOPRA parameter. Refractive indices play a major role in defining the amount of light transmitted, reflected and refracted. This property can be defined with the help of *SOPRA* database [72]; Properties that is limited to a certain material like optical properties, low field mobility, recombination lifetimes, conduction band density of states at 300K etc. can be assigned using the material command. Moreover, the built-in materials library in ATLAS is very rich. Many common materials are member of this library [47] and their respective useful properties are included in their library file. Other than that, ATLAS has the ability to use new materials from outside the library by defining them manually [21].

4.2.2.6. Specifying Surface State

The analytical model developed in previous chapter uses surface recombination velocity to calculate the carrier concentration at the surface. To ensure that the physically-based simulation in ATLAS is comparable with the analytical solution, the surface recombination velocity will be included by the contact command.

```
contact name=anode SURF.REC VSURFP=5e2
```

The default property of top surface (anode contact) is overridden by the SURF.REC parameter and the minority carrier (hole) recombination velocity is specified by VSURFP. Similar coding goes for the cathode contact.

4.2.2.7. Models

There are many models in ATLAS to improve the accuracy of the structure and to get more realistic values. BGN, SRH, CONSRH, AUGER, CONMOB and OPTR are the dominant models that will be used here for photovoltaic simulation.

A. BGN defines band-gap-narrowing. Since the doping variation that will be used in analysis exceeds $10^{18}cm^{-3}$, the p-n product in silicon will become doping dependent [73]. As the doping level increases, a decrease in the band-gap is inevitable, where the conduction band is lowered by approximately the same amount as the valence band is raised [74].

B. SRH is for Shockley-Read-Hall recombination
This transition occurs in the presence of a trap (or defect) within the forbidden gap of the semiconductor.

C. CONMOB for concentration dependent mobility:
The local electric field, lattice temperature, doping variation, surface and material imperfection inside the device will affect the mobility of the carriers. Since the non-uniformly doped DF solar cell has electric field across the quasi-neutral region and inside the junction, their effects have to be included in the modeling process.

Atlas offers 4 mobility models –

i. Low-field behavior
ii. High field behavior
iii. Bulk semiconductor behavior
iv. Inversion layer

At low field, the carrier mobility is in quasi-equilibrium and depends on phonon and impurity scattering. To include the low field mobility in the simulation, CONMOB model is used here, which uses a look-up table for experimental mobility values at 300K. The mobility vs. doping dependence it follows is shown in the fig. 4.15 below.

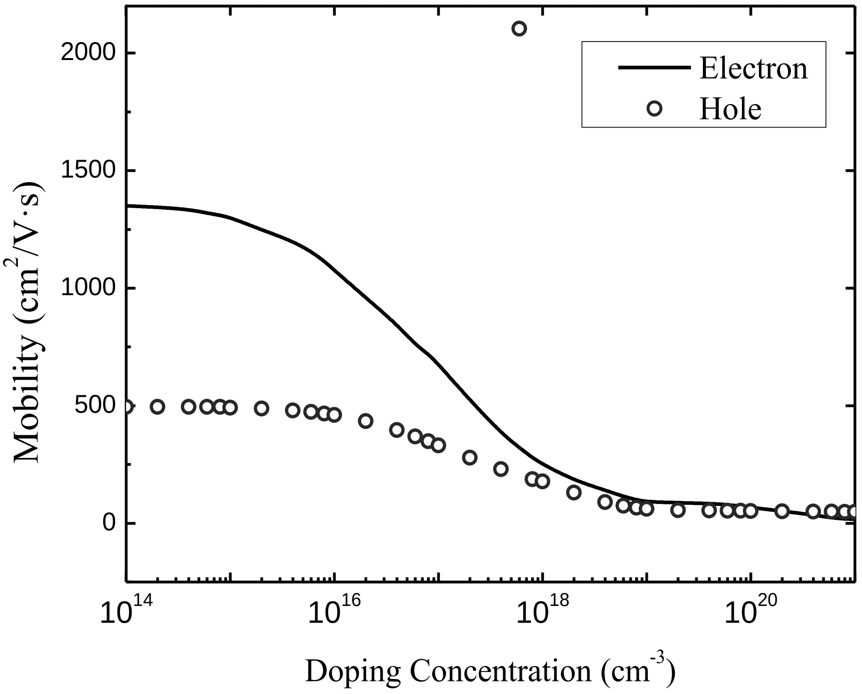

Fig 4.6. The empirical data of mobility dependence on doping used in CONMOB model of ATLAS.

There are other mobility models (see table 4.2) that can be employed in the quest of verifying the analytical model.

Table 4.2. Different mobility models in ATLAS [47]

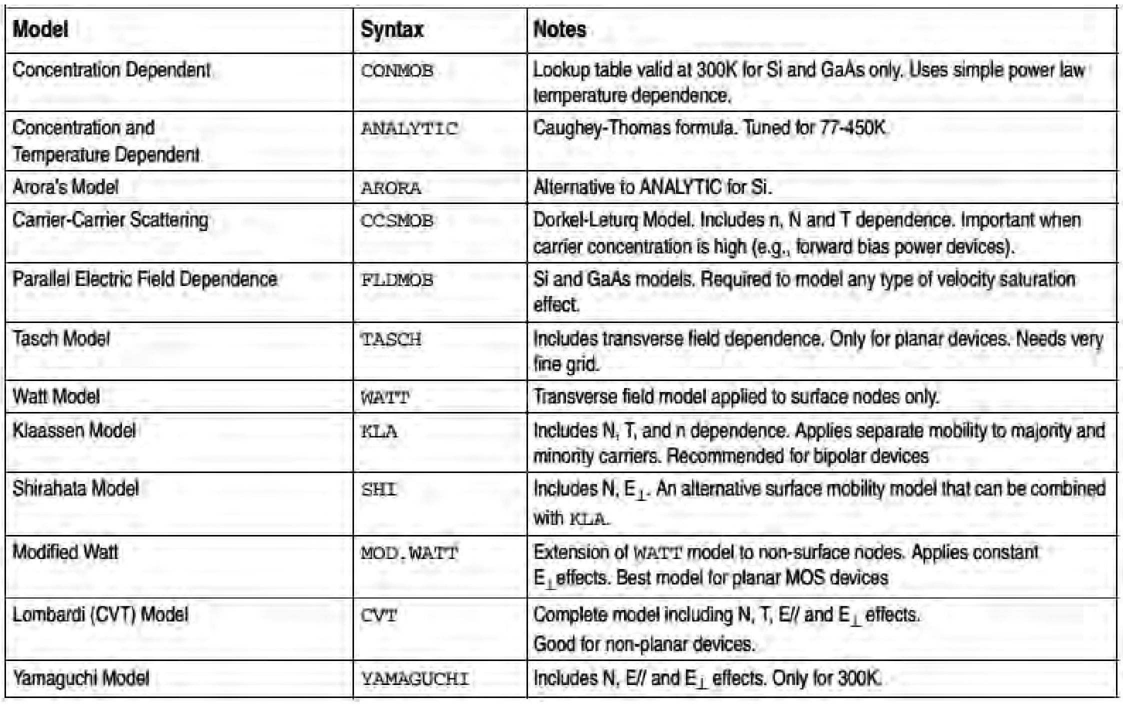

Model	Syntax	Notes
Concentration Dependent	CONMOB	Lookup table valid at 300K for Si and GaAs only. Uses simple power law temperature dependence.
Concentration and Temperature Dependent	ANALYTIC	Caughey-Thomas formula. Tuned for 77-450K.
Arora's Model	ARORA	Alternative to ANALYTIC for Si.
Carrier-Carrier Scattering	CCSMOB	Dorkel-Leturq Model. Includes n, N and T dependence. Important when carrier concentration is high (e.g., forward bias power devices).
Parallel Electric Field Dependence	FLDMOB	Si and GaAs models. Required to model any type of velocity saturation effect.
Tasch Model	TASCH	Includes transverse field dependence. Only for planar devices. Needs very fine grid.
Watt Model	WATT	Transverse field model applied to surface nodes only.
Klaassen Model	KLA	Includes N, T, and n dependence. Applies separate mobility to majority and minority carriers. Recommended for bipolar devices
Shirahata Model	SHI	Includes N, $E_\perp$. An alternative surface mobility model that can be combined with KLA.
Modified Watt	MOD.WATT	Extension of WATT model to non-surface nodes. Applies constant $E_\perp$ effects. Best model for planar MOS devices
Lombardi (CVT) Model	CVT	Complete model including N, T, E// and $E_\perp$ effects. Good for non-planar devices.
Yamaguchi Model	YAMAGUCHI	Includes N, E// and $E_\perp$ effects. Only for 300K.

4.2.3. Optoelectronic Simulator: LUMINOUS

In the numerical study of solar cell, simulating light propagation and absorption must be integrated. LUMINOUS is the default tool that will simulate the electrical responses to optical signals, by converting optical intensity profile into photogeneration rate.

There are several physical models for propagation of light inside the device,

- Ray tracing
- The transfer matrix method
- The beam propagation method
- Finite difference time domain method
- User-Defined Photogeneration

For our purpose, 2D ray tracing method will be used to simulate the solar spectrum. This method uses the real component of the refractive index to calculate the optical intensity and the imaginary component in the absorption model to calculate the carrier concentration.

By using the BEAM command, the optical source can be modeled inside ATLAS. The general syntax is `BEAM <parameters>`.

The parameters cover a broad spectrum including terrestrial spectrum AM1.5 and space spectrum AM0. The code to include the AM1.5G spectrum is below:

```
beam num=1 AM1.5 x.origin=1 y.origin=-1 angle=90.0 waval.start=0.1
waval.end=1.2 waval.num=500 reflect=4 back.refl
```

The spectrum imported in this command is AM1.5, which is actually a table of wavelength vs. intensity from NREL [66]. X.ORIGIN and Y.ORIGIN are shown in figure 4.7, with an ANGLE. Since silicon cell mostly absorbs light up to 1.1μm, discretizing the spectrum between 0.1μm to 1.1μm is enough for simulating sunlight. Hence WAVEL.START sets the starting wavelength of the AM1.5 spectrum, WAVEL.END denotes the end of the spectrum. WAVEL.NUM sets the number of steps taken in this spectrum range. REFLECT parameter takes the specified number of reflections at the front interfaces and BACK.REFL considers if there is any back reflection from the device.

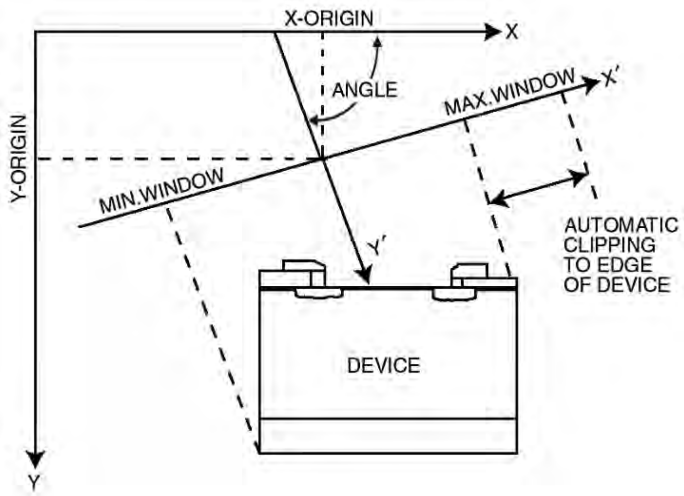

Fig 4.7. Schematic describing the 2D ray tracing by BEAM command parameters [47]

ATLAS allows user-defined photo-generation techniques. The mentionable ones are –

- Exponential Photogeneration
- Tabular Photogeneration

The exponential photogeneration is a function of location. It is noteworthy because similar photogeneration is used in our analytical model (see equation (3.3) of approximated Generation rate). The equation ATLAS uses [47] is mentioned here –

$$G(l, r) = (\mathtt{CONSTANT} + \mathtt{LINEAR} \cdot l + \mathtt{FACTOR}\mathit{exp}(-\mathtt{EXPONENT} \cdot l))\mathit{exp}\left(-\left(\frac{r^2}{\mathtt{RADIAL}^2}\right)\right)$$

The above generation rate can be expressed as a sum of exponential terms by carefully setting the values of CONSTANT, LINEAR, FACTOR, EXPONENT and RADIAL. The relationship is an important indicator that the approximation used in the derivation of our analytical model is already well-used in standard device simulation tools.

The tabular photogeneration rate takes into account an ASCII file that contains the photogeneration rates over the x-y grid points, in units of per second per cubic cm. This command is useful to check how well our model can predict carrier concentration when ATLAS simulation uses same tabulated G(x) as our analytical approach uses.

The photogeneration that will be used to compare with analytical generation rate is shown in fig 4.8.

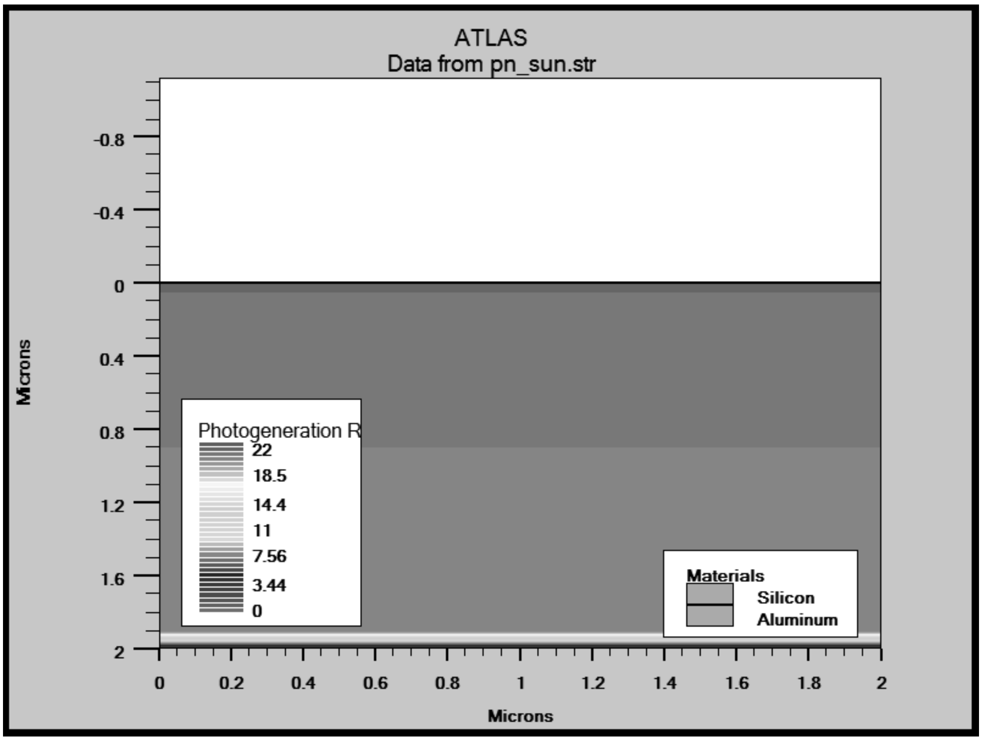

Fig 4.8. Photogeneration rate G(x) for AM1.5, obtained from ATLAS 2D ray tracing method

4.2.4. Numerical Method Selection

Numerical methods are used to calculate solutions to semiconductor device problems. There are three types of solution techniques:

- Decoupled (GUMMEL)
- Fully coupled (NEWTON)
- BLOCK

The GUMMEL method solves for each unknowns by keeping all other unknowns constant. The process is repeated until there is a stable solution. The NEWTON method solves all unknowns simultaneously. The BLOCK method solves some equations with the GUMMEL method and some with the NEWTON method.

4.2.5. Solution Specifications

Once the structure, physical model, optical techniques and numerical methods are set correctly, it is quite easy to extract the solution at each node points. For example, to get the solved structure, the following code is enough.

```
solve b1=1.0

structure outf = pn_sun.str

tonyplot pn_sun.str
```

This will solves the structure with the BEAM over the device. The designer can also solve a sweeping bias using the following commands:

```
solve vcathode=0

solve vanode=-5 vfinal=5 vstep=0.1 name=anode
```

This will solve the circuit for a basing sweep of anode voltage from -5 to 5 with 0.1 voltage steps. The results can be saved to a log file (see below) for extracting the desired solved quantities.

```
log outfile=Solar_cell_Under_light.log
```

4.2.6. Results Analysis

Silvaco offers a *post-processing* viewing program named TONYPLOT. The structure and log files created from ATLAS can be visualized here. The structure files (.STR) display mesh density, doping concentrations, current densities, and many more parameters. The LOG files present the results of ATLAS's electrical and optical analysis.

The simulated hole and electron concentration under AM1.5 is presented in the fig. 4.9. Since this is a p-n junction, the majority carrier (hole) concentration at the emitter is almost uniform, but the minority carrier concentration varies significantly. Same observation applies for the carrier concentration in base region. These results will be used in the results section to validate the analytical model.

A 3D model of Silicon solar cell is also developed which can be used to investigate the effect from 3rd dimension. The complete code is given in the appendix.

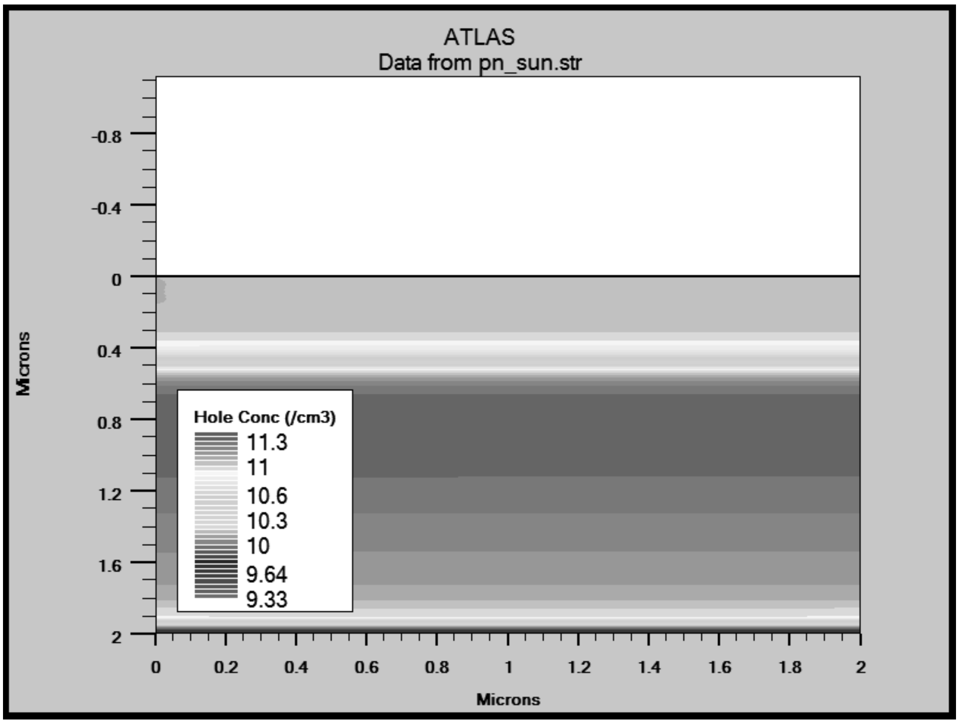

Fig 4.9. Hole concentration along the depth. simulation results extracted from ATLAS

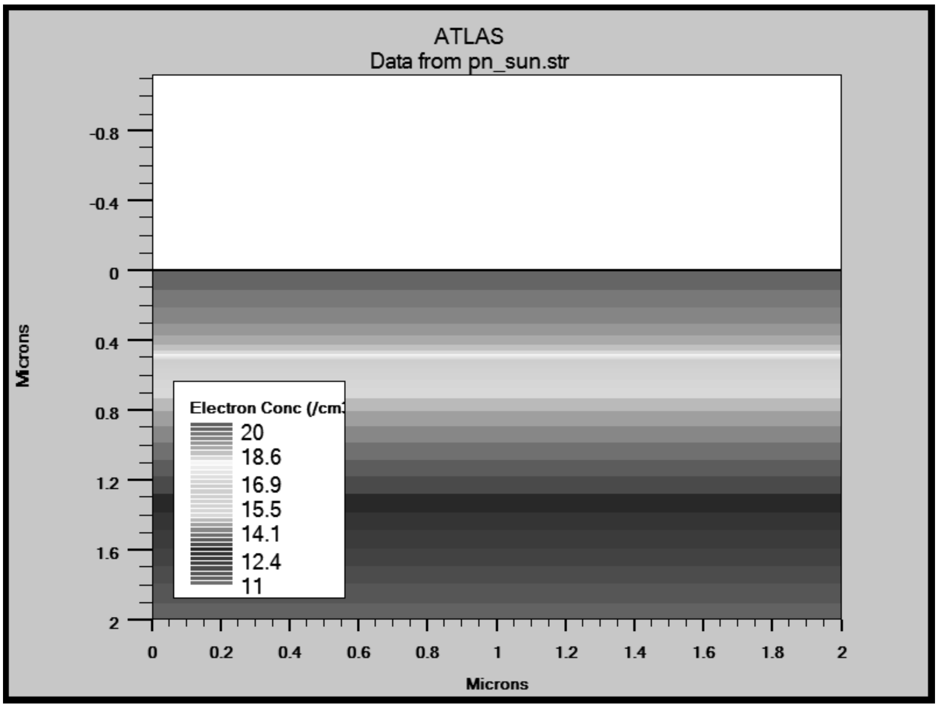

Fig 4.10. Electron concentration along the depth. Simulated results extracted from ATLAS.

4.3. COMSOL Multiphysics

COMSOL Multiphysics is an interactive environment for modeling engineering problems. Using the built-in physics interfaces and the advanced support for material properties, powerful models can be developed that includes relevant physics by defining the underlying partial differential equations (PDEs). COMSOL Multiphysics uses the finite element method (FEM) to create the model [75]. The software can also use adaptive meshing and error control by the help from a variety of numerical solvers.

COMSOL Multiphysics creates sequences to record the steps of creating device geometry, the meshing information, numerical studies and the results. This offers the ability to study the model by varying the necessary parameters.

For this thesis, the COMSOL Multiphysics will be used a second verification tool. The equation based modeling technique will be employed to address the mathematical soundness of the analytical model.

There are several tools that can be used to model the underlying equations of solar cell. They are [75] –

- The Mathematics Interfaces
- PDE Interfaces
- Weak Form Modeling
- Using Weak Constraints
- Solving ODEs and DAEs
- The Wall Distance Interface
- Theory for the Wall Distance Interface

For our purpose, the PDE interface will be used; specifically the *Coefficient form PDE interface* will be our main focus. This interface covers several well-known PDEs that can help in solving the differential equations of chapter 3.

The Scalar Coefficient Form Equation

The dependent variable u(z) is an unknown function on the computational domain (Ω). COMSOL Multiphysics determines it by solving the PDE problem that is specified. In Coefficient form, the PDE equation used by COMSOL is –

$$e_a \frac{\partial^2 u}{\partial t^2} + d_a \frac{\partial u}{\partial t} + \nabla \bullet \left(-c\nabla u - \alpha u + \gamma \right) + \beta \bullet \nabla u + \alpha u = f \qquad (4.1)$$

The COMSOL PDE formulations uses coefficient names that fall within the realm of continuum mechanics and mass transfer (see *General Names* in Table 4.2). This PDE interface will, by default, add the nodes: Zero Flux and Initial Values. These nodes will indicate the boundary conditions at the computational domain.

$$n \bullet \left(-c\nabla u - \alpha u + \gamma \right) + qu = g - h^T \mu \;; \qquad \text{at the domain boundary} \qquad (4.2)$$

$$\mu = r \;; \qquad \text{at the domain boundary} \qquad (4.3)$$

Equation (4.2) is a generalized Neumann boundary condition. This is also known as natural boundary conditions, since it does not occur explicitly in the weak form of PDE problem. Equation (4.3) is a Dirichlet boundary condition, which corresponds to a flux or source. This is known as essential boundary condition that specifies the value of the numerical flux at the boundary.

The Neumann condition specifies the value of the dependent variable at the boundary, while the Dirichlet boundary condition forces an arbitrary function of the dependent variables to equal zero on the boundary [75].

To include our differential equation in the finite element modeling, the coefficients c, α, β, γ, a, h, and the terms f, g, r have to be specified. Equation (3.10) and the boundary conditions are repeated here for easy access –

$$\frac{d^2p}{dx^2}+\alpha(m+f-1)\frac{dp}{dx}-\left(m(1-f)\alpha^2+\frac{N_{d0}{}^{m+k}e^{-\alpha(m+k)x}}{KMV_T}\right)p=-\left(\frac{N_{d0}{}^{m}e^{-\alpha mx}}{MV_T}\right)\sum_{i=1}^{5}a_ie^{-b_ix}$$

$$p\left(x_j\right)=\frac{n_i^2}{N(x_j)}\exp\left(\frac{V}{V_T}\right)$$

$$\left[\mu(x)Ep(x)-D_p\left(x\right)\frac{dp(x)}{dx}\right]_{x=0}=S\,p\left(0\right)$$

The above equation is non-linear, because the coefficients depend on p(x) and its derivatives. Comparing the above equation and the boundary conditions with equation (4.1)-(4.3) above, the coefficient values are obtained for modeling. These are listed in table 4.3.

Table 4.3. Values of coefficients and Terms used in COMSOL modelling

Coefficient and Terms	**General Name**	**Value**
u(x)	Dependent Variable	Hole concentration, p(x)
c	Diffusion Coefficient	-1
α	Conservative Flux Convection Coefficient	0
β	Convection Coefficient	$-\alpha\ (1-f-m)$
γ	Conservative Flux Source	0
a	Absorption Coefficient	$-\ N_{d0}{}^{m+k}/(KMV_T) \times \exp\ [-\alpha\ (m+k)\ x]$ $-\ m(1-f)\ \alpha^2$
f	Source Term	$-N_{d0}{}^{m} \exp(-\alpha mx)/(MV_T) \times \Sigma\ a_i \exp(-b_ix)$
g	Boundary Flux/Source	0
r	Dirichlet Boundary Coefficient	$(ni^2/Nd\_W)\ \exp(V/V_T)$

$\mathbf{e_a}$	Mass Coefficient	0
$\mathbf{d_a}$	Damping Coefficient	0
q	Boundary Absorption / Impedance Term	$-S/(V_T M N_{d0}^{-m})+\alpha(1-f)$

All the symbols used in the table 3.2 are already introduced in chapter 3. The solution is obtained for very fine meshing. After the FEM modeling, the results from the COMSOL can be extracted for further analysis, as seen in fig. 4.11.

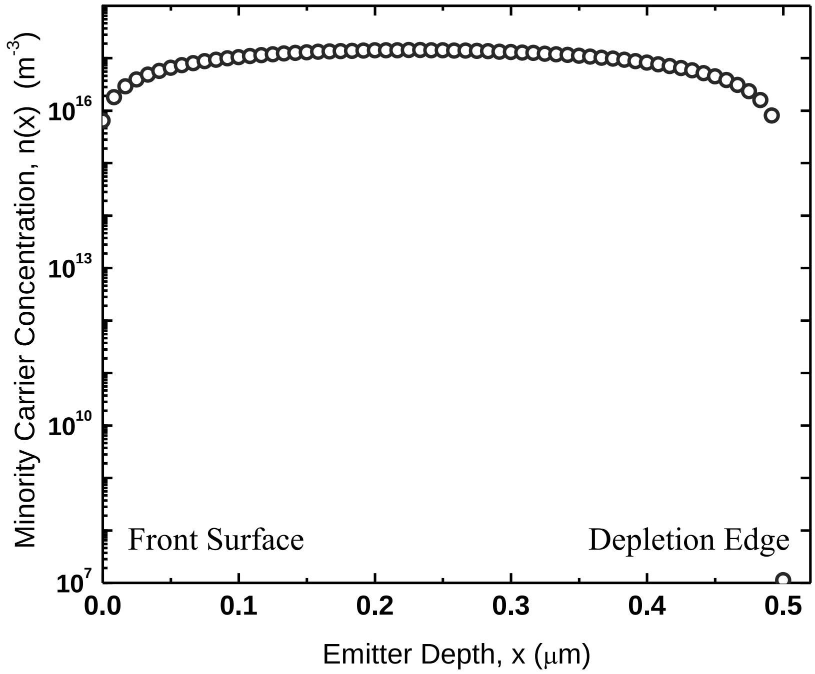

Fig 4.11. Minority carrier concentration, extracted from the COMSOL multi-physics model.

4.4. Conclusion

This chapter presents the details of developing numerical solar cell models. For this purpose, a physically-based TCAD simulator Silvaco/ATLAS is used. The electrical behavior of the cell is simulated by including the BGN, SRH, CONSRH and Auger models and light response is taken into account by using a beam of AM1.5 solar spectrum.

Besides, a physics-based simulator COMSOL is used to model the differential equation behind the photovoltaic operation. The equation-based modeling technique uses finite element method to discretize the calculation domain and provide the desired results.

The numerical models of solar cell developed in this chapter will be used to validate the previously derived analytical model.

Chapter 5

RESULTS AND DISCUSSIONS

5.1. Introduction

The main success of this work is that one single model includes the effect of solar illumination, doping profile, surface & bulk recombination, heavy doping effect and mobility & lifetime variation. Besides, this model can be extended to other materials (e.g. Ge, GaAs, GaP, CIGS etc.), other solar spectrum (AM1.5D, AM1, AM0 etc.) and other practical doping profiles (Gaussian profile, power-law profile). In this chapter, the applicability of this analytical work will be discussed by exploring the model more profoundly, for some common solar cell configurations. Along with the analysis, the results will be verified by Silvaco/ATLAS Device simulator and Numerical model of COMSOL Multiphysics, which have already been developed in Chapter 4.

5.2. Effect of Transport parameters on minority carrier concentration

Since the model reported here considers several position-dependent parameters, it is easier to evaluate each of their effects separately and simultaneously to get more insight in the physics.

5.2.1. Effect of BGN on Solution Parts

The hole concentration in an n-type emitter will be taken as an example. The analysis for electron will be similar & discussed later. The expression of p(x) in (3.19) has three constituting terms:

- The first two terms, namely $P_1(x)$ & $P_2(x)$ corresponds to dark condition, which is just normal p-n junction current under no generation i.e., $G = 0$.
- The third term is the contribution from illumination. This specific $P_3(x)$ is the major concern for photovoltaic action.

All three terms and their effects will now be studied meticulously. A thin emitter layer (0.5 μm) is considered for this purpose. This range of emitter thickness is quite common for practical solar cells. The doping profile is exponential in nature. Doping concentration is varied from 10^{20} cm^{-3} (at x = 0 μm, surface) to 6×10^{18} cm^{-3} (Emitter-Base junction is at $x = x_j = 0.5$ μm). The recombination at the front surface is characterized by surface recombination velocity (S_p). Moderate values of recombination velocity ($S = 5 \times 10^4$ cm/s) is considered at the top surface.

$P_1(x)$ and $P_2(x)$ are calculated (see fig. 5.1) without BGN ($f = 0$) and with BGN ($f = 0.75$). It is found that BGN has no effect on $P_1(x)$. On the other hand, $P_2(x)$ term depends greatly on the band gap narrowing effect. Previous works [36], that have neglected BGN, will certainly give significant error for $P_2(x)$ term. The contribution from illumination, namely $P_3(x)$, has no significant change for BGN. This can be explained easily since $P_3(x)$ depends on incident solar spectrum. This is also evident in fig. 5.2. The change of spectrum from AM1.5G to AM1 (keeping all other parameters same), has improved $P_3(x)$, although the change is not that much in value. The detailed analysis of effects from spectrum will be revisited later.

5.2.2. Effect of Variable Lifetime and Mobility on Analytical Solution

Instead of normalized solution parts, the complete solution for a practical emitter layer will be studied now. Two device configurations will be considered to ensure the versatility of the analytical model.

- A p^+-n junction, where *mobility and lifetime strongly depend on doping variation. The band gap narrowing will be ignored*. Generally for a emitter or base region of DF solar cell, when the doping variation does not exceed 5×10^{18} cm^{-3}, the mobility and lifetime show power-law dependence on doping. The band gap narrowing, on the other hand, can be neglected safely for this range of doping.
- A p-n junction *where mobility, lifetime & BGN depend on doping profile*. This situation will arise for that particular cell when the doping profile is higher (exceeds 5×10^{18} cm^{-3}).

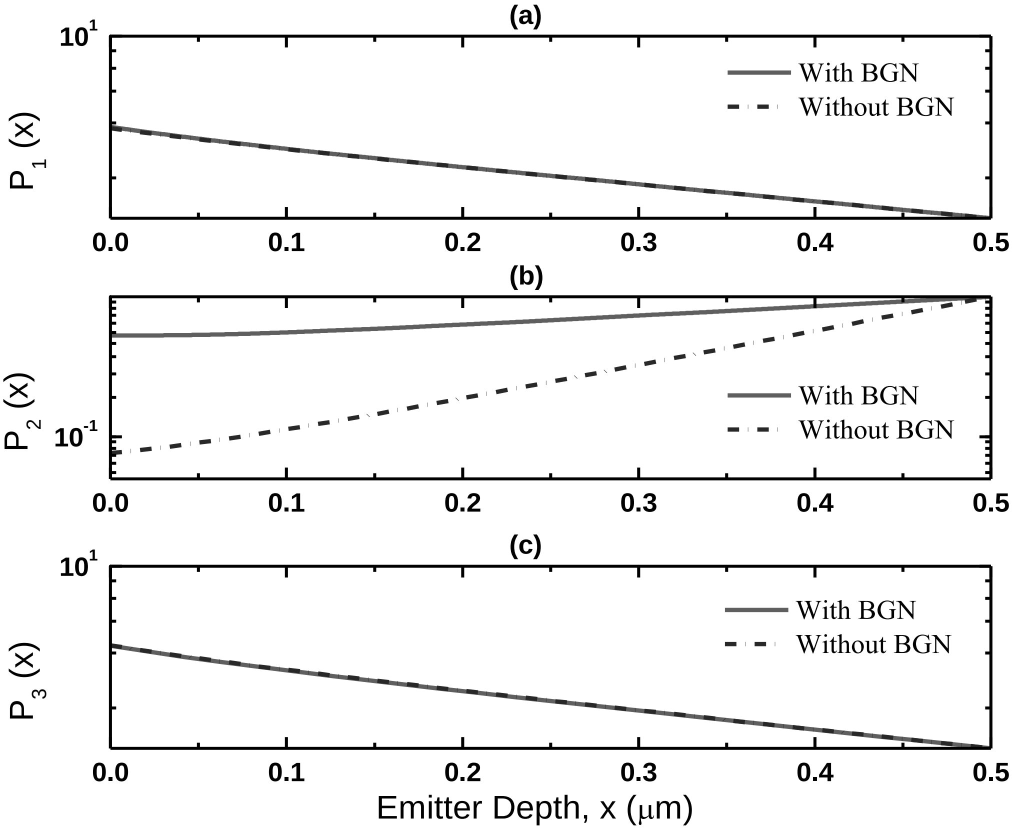

Fig 5.1. Effect of band gap narrowing on the solution of minority carrier concentration. The doping is varied exponentially from 10^{20} cm^{-3} to 6×10^{18} cm^{-3} (a) $P_1(x)$ normalized to $P_1(x_j)$, (b) $P_2(x)$, normalized to $P_2(x_j)$ and (c) $P_3(x)$, normalized to $P_3(x_j)$. Spectrum: AM1.5G.

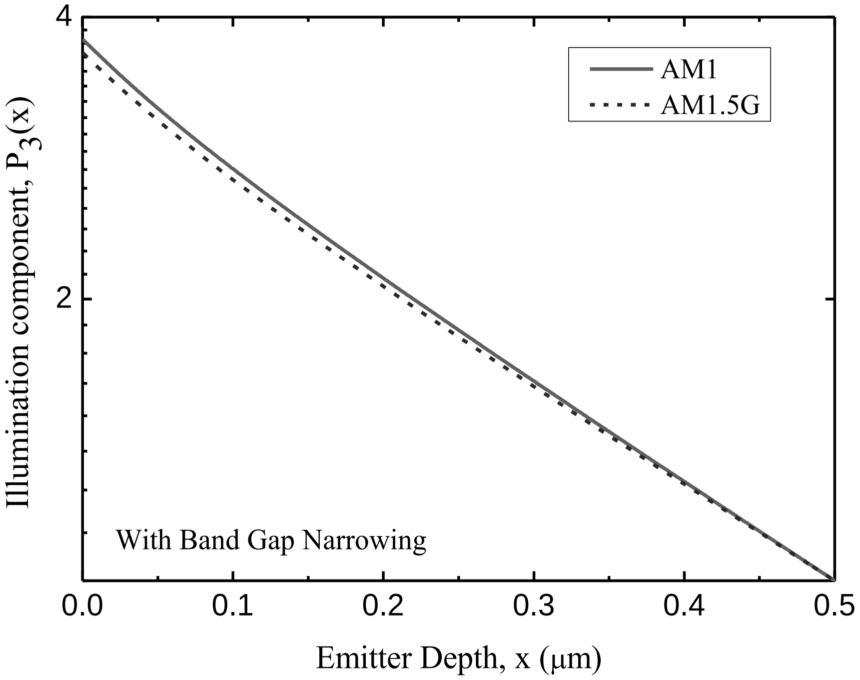

Fig 5.2. Effect of Solar spectrum (AM1 and AM1.5G) on illumination term $P_3(x)$

A p^+–n(x) DF Silicon Solar Cell:

The DF solar cell is assumed to have uniform doping at emitter region and exponential doping at Base region. Hence this serves as good example to demonstrate the impact of both doping profiles at the same time. For this uniform doping density in P-type emitter, mobility and lifetime will become constant along the device depth (m, M, k, K all are constant in equation (3.4)-(3.5)). As mentioned in chapter 3, the resulting model will become a special case of our solution. BGN in equation (3.10) is ignored for this case, i.e., $f = 0$. The excess minority carrier electron density is described by equation (5.1),

$$n\,(x) = C_1 \exp\left(\beta_u x\right) + C_2 \exp\left(-\beta_u x\right) - \left(\frac{N_{d0}{}^{m}}{MV_T}\right) \sum_{i=1}^{5} \left(\frac{a_i}{b_i{}^2 - \beta_u{}^2}\right) \exp(-b_i x) \quad (5.1)$$

β_u is already defined in chapter 3. M, N are constants to be determined from boundary conditions at top surface and depletion edge. The solution is depicted in fig. 5.3 for high front surface recombination velocity (5×10^6 cm/s). A comparison with numerical models, developed in COMSOL and ATLAS, is also presented in the same figure. Since the bang gap narrowing is neglected and the doping is constant throughout this region, the electric field inside the emitter is zero. As seen from the fig. 5.3, the analytical model slightly underestimates the electron concentration near the middle of the device. Also at the edge of the emitter-base depletion region, unlike numerical model, the concentration drops. This can be explained from the fact that ATLAS considers the minority carrier variation inside the depletion region, while the analytical solution uses (ni^2/N_D) in its boundary condition at E-B edge (see equation (3.46)). This slight mismatch seen in fig. 5.3 can also be attributed on the approximation of carrier generation rate (G) and the empirical relationships of mobility and lifetime. It is noteworthy that the COMSOL drift-diffusion-based FEM model for the same device perfectly matches with analytical solution. This proves that, from mathematical viewpoint, our analytical model is robust and the solution is correct for the included physics.

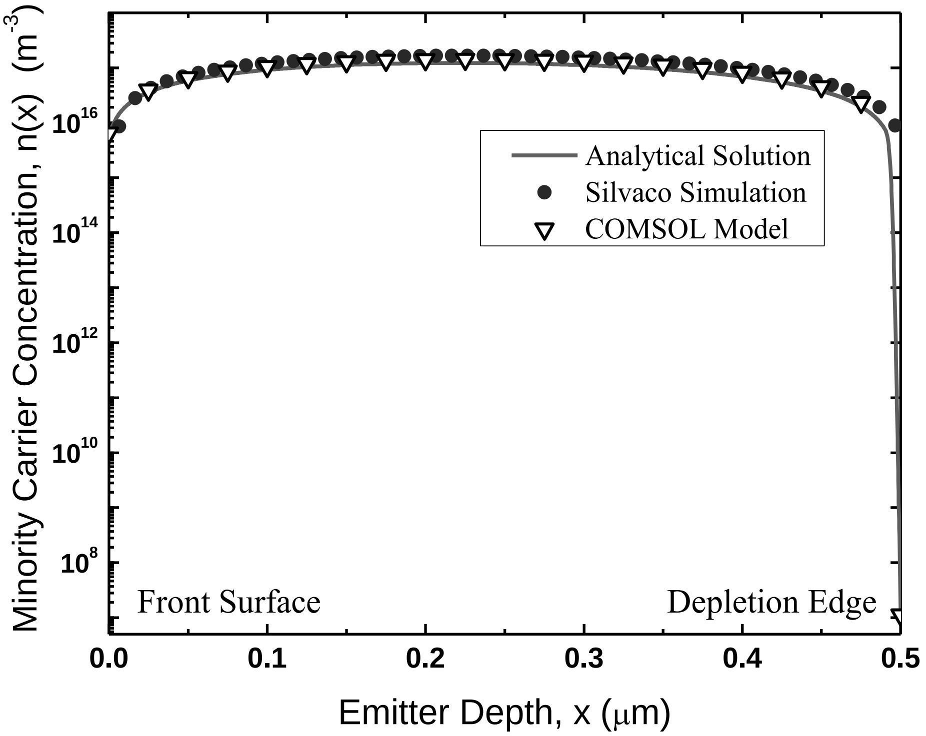

Fig 5.3. Minority carrier (electron) concentration for uniformly doped (2×10^{19} cm^{-3}) P-type Emitter. The front surface recombination velocity (S_P) is 5×10^{6} cm/s. The symbols represent numerical solution (COMSOL Model and ATLAS model) and the line represents our analytical model.

For base region, increasing exponential doping is considered. This corresponds to the modified model of section 3.4. There will be induced electric field in base due to non-uniform doping. This built-in electric field in base region is important for reducing the damage from nuclear particle radiation [36]. Since the induced field in base has practical application in improving radiation resistance, considering such a base in our analytical model will be an effective way to test practical situation.

The doping density is minimum ($N_{d\text{-}min} = 7 \times 10^{17}$ cm^{-3}) at $x = x_j + W$ (the edge of depletion region at the base side) and at the end of base ($x = H$), it is 4.5×10^{18} cm^{-3} (see the device configuration at fig. 3.1). Since the doping range is not that high, ignoring BGN is justified, although it can easily be included in calculation by setting f = 0.75. Besides, along with exponentially increasing doping profile, the lifetime and mobility gradually fall towards the back surface. The power-law dependence of lifetime and mobility on doping (hence, position) makes our analytical solution effective in analysing this type of base region. The electric field E, on the other hand, is constant because the impurity density has exponential variation and contribution from the band gap narrowing is excluded in E (see equation (3.6) for f = 0). The electric field is negative with respect to depth (x), as it should be, since the donor concentration is gradually increasing as x increases. Fig. 5.4 shows the positional variations of transport parameters which are included in the solution.

The boundary conditions for this base region are:

$$p\left(x_j+W\right)=\frac{n_i^2}{N(x_j+W)}\exp\left(\frac{V}{V_T}\right)$$

$$\left[\mu(x)Ep(x)-D_p\left(x\right)\frac{dp(x)}{dx}\right]_{x=H}=S_p\ p\left(H\right)$$

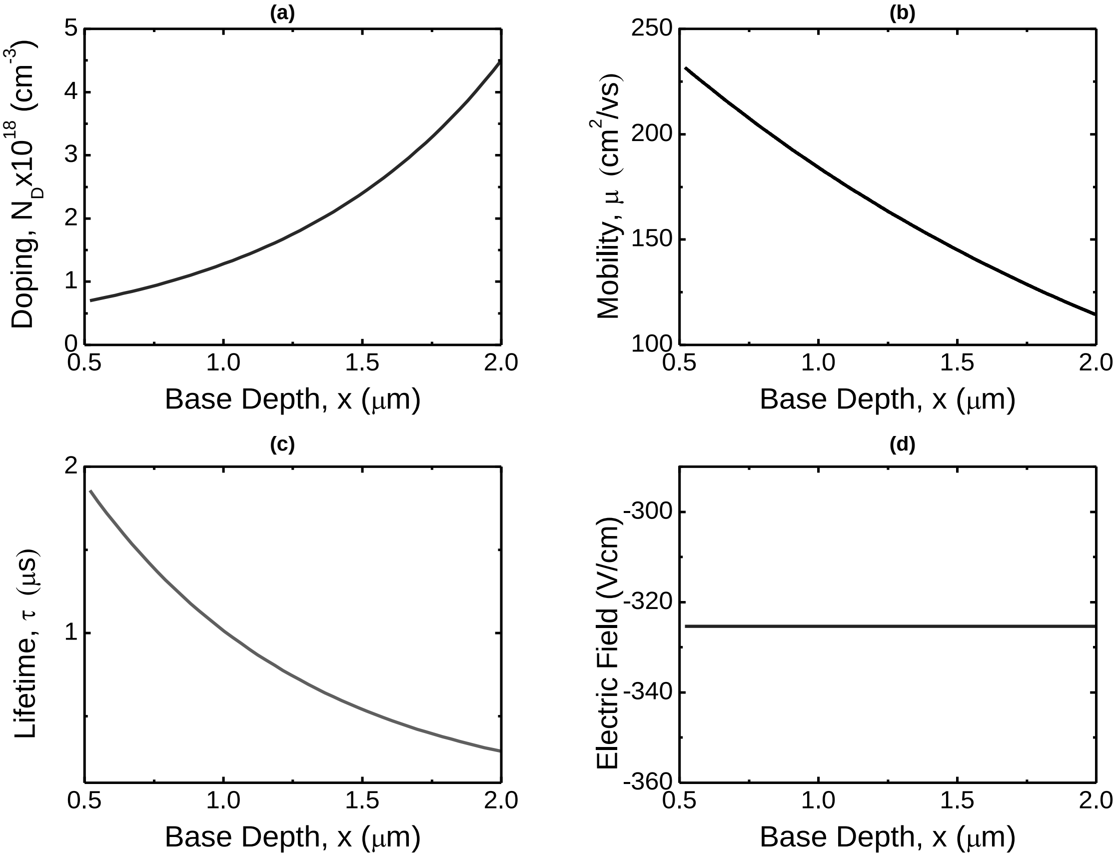

Fig 5.4. Device characteristics for exponentially doped base region of DF solar cell- (a) exponential doping variation (7×10^{17}cm^{-3} to 4.5×10^{18}cm^{-3}) with base depth (x), (b) Mobility dependence on position, (c) lifetime changing with depth, (d) Electric field inside Base for increasing exponential doping

Here, X_j can be calculated easily from the acceptor and donor doping across the E-B junction [43] (for details, see chapter 2). The solution of the drift-diffusion equation will be similar to (3.19), but the coefficients of solution will change depending on the abovementioned boundary conditions. The resulting hole concentration inside the base is depicted in fig. 5.5. Again, the COMSOL model ensures the mathematical soundness of our analytical model. The TCAD model of ATLAS also shows close match with mathematical solution.

The effect of BGN is also investigated for the base. As seen in fig 5.6., BGN affects the hole conc. very little and near the back surface only. This is understandable because doping is gradually exceeding 7×10^{17} cm^{-3} (after which BGN becomes dominant) towards the back interface.

To investigate the effect of surface recombination velocity (SRV), both surface (front & back) recombination velocity for electron and hole is varied for a wide range. The effect is apparent in fig. 5.7–5.10, where the high recombination velocity has necessarily reduced the minority carrier concentration at the surface. The result has been compared with ATLAS Device Simulator and the match is significant between the numerical and analytical model. In this numerical model, concentration dependent models, CONMOB and SRH are included, but no BGN model is incorporated.

We have investigated how well our model can predict the surface effects when extreme conditions are forced. As observed in fig. 5.9, this model can handle very high recombination velocity, e.g. like those in metal with ohmic contact. On the other hand, low SRV e.g. 1 m/s in fig. 5.9 also works for this model.

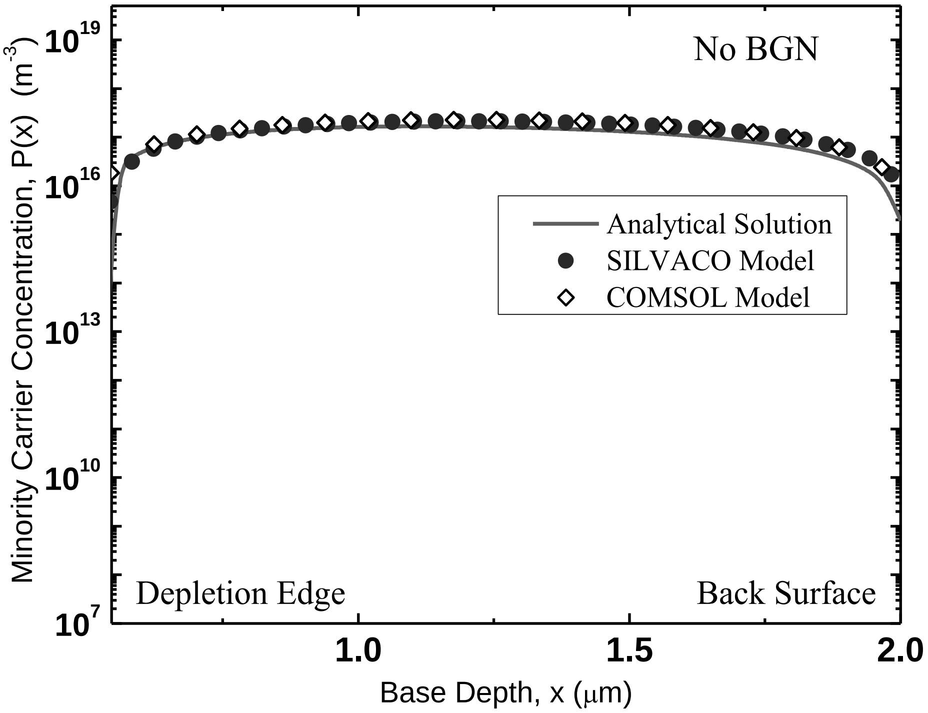

Fig 5.5. Minority carrier hole concentration for exponentially doped n-type Base. The Back surface recombination velocity (S_p) is 5×10^2 cm/s. The line represents our analytical model. The symbols represent numerical solution: COMSOL Model and ATLAS model.

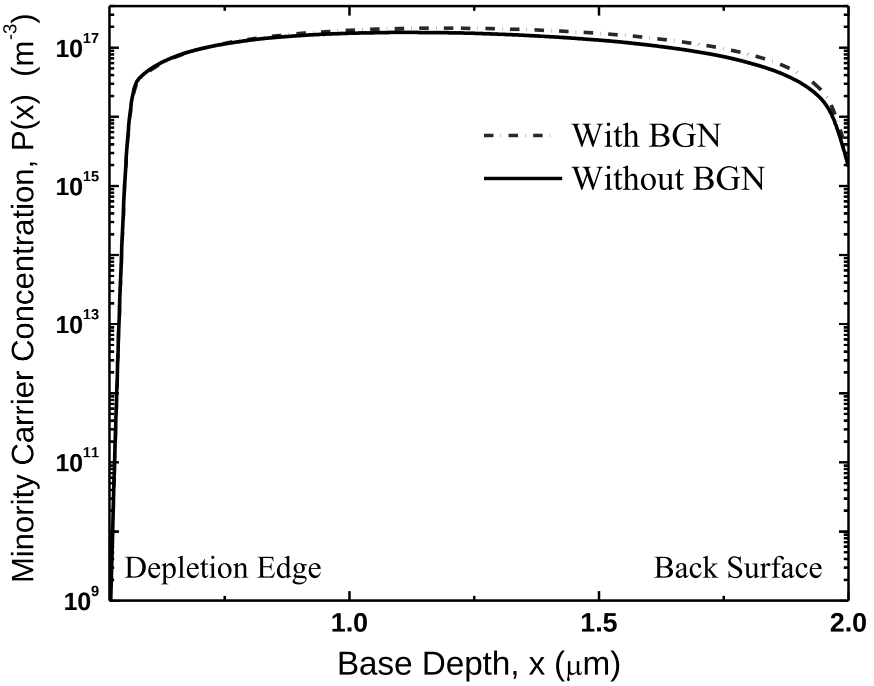

Fig 5.6. The effect of BGN on Minority carrier hole concentration in Base: The Back surface recombination velocity (S_p) is 5×10^2 cm/s.

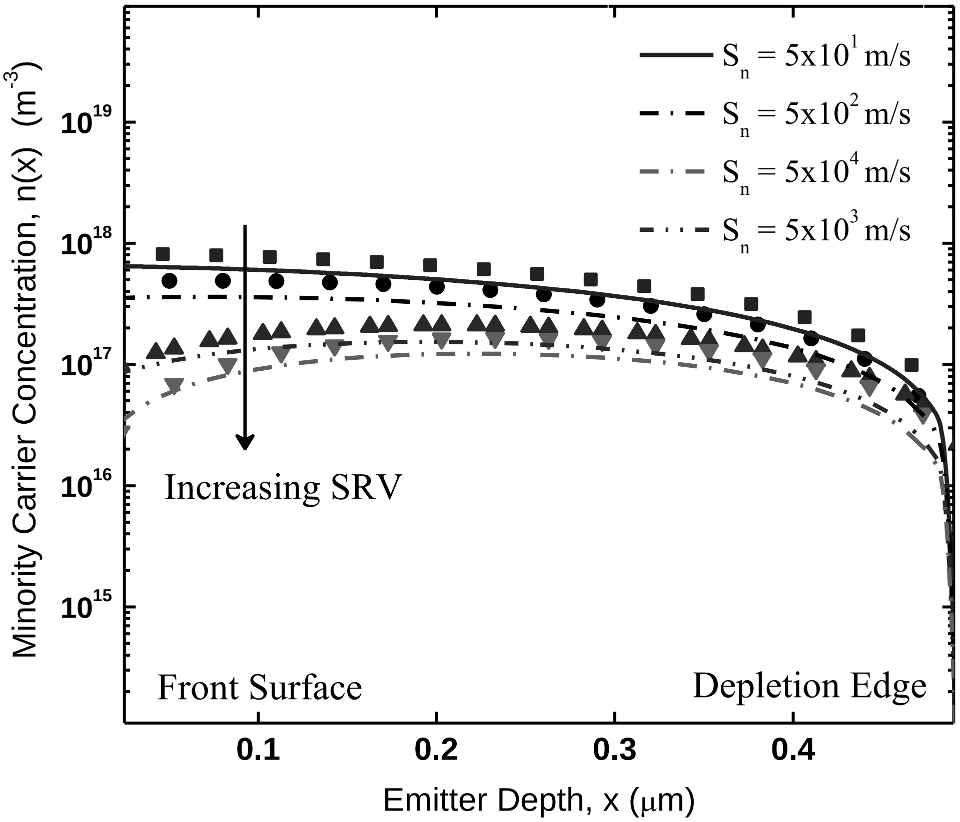

Fig 5.7. Effect of surface recombination on carrier concentration (electron). The front surface recombination velocity (S_n) varies from 5 × 10^3 cm/s to 5 × 10^6 cm/s. The symbols represent the solution from ATLAS model and lines indicates analytical model. Band gap narrowing is ignored. Spectrum: AM1.5

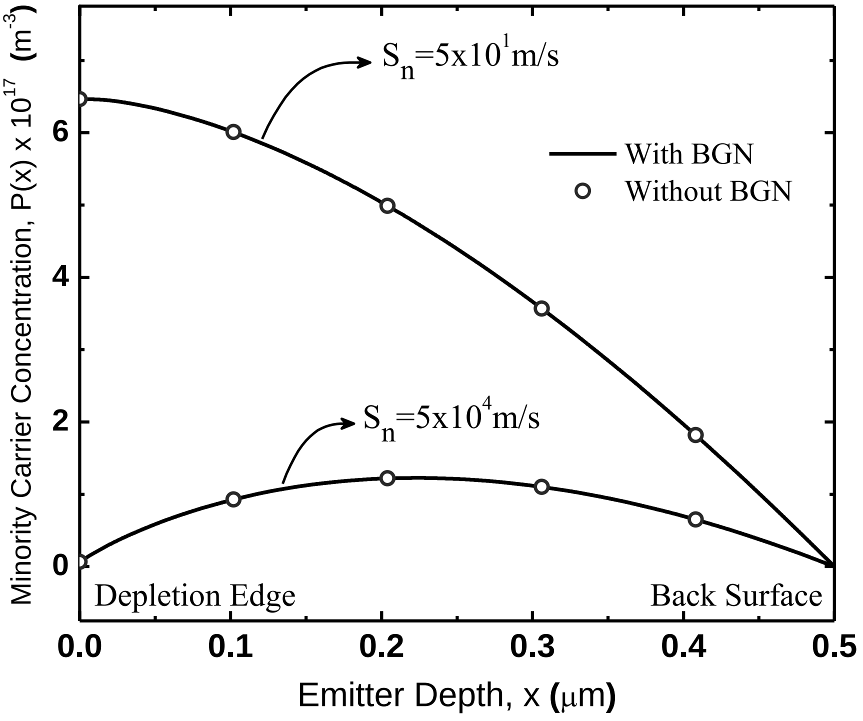

Fig 5.8. comparing the effect of Band gap narrowing on the carrier profile in emitter

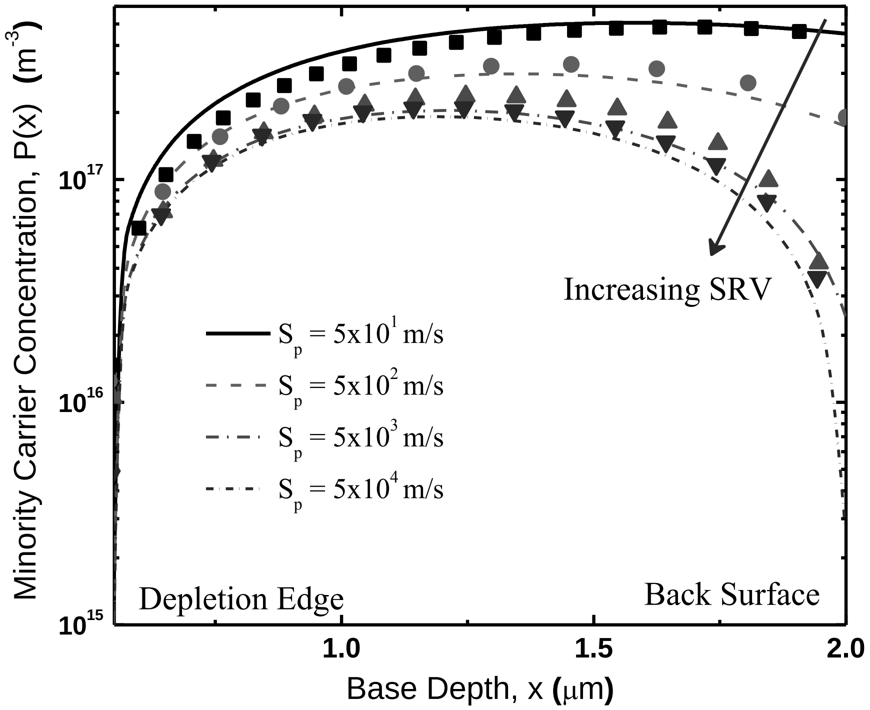

Fig 5.9. Effect of surface recombination on carrier concentration (hole) for exponentially doped base. The SRV (S_P) varies from 5 × 10^3 cm/s to 5 × 10^6 cm/s. The symbols represent the solution from SILVACO model and lines indicates analytical model. BGN is ignored. Spectrum: AM1.5

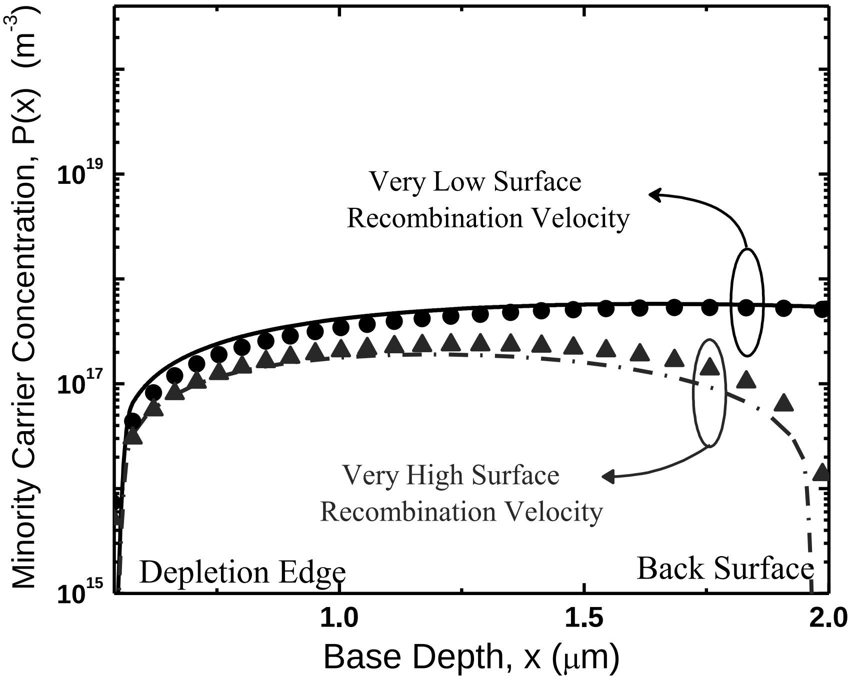

Fig 5.10. Some extreme cases of Surface Recombination velocity are investigated (SRV: 1m/s and 10^{20}m/s). The symbols represent the solution from ATLAS model and lines indicate analytical model.

The electric field inside the device is zero at the uniformly doped emitter as it should be (since no dopant variation and no band gap variation). At the quasi-neutral base side, the electric field is constant, as predicted by equation (3.6). We are not deriving E(x) inside the depletion region, since the expression of E(x) is quite common in standard textbooks [43].

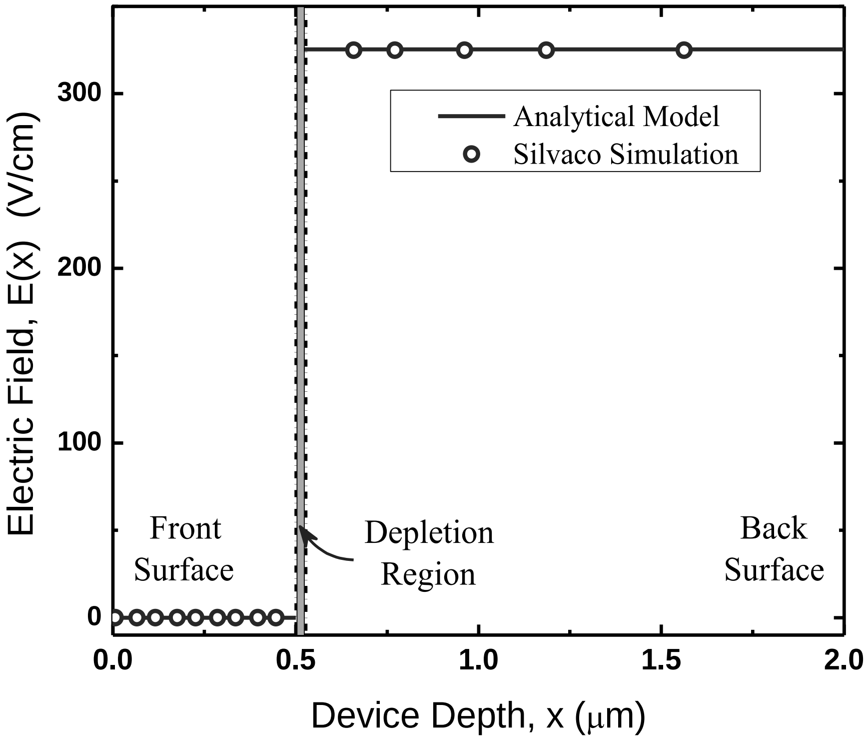

Fig 5.11. Electric field inside the solar cell: Solid line represents the analytical solution and symbols indicate the numerical data.

5.3. Minority Carrier Current Density

If the minority carrier profile is known all over the device, then it is quite easy to calculate the minority carrier current density inside DF solar cell. For P+ uniformly-doped emitter region, the current density is described by equation (3.35). The drift component of hole current will certainly be negligible (as electric field is zero). But the diffusion component of hole current density will exist inside emitter, as given by following equation –

$$J_{n\text{-}Diff}(x) = qV_T MN^{-m} \left[\underbrace{b_u C_1 exp\left(b_u x\right) - b_u\, C_2 exp\left(-b_u x\right)}_{\text{Dark Response}} + \underbrace{\left(\frac{N_{d0}{}^{m}}{MV_T}\right) \sum_{i=1}^{5} \left(\frac{a_i b_i}{b_i^2 - b_u{}^2}\right) exp(-b_i x)}_{\text{Contribution from Solar Spectrum}} \right] \tag{5.2}$$

As we can see from fig. 5.12, the electron current density is divided in two parts – dark current and illumination current. The total current is a superposition of both components. Now, to find out the minority carrier current variation in exponentially-doped n-base region, the compact equation in section 3.6 will be used. Since electric field exists in this region, both drift and diffusion component will be dominant factors. The minority carrier (Hole) current density is repeated here in equation (5.3). The comparison of hole current density with ATLAS model shows good agreement with our model (fig. 5.12). Fig. 5.13 stands for the base region that shows the drift ($J_{P\text{-}Drift}$) and diffusion ($J_{P\text{-}Diff}$) components that together shape the total current density, J_{TOTAL}.

$$\begin{aligned} J_P(z) = {} & C_1\left[qMN_{d0}^{-m} V_T \alpha z^{\left(\frac{-2m}{m+k}\right)} \left\{ (f-1)R_{11}(z) - \left(\frac{m+k}{2}\right) zX_{11}(z) \right\} \right] \\ & + C_2\left[qMN_{d0}^{-m} V_T \alpha z^{\left(\frac{-2m}{m+k}\right)} \left\{ (f-1)R_{12}(z) - \left(\frac{m+k}{2}\right) zX_{12}(z) \right\} \right] \\ & + \left[qMN_{d0}^{-m} V_T \alpha z^{\left(\frac{-2m}{m+k}\right)} \left\{ (f-1)R_{13}(z) - \left(\frac{m+k}{2}\right) zX_{13}(z) \right\} \right] \end{aligned} \tag{5.3}$$

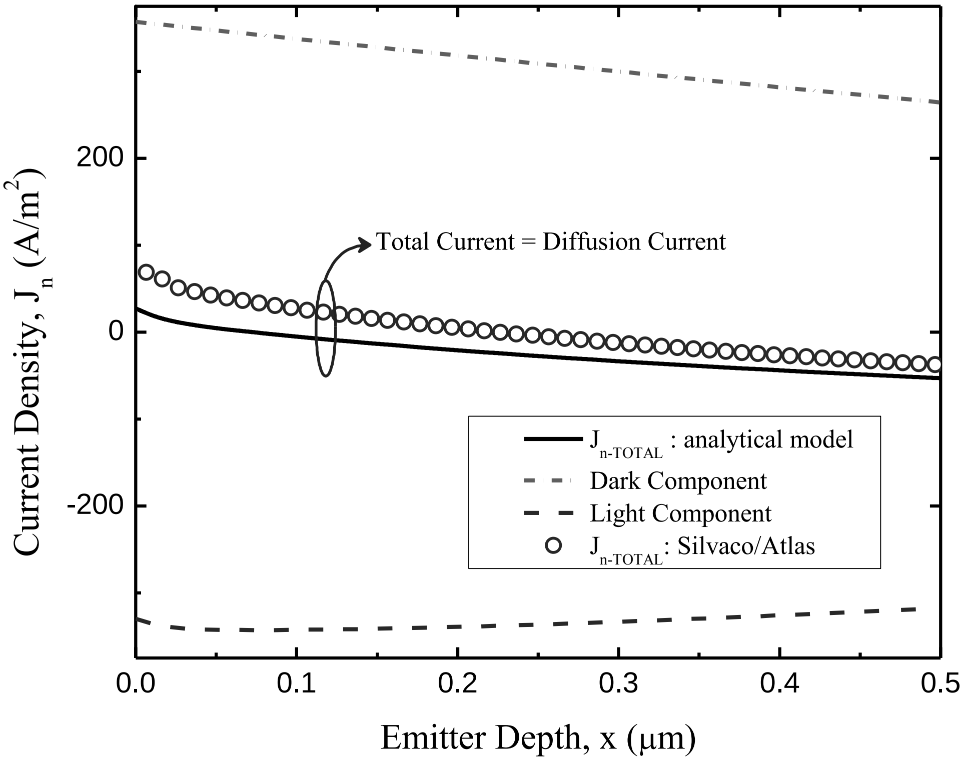

Fig 5.12. Electron current Density inside emitter: line represents the analytical solution and Symbol represents TCAD simulation

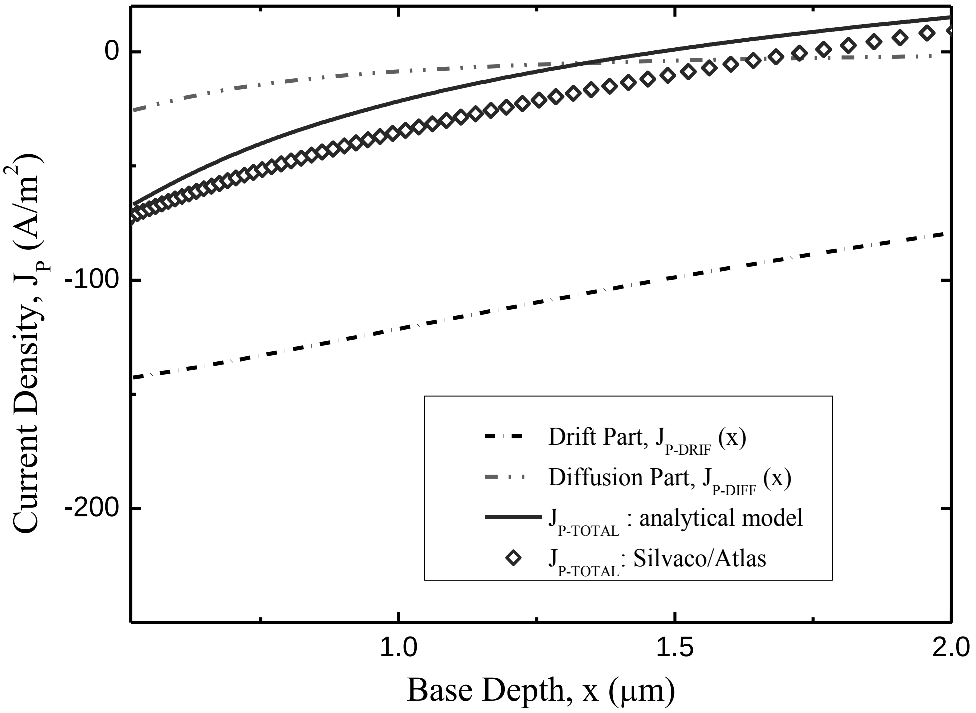

Fig 5.13. Hole current Density inside Base: line represents the analytical solution and Symbol represents TCAD simulation

5.4. Effect of Spectrum

The attractive feature of this model is the inclusion of solar spectrum in a compact expression, without using elaborate numerical approach. Besides, this solution does not need any number of iterations to show satisfactory correct results with experimental data and device simulator. In this section, we will consider the effect of two different solar spectrums: AM1.5D and AM1.5G. According to NREL, these are standard solar spectrum for terrestrial applications [66]. The details are also presented in Appendix D.

As explained in chapter 3, the spectrum is included in the solution process using approximated carrier generation rate equation, which is repeated here for helping the discussion –

$$G_{\text{approx.}}(x)=\sum_{i=1}^{5}\mathrm{a}_{\mathrm{i}}\exp\left(-b_i x\right)$$

The a_i and b_i values needed for approximated G is tabulated in the following table [57, 59]:

Table 5.1. Coefficients a_i ($\times 10^{20}\,s^{-1}cm^{-3}$) and b_i ($\times 10^{4}\,cm^{-1}$) in Si for different solar spectrum

Co-efficient (a_i, b_i)	AM1.5D (Diffused)	AM1.5 G (Global)	AM0 (Space)
a1	28.63	50.63	27.09
a2	6.60	10.00	13.03
a3	4.20	3.90	6.23
a4	0.511	0.45	1.02
a5	0.0211	0.0201	0.103
b1	70.44	65.44	30.81
b2	3.72	3.72	3.568
b3	0.35	0.35	0.571
b4	0.0720	0.0620	0.116
b5	0.0055	0.0061	0.0175
Approximated Carrier Generation, G(x)	$\mathrm{G}=\sum_{i=1}^{n}\mathrm{a_i}\exp(-\mathrm{b_i}\mathrm{x})$		

5.4.1. Effect of Changing Solar Spectrum on Carrier Concentration

To observe the effect of AM1.5G and AM1.5D, we are considering a heavily-doped n-type emitter. To include the AM1.5D spectrum, simply the a_i and b_i values from Table 5.1 will be included in the expression of minority carrier concentration. To verify that our mathematical model is correctly predicting the solar cell performance under different spectrum in 1-Sun condition, Hole concentration from all the irradiation is compared with Silvaco/ATLAS simulation. The top surface recombination velocity is 5×10^4 cm/s and the biasing voltage is 0V. The doping profile is exponentially varying from top surface (10^{20} cm^{-3}) to the E-B junction at 0.5 μm (7×10^{18} cm^{-3}).

As seen in fig. 5.14-5.15, the analytical model works fine for both spectrums. It should be noted that the change in hole concentration due to change in spectrum from AM1.5D to AM1.5G is very little. The reason behind this is that both are standard terrestrial irradiance with almost similar spectrum: AM1.5D is considering the direct irradiance and AM1.5G is including total global irradiance (see Appendix D: Section D.1). Hence, fig. 5.14 and fig.5.15 has very small change.

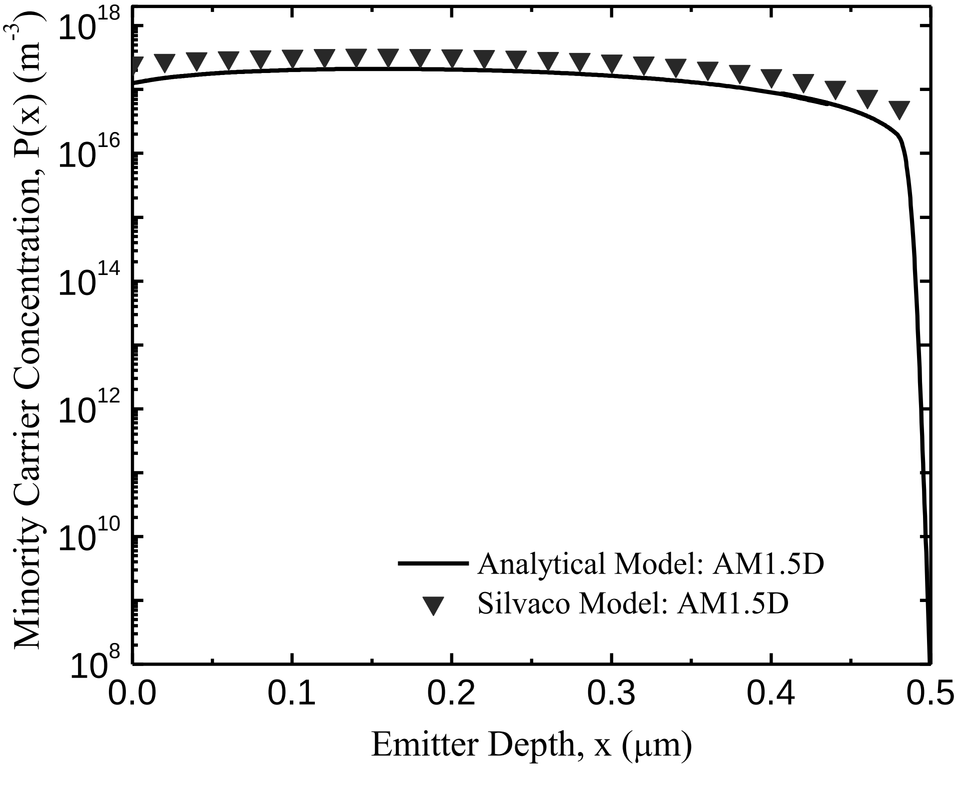

Fig 5.14. Effect of spectrum on carrier concentration. Spectrum: AM1.5D. line represents the analytical solution and Symbol represents TCAD simulation

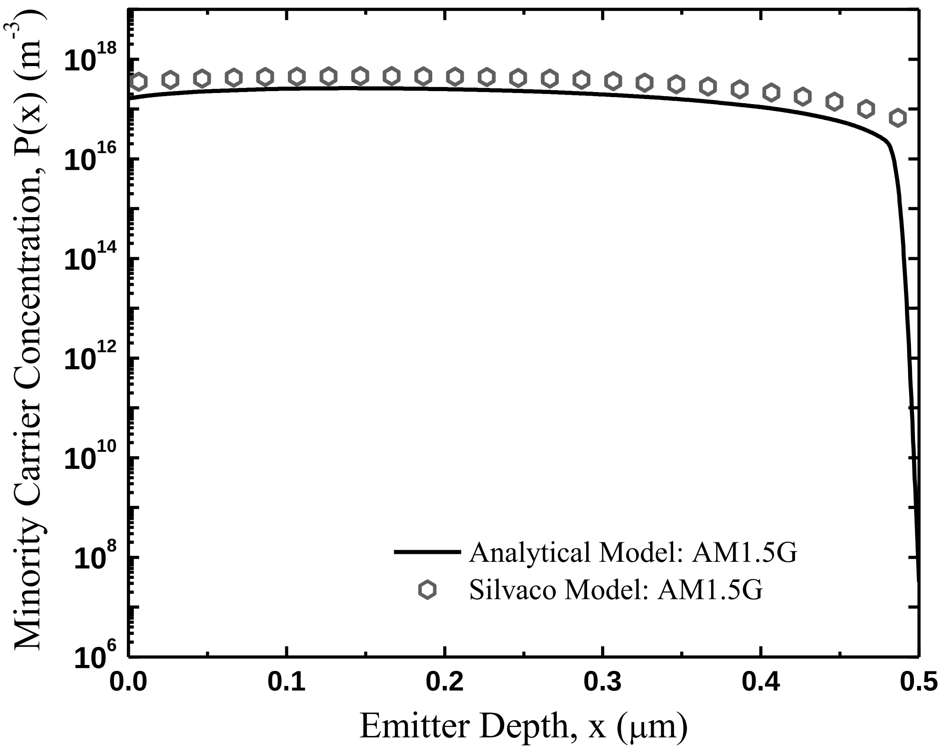

Fig 5.15. Effect of spectrum on carrier concentration. Spectrum: AM1.5G. line represents the analytical solution and Symbol represents TCAD simulation

5.4.2. Comparing Approximated and Simulated Generation Rate

It is desirable to find out how good the approximation of G is when compared to TCAD device simulator. As seen in the fig. 5.16, the approximation is quite good for a typically thick solar cell (above 300μm), but the 5-term approximation of equation (3.3) shows error for small depth. This is certainly a concern for thin cells. Fig. 5.17 reveals that the approximation taken for AM1.5D is better than that of AM1.5G.

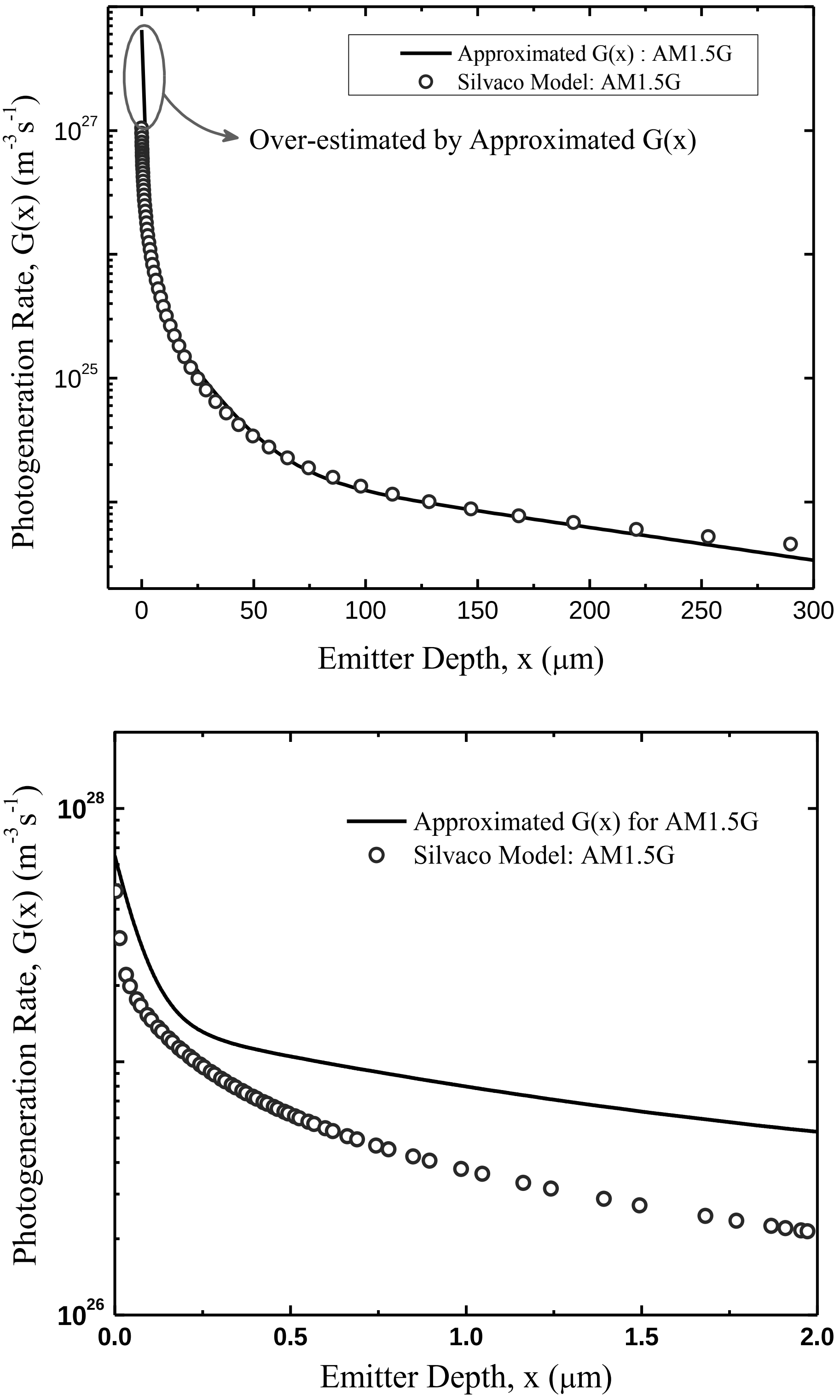

Fig 5.16. Photogeneration rate for AM1.5G (Global) solar spectrum. The solid line represents 5-term approximation of photogeneration and the symbol represents the data from TCAD simulator: (a) for a thick (300μm) Solar Cell, (b) for a thin (2μm) Cell. No reflection is considered in ATLAS model.

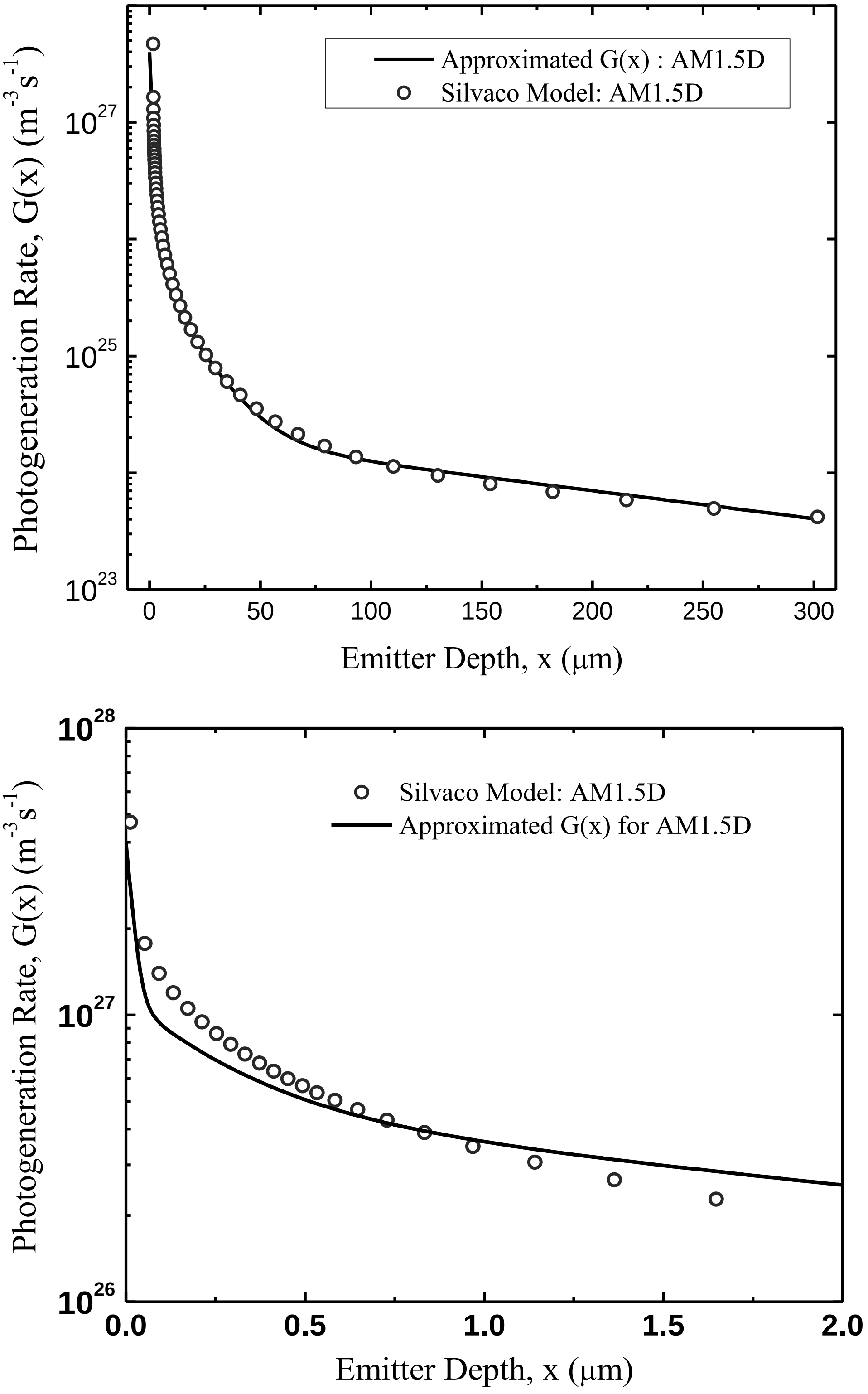

Fig 5.17. Photogeneration rate for AM1.5D (Direct) solar spectrum. The solid line represents 5-term approximation of photogeneration and the symbol represents the data from TCAD simulator: (a) for a thick (300μm) Solar Cell, (b) for a thin (2μm) Cell. No reflection is considered in ATLAS model.

For most of the cases the emitter region is very thin (around 0.5μm); hence the error in the generation rate will cause much mismatch. To correct this approximation, we are reporting a new set of a_i and b_i, as presented in table 5.2 below. The corresponding new generation rate is illustrated in fig. 5.18, along with Ray tracing simulation data. The hole concentration, using new values of a_i and b_i from table 5.2, shows that carrier distribution shows very good match with the ATLAS simulator.

Table 5.2. New Coefficients a_i ($\times 10^{20} s^{-1} cm^{-3}$) and b_i ($\times 10^{4} cm^{-1}$) in Si for different solar spectrum

New Coefficient (a_i, b_i)	AM1.5 G (Global)
a_1	78.1
a_2	15
a_3	4.8
a_4	0.8
a_5	0.0011
b_1	75.44
b_2	4.19
b_3	0.6
b_4	0.052
b_5	0.0015

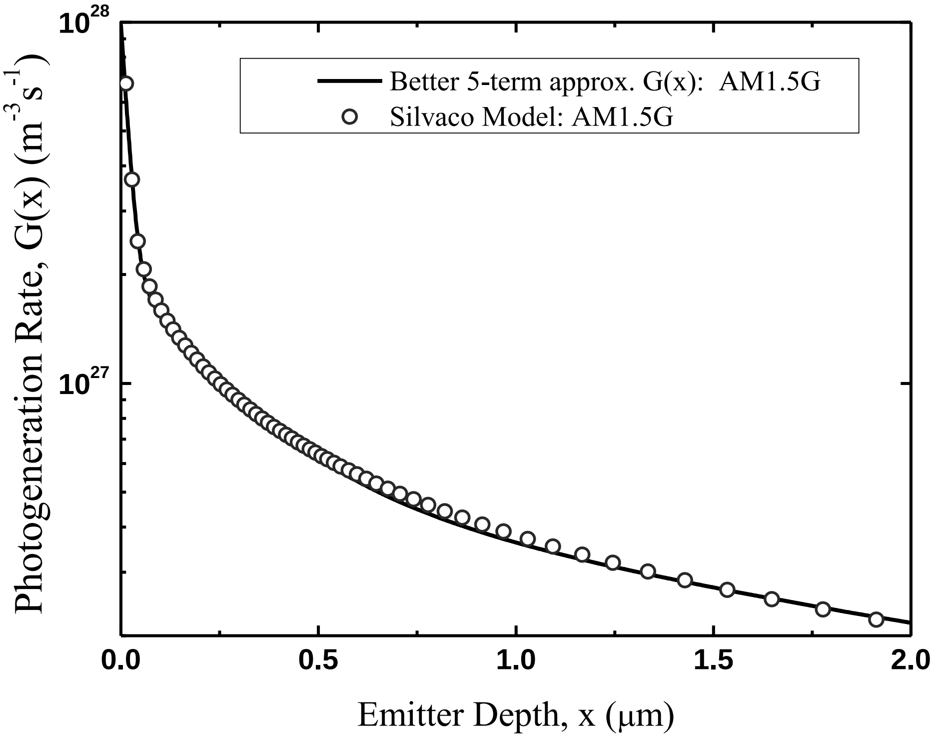

Fig 5.18. Better approximation rate for photogeneration in AM1.5 solar spectrum: The solid line represents 5-term approximation of photogeneration and the symbol represents the data from TCAD simulator

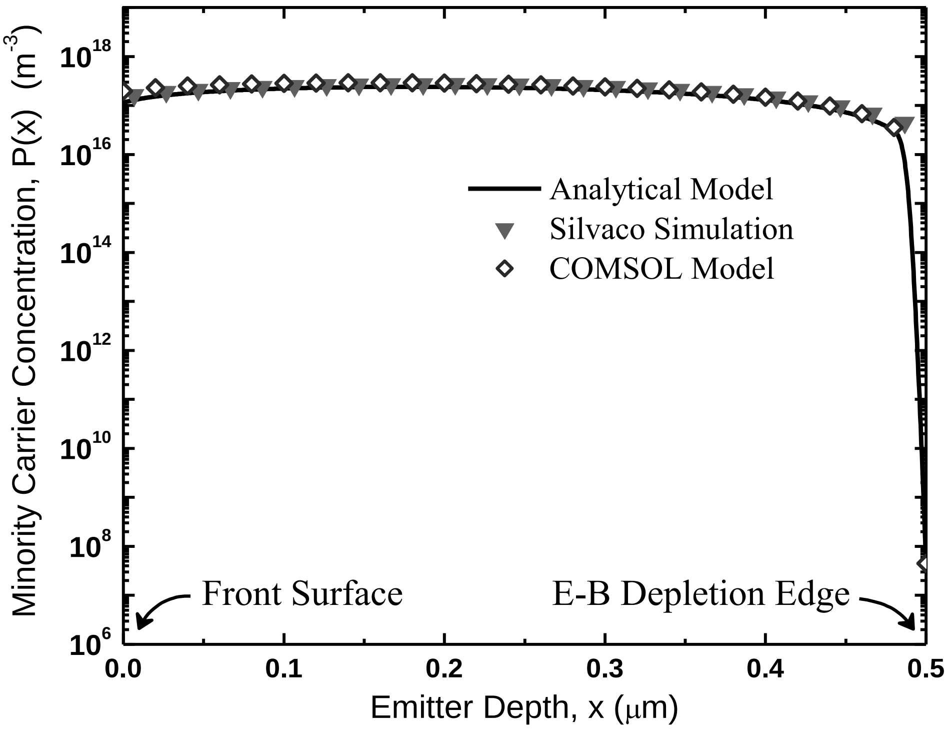

Fig 5.19. Minority carrier concentration using the better approximation in G, proposed by this work

5.5. Effect of Biasing

The effect of applied bias is embedded in the developed model through the boundary condition of Emitter-Base junction (for example, see equation (3.21)). The applied bias will certainly increase the injection of minority carrier from the base side and increase the current. To understand the effect of biasing, we will take a thin emitter (0.3 μm) as example and separate the terms which are affected by applied bias. A simple observation of the general expression for minority carrier (both electron and hole) shows that the contribution from V is hidden in the boundary constants C_1 and C_2. Increasing the applied voltage will increase the injection level in the emitter region. Besides, as evident from equation (5.4) the illumination term is not affect at all by the applied voltage.

$$
\begin{aligned}
p(z) = {} & \overbrace{\left[\underbrace{\frac{\dfrac{n_i^2}{N_d(z_j)}\exp\left(V/V_T\right)}{P_1(z_j) - \dfrac{T_{21}(z_0)}{T_{22}(z_0)}P_2(z_j)}}_{\text{Contribution from Biasing}} + \underbrace{\frac{T_{23}(z_0) + \dfrac{T_{22}(z_0)}{P_2(z_j)}P_3(z_j)}{T_{21}(z_0) - \dfrac{T_{22}(z_0)}{P_2(z_j)}P_1(z_j)}}_{\text{Contribution from Spectrum}} \right]}^{C_1} z^A I_v(\beta z) \\
& + \overbrace{\left[\underbrace{\frac{\dfrac{n_i^2}{N_d(z_j)}\exp\left(V/V_T\right)}{P_2(z_j) - \dfrac{T_{22}(z_0)}{T_{21}(z_0)}P_1(z_j)}}_{\text{Contribution from Biasing}} + \underbrace{\frac{P_1(z_j)\dfrac{T_{23}(z_0)}{T_{21}(z_0)} + P_3(z_j)}{\dfrac{T_{22}(z_0)}{T_{21}(z_0)}P_1(z_j) - P_2(z_j)}}_{\text{Contribution from Spectrum}} \right]}^{C_2} z^A I_{-v}(\beta z) \\
& + \underbrace{P_3(z)}_{\text{Illumination term}}
\end{aligned}
\tag{5.4}
$$

To observe the impact of increasing injection level on a 0.3 μm emitter, biasing is varied from 0.1 to 0.7V. As seen in fig. 5.20 below, the minority carrier at the junction gradually increases due to high injection from the base side. If the voltage is very high, the low injection condition becomes invalid. Fig. 5.20 shows that, when V is near 0.7V, the minority carrier concentration becomes comparable to majority carrier concentration (or, alternatively the doping density). Since generally the analytical models work on the basic assumption of low injection, this solution also should not be used for biasing beyond 0.8 V.

Since the complete expression of current density is known to us (from chapter 3), J-V curve for this device structure is straightforward to calculate. A closer look at the compact expression for current density (both drift and diffusion) reveals that, only the dark component contains C_1 and C_2. Since the expression of C_1 and C_2 (see equation (5.4)) contains the Voltage part only, it is obvious that the current is proportional to the exponential variation of applied voltage. It is also obvious from the current equations that the contribution from the solar spectrum works like a constant current source, irrespective of the applied biasing. This is consistent with basic photovoltaic physics.

$$J_{P-Diffusion}(z)=\underbrace{C_1\left[qMN_{d0}^{-m}V_T\alpha z^{\left(\frac{k-m}{m+k}\right)}\left(\frac{m+k}{2}\right)X_1(z)\right]+C_2\left[qMN_{d0}^{-m}V_T\alpha z^{\left(\frac{k-m}{m+k}\right)}\left(\frac{m+k}{2}\right)X_2(z)\right]}_{\text{Dark Component}}$$

$$+\underbrace{\left[qMN_{d0}^{-m}V_T\alpha z^{\left(\frac{k-m}{m+k}\right)}\left(\frac{m+k}{2}\right)X_3(z)\right]}_{\text{Contribution from Solar Spectrum}}$$

$$J_{P-Drift}(z)=\underbrace{C_1\left[qMN_{d0}^{-m}V_T\alpha z^{\left(\frac{-2m}{m+k}\right)}(1-f)P_1(z)\right]+C_2\left[qMN_{d0}^{-m}V_T\alpha z^{\left(\frac{-2m}{m+k}\right)}(1-f)P_2(z)\right]}_{\text{Dark Response}}$$

$$+\underbrace{\left[qMN_{d0}^{-m}V_T\alpha z^{\left(\frac{-2m}{m+k}\right)}(1-f)P_3(z)\right]}_{\text{Contribution from Solar Spectrum}}$$

Fig. 5.21 illustrates the current density for various voltages. As the J-V curve is now acquired, calculations of the key parameters (efficiency, FF) are just some trivial work. For example, the open circuit voltage for this thin emitter is found to be 0.55V and the short circuit current is nearly 30 A/m^2.

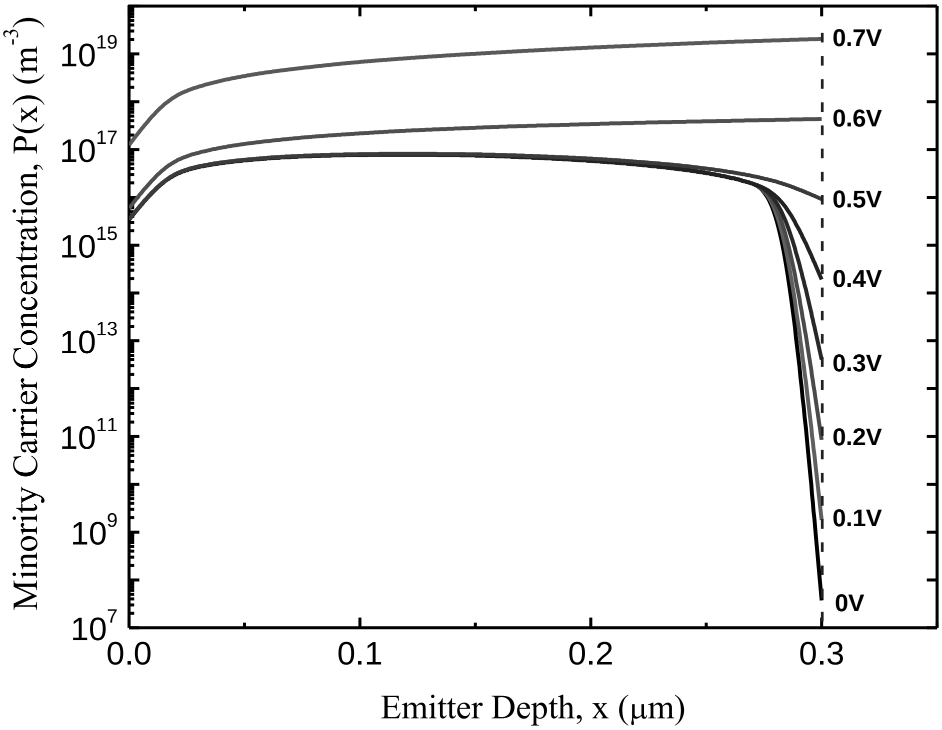

Fig 5.20. The minority carrier concentration for different applied bias. Thin emitter (0.3 μm) is considered with high surface recombination velocity (5 × 10^6 cm/s).

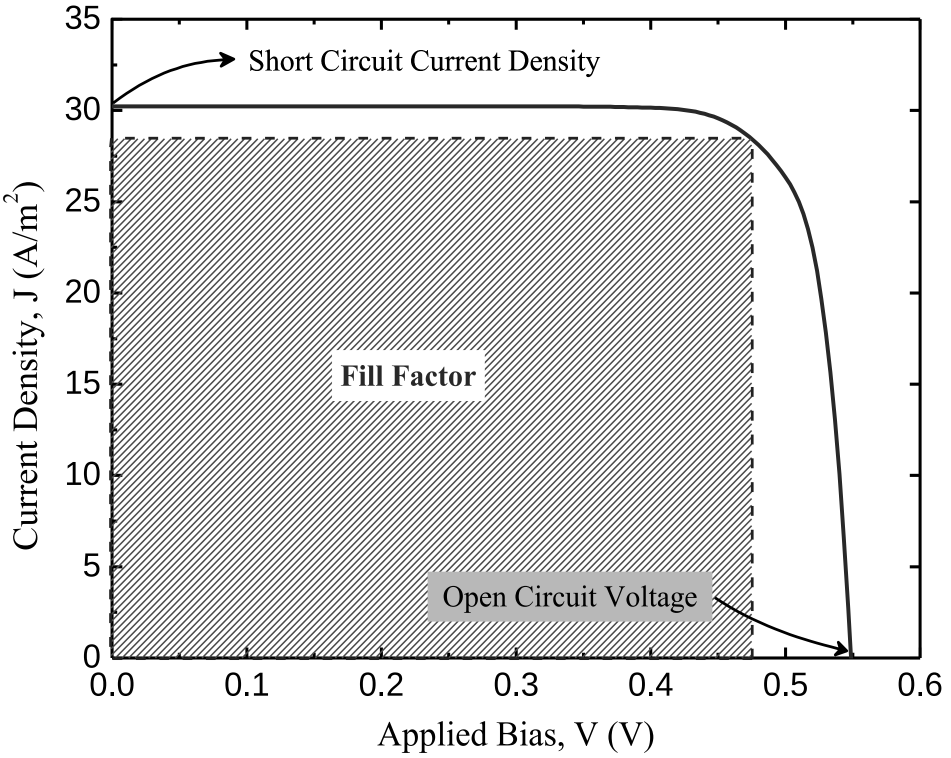

Fig 5.21. J-V curve obtained from the compact model

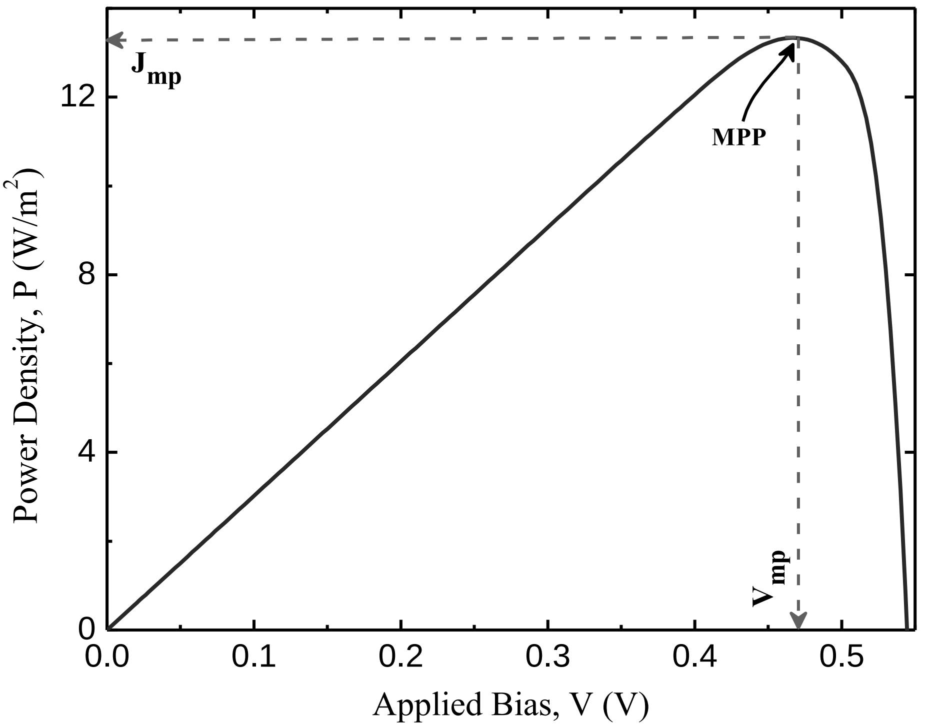

Fig 5.22. P-V curve obtained from the compact model

From the J-V curve, the power-voltage curve and the corresponding MPP point can be easily obtained by applying the theory in Chapter 2. As seen in fig. 5.21 and 5.22, the optimal operating voltage and current density is 0.475 V and 28.5 A/m^2 respectively, with an optimal power density of 13.3W/m^2. The fill factor square is also shown in fig. 5.21.

Comparison with the experimental work:

A commercial (R.T.C France) silicon solar [76] cell is considered to compare with the proposed analytical model. Their experimental I-V data is obtained under controlled conditions from an automated measuring system with a CBM 8096 microcomputer acting as the controller which once finishes the acquisition of data, starts executing the optimization program in order to determine the model parameters. The cell key parameters from [76] is presented below –

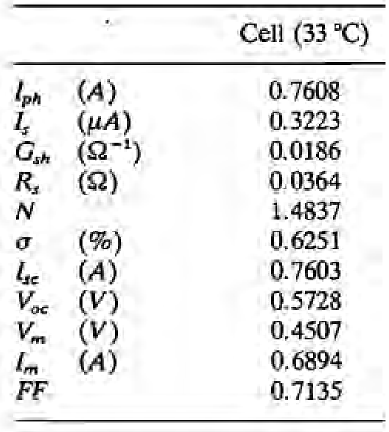

		Cell (33 °C)
I_{ph}	(A)	0.7608
I_s	(μA)	0.3223
G_{sh}	(Ω^{-1})	0.0186
R_s	(Ω)	0.0364
N		1.4837
σ	(%)	0.6251
I_{sc}	(A)	0.7603
V_{oc}	(V)	0.5728
V_m	(V)	0.4507
I_m	(A)	0.6894
FF		0.7135

The experimental result is compared to the result of our analytical model. As seen from fig. 5.23 below, the mathematical model shows promising matching with the experiment. The mismatch near the MPP (Maximum Power Point) can be explained easily from the concept of shunt and series resistance. As explained by Prince [77], when the series and shunt resistances are negligible (R_{series}=0 and R_{shunt}=∞), the I-V curve follows a sharp fall (like in our model). But if the series resistance becomes significant (even near 5Ω), the I-V curve falls drastically. The experimental R.T.C France solar cell contains series resistance, hence the curve in fig. 5.23 is different because in our model, no series resistance is included in the analysis.

The open circuit voltage from experimental solar cell is also close enough with the developed analytical model.

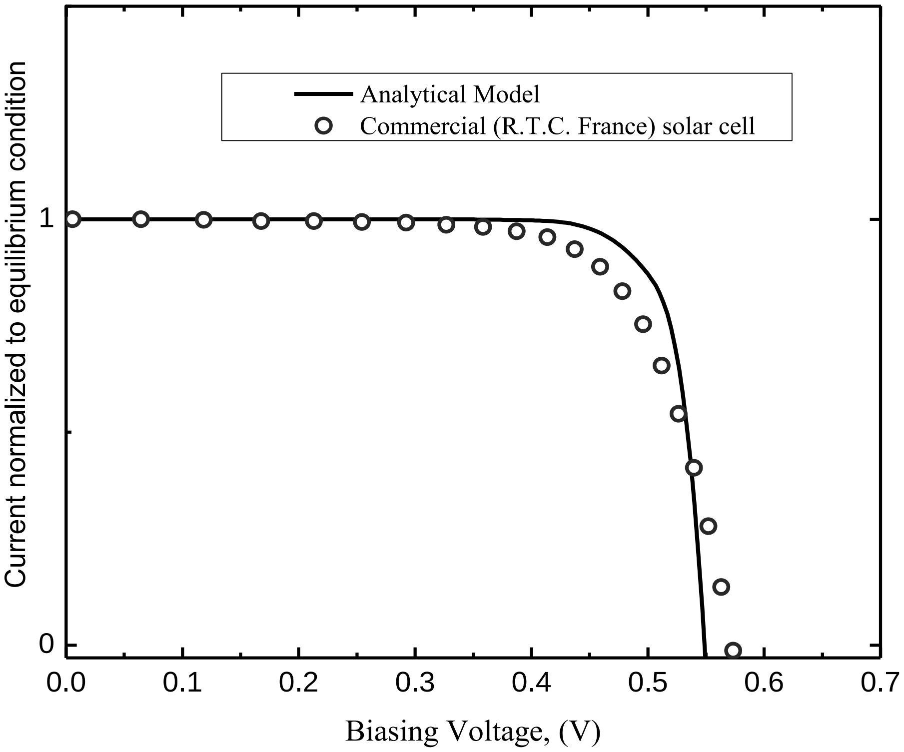

Fig 5.23. Comparison of the analytical I-V characteristics with the experimental solar cell module data from [76]

5.6. Effect of Thickness

In this section, the applicability of our model will be analysed when the emitter thickness is varied from thin layer to thick layer. First, five emitters with different thickness are considered to observe the trend in carrier concentration. From fig. 5.23, it is found that when doping gradient α is kept constant ($\alpha = 5.6268\times10^6$) and emitter depth is gradually increased, the corresponding hole concentration just spreads over the emitter (range of x_j). The resulting hole concentration is almost similar in shape near the junction. This can be explained since for very thin emitter (0.1µm), the surface and junction are too close and they drag the p(x) together than the p(x) for thick emitter (0.5µm). Since α is same for all five emitter profile, the Electric field (and hence, drift component of p(x)) will be same. The diffusion component, however, has spacial dependence and will vary with x. This can also be understood from the current density variation for the five cases of emitter profile.

The effect of emitter thickness can be studied from another perspective. For the previous case, the exponential gradient α was kept same; so, the doping at depletion edge (at X_j)

was different for each case. Now same doping range (10^{20} cm^{-3} to 6×10^{18} cm^{-3}) will be assumed for each case of emitter (see fig. 5.24), i.e., unlike fig. 5.23, the gradient α will be different. It is seen that there is not much change in hole conc., since the doping density are closer for both cases.

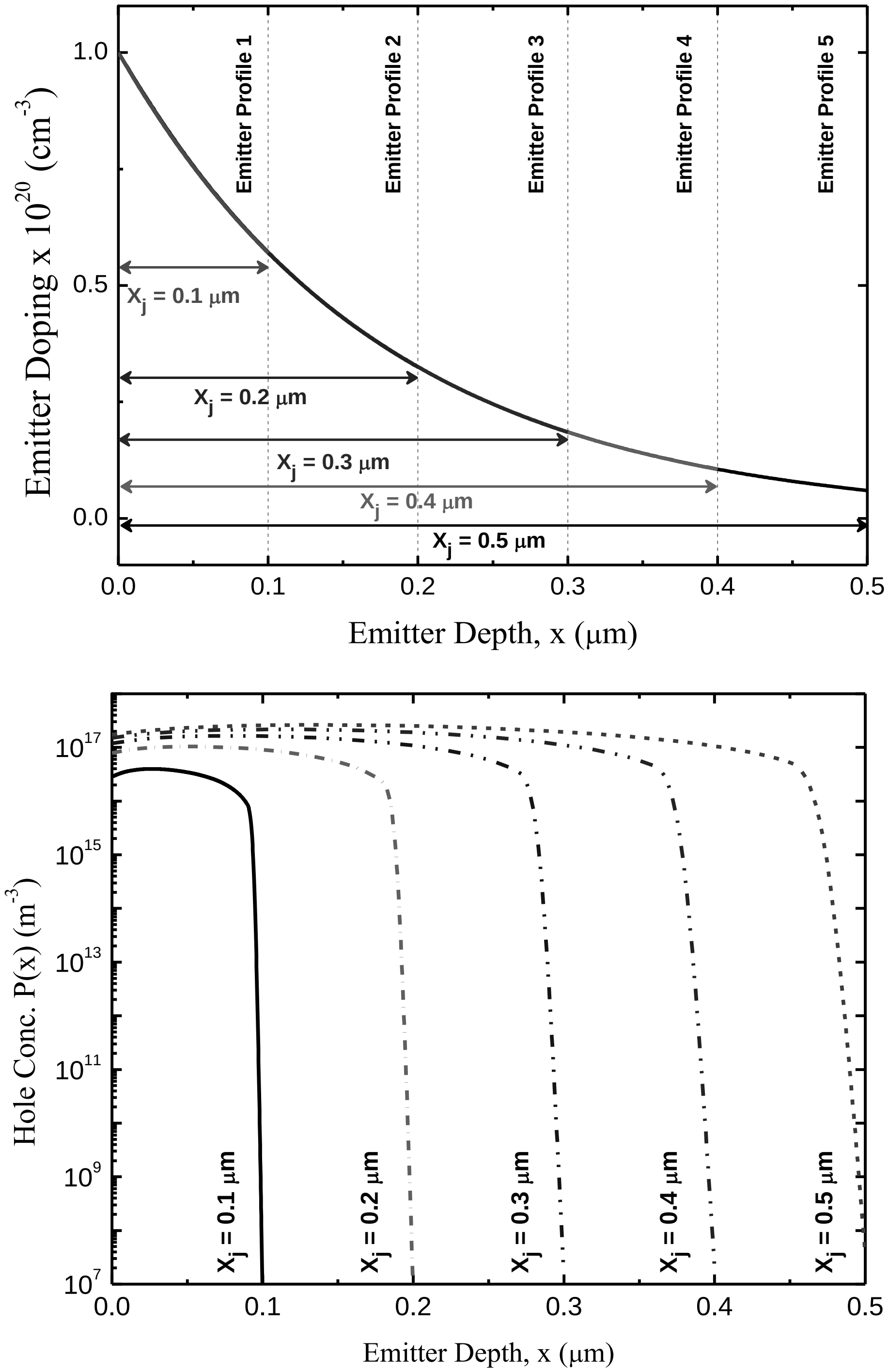

Fig 5.24. Five emitters (0.1–0.5μm thickness) are analysed for same SRV and zero bias condition. (a) The doping concentration falls with same gradient (α) in all the cases. (b) Corresponding minority carrier concentration

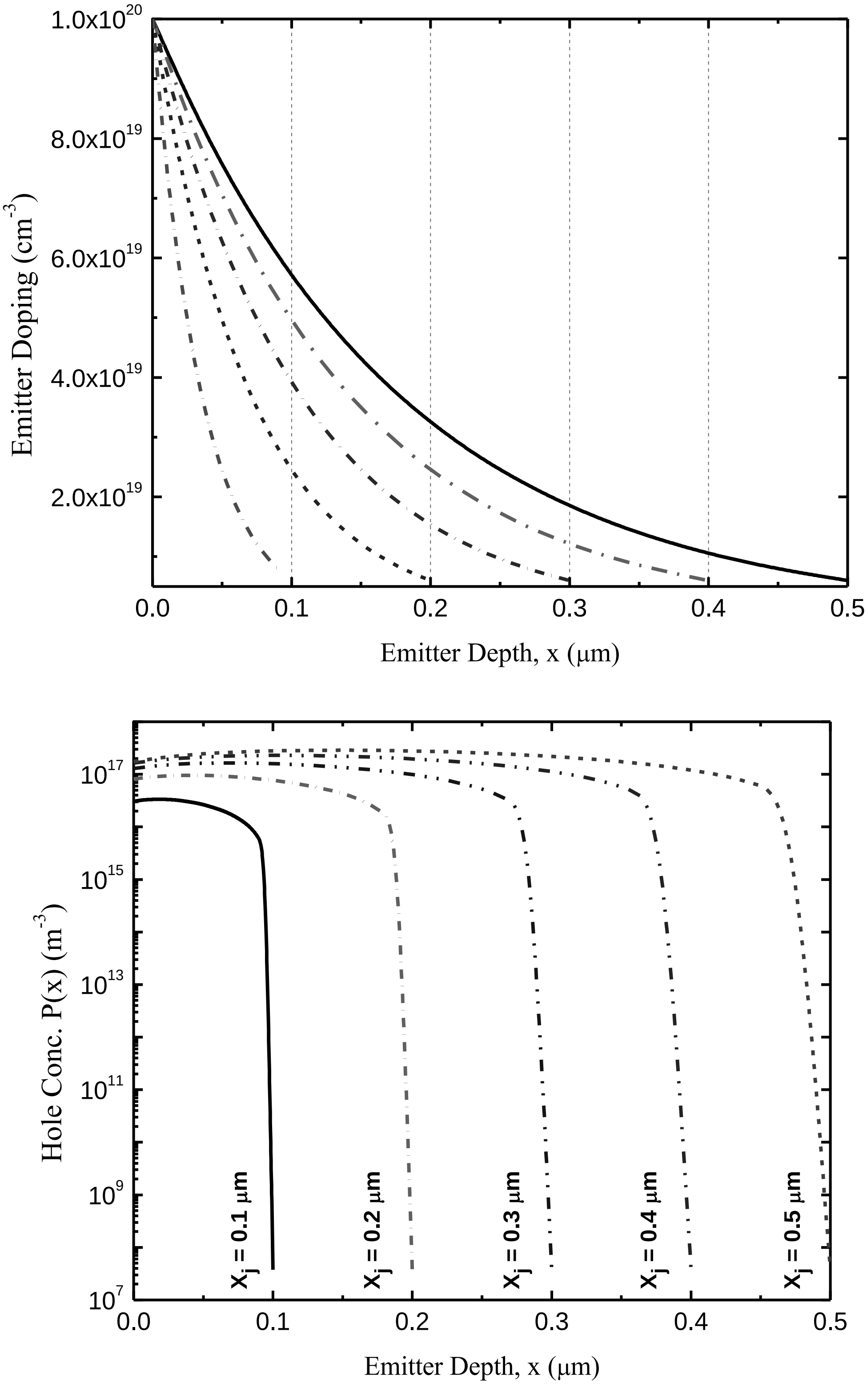

Fig 5.25. Five emitters (0.1–0.5μm thickness) are analysed for same SRV and zero bias condition. (a) The doping is maximum at the top surface (10^{20} cm^{-3}) and gradually falls to the junction-edge (6×10^{18} cm^{-3}). Same doping profiles are considered for all the emitters. (b) Corresponding minority carrier concentration

So far, thin emitter has been our main concern. But what happens when the emitter thickness exceeds the range of 'thin emitter'? To explore this situation, we will consider an n-type base region, where doping is exponentially increasing towards the back contact. The base depth is varied from 1μm to 7μm. Back Surface recombination velocity is constant (5×10^4 m/s). As seen in fig. 5.25, the effect is similar to emitter case. As the width of the base is increased, the hole concentration remains same at the boundary. Only slight increase in concentration with W is observed at the middle of the base region.

This result is important for another reason. Many of the previous analytical models work only for swallow emitter/base regions (near 0.3μm ~ 0.5μm), while our model can solve structure beyond that range. The reason behind this is that our model does not employ any kind of approximations that may arise from shallow emitters exclusively. Hence, the model is robust for both thin and thick layer of devices.

The current density profile for various base thicknesses is shown in fig. 5.26. It is noteworthy that for increasing W, the absolute value of hole current density at each boundary increases. For this specific solar cell, hole current density at the E-B junction increases 2.4 times for a 3.5 times change in base thickness.

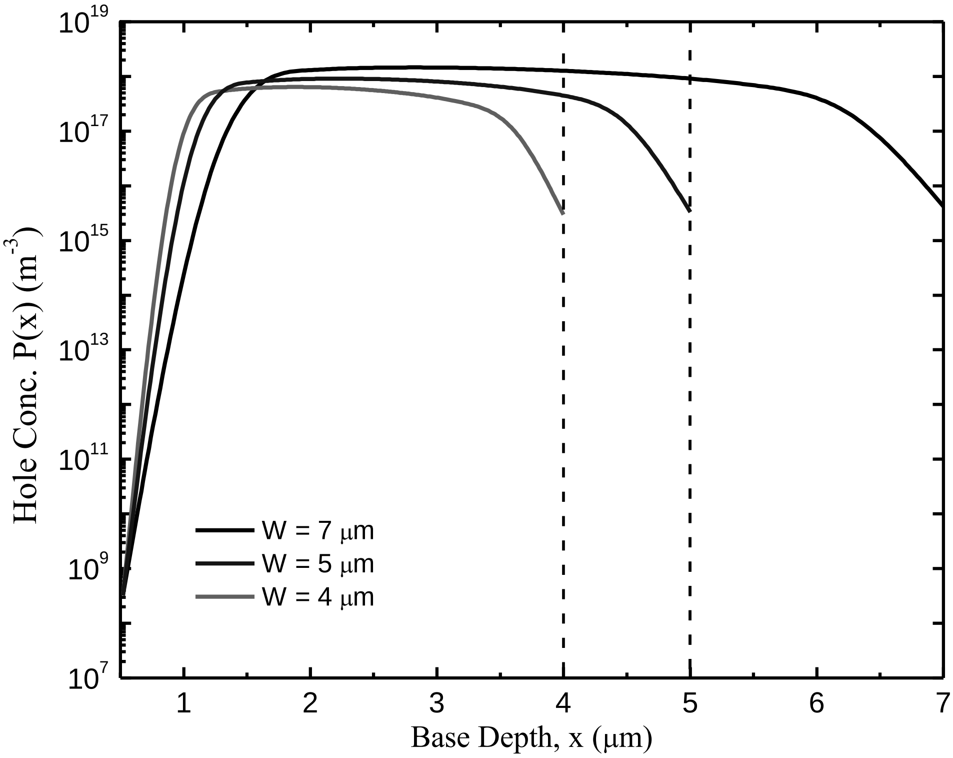

Fig 5.26. Hole concentration for three base regions for same SRV (5×10^4 m/s) and zero bias condition. The impurity concentration gradually increases towards the back contact.

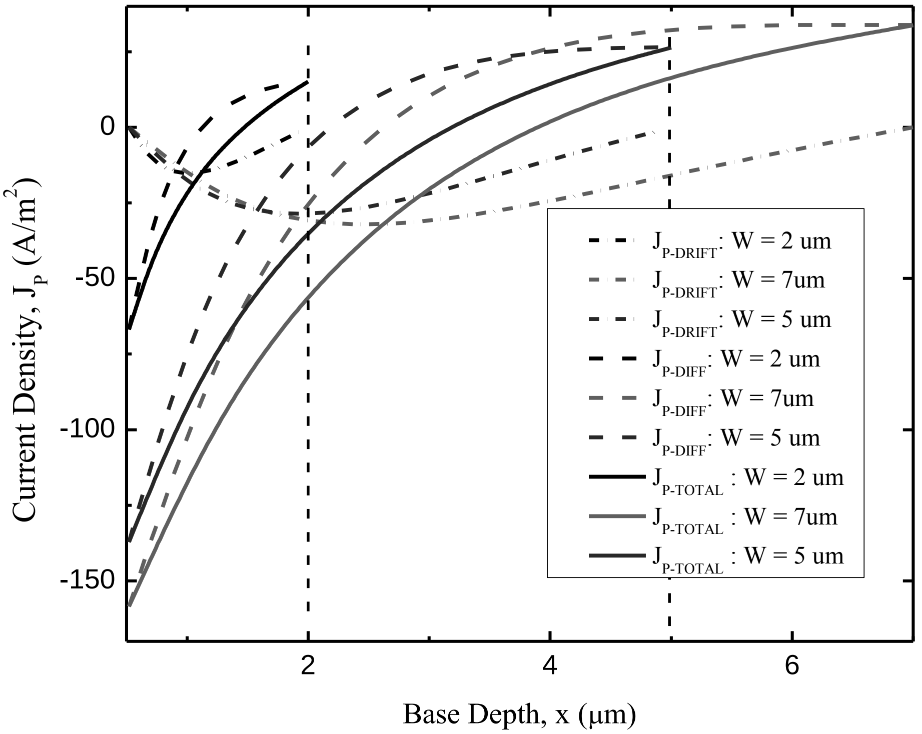

Fig 5.27. Current density for three base regions.

5.7. Analysis With Accurate Generation Rate

Generation rate is a function of depth into the material (x) and wavelength of incident solar spectrum. The light generation rate is the sum of individual contributions over the whole solar spectrum. So far, G has been approximated by a series of three to five exponential terms in previous analysis. As discussed in chapter 3, that the analytical solution obtained using approximated G has the same form when actual generation rate is considered [57]. Approximated G will now be avoided and more accurate generation rate will be the focus of this section.

Fig. 5.27 uses the general analytical expression of Section 3.8 and explains the effect of individual wavelength on the minority carrier concentration. As evident from the figure, with increasing photon energy (decreasing wavelength), the contribution to carrier concentration gradually decreases. The wavelength considered in this analysis is from 0.2 to 1.2 μm (with a 10 nm step). The reason of taking this band can be explained from fig. 3.4. The absorption for Silicon is dominant in this region.

In fig. 5.27, the hole concentration at the junction is same for all wavelength, but the surface concentration depends on the incident photon energy. Besides, the concentration does not have similar profile for some wavelength; for example, at 0.9 μm, the surface carrier concentration suddenly increases (marked with arrow). The reason behind this is the unevenness in absorption coefficient and sudden change in solar spectrum. Studying this type unexpected change is possible with our model.

It should be noted that the small change in one wavelength will not change the overall hole concentration over the device, because the overall hole concentration is the summation (integration) of the all contributions. Hence for monochromatic study, as well as for study of overall spectrum, this model is very helpful. But if studying the effect of spectrum is prime concern, then the model with approximate generation rate will be accurate enough to use. To clear this point, the hole concentration of an ultra-shallow emitter (0.1μm) is presented in fig. 5.28. This figure is obtained by summing over the individual frequency concentration in AM1.5G solar spectrum. It is clear that the general solution with actual G(x) and the approximated analytical solution actually overlap on one another. Hence, both solutions (in section 3.1 and in section 3.8) can be used without introducing any significant errors in the carrier concentration. The ATLAS device simulator data is also presented in fig. 5.28.

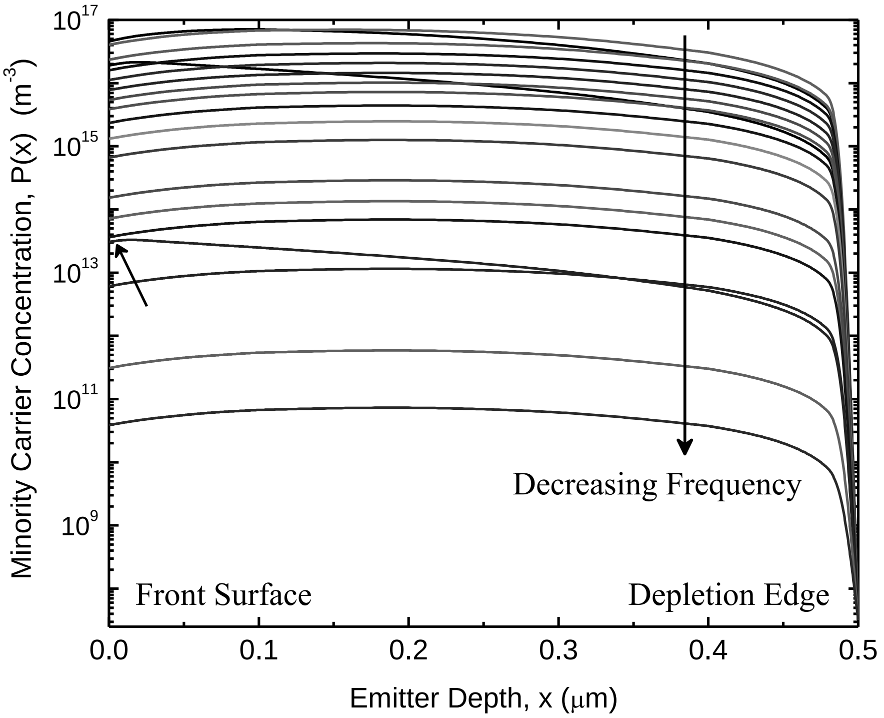

Fig 5.28. The contribution from individual wavelength on a 0.5 μm emitter. SRV is 5 × 10^4cm/s. The wavelength of incident light is varied from 0.3μm to 1.2μm.

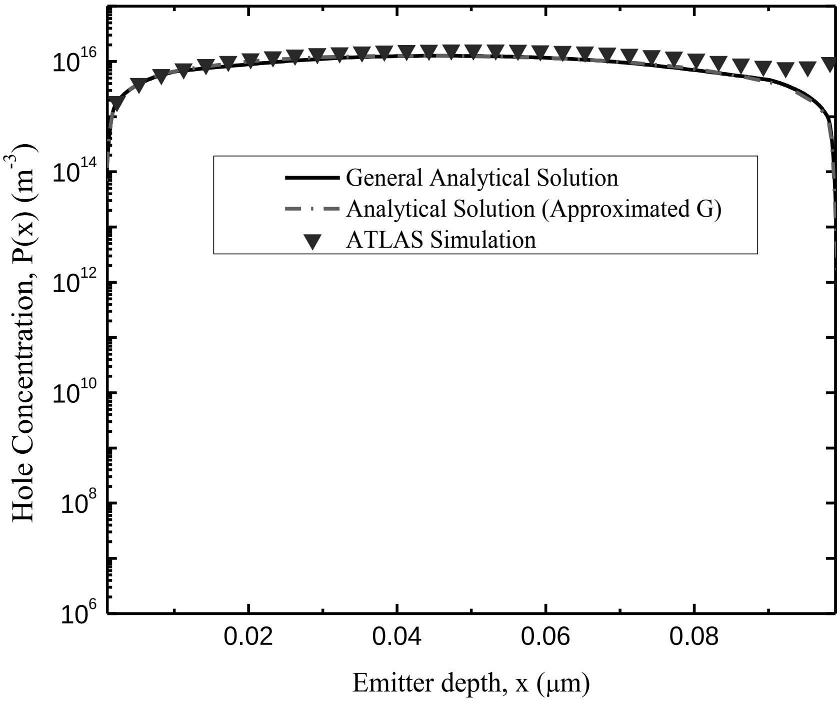

Fig 5.29. General analytical solution for a 0.1 μm emitter with very high SRV (5 × 10^6 cm/s) and no bias is applied. AM1.5 spectrum in the range of 0.3μm to 1.2μm is incident on the cell. BGN factor, f=0.

5.8. Simplification of the Analytical model

The main drawback of this model is the mathematical complexity that may limit its applicability in getting a quick estimate for optimization purpose. Although this model can include many effects simultaneously with the added cost of complexity, it will serve better purpose if the expression is much less complex and more straightforward. A simple look at the expression of hole concentration (or, electron concentration) shows that one particular function is making it complex to interpret. That is the Hypergeometric function, ${}_1F_2$. To achieve a simplified version of equation (3.19), several mathematical approximations will be explored in this section to deal with these advanced functions.

The theoretical details of Hypergeometric functions are discussed briefly in the appendix C. The two Hypergeometric functions, used in the derivation, are defined as follows –

$$\text{Hypergeometric function 1} = H_1(z) = {}_1F_2\left(\frac{\gamma-\nu}{2};-\nu+1,\frac{\gamma-\nu+2}{2};\frac{\beta^2 z^2}{4}\right) \quad (5.5)$$

$$\text{Hypergeometric function 2} = H_2(z) = {}_1F_2\left(\frac{\gamma+\nu}{2};+\nu+1,\frac{\gamma+\nu+2}{2};\frac{\beta^2 z^2}{4}\right) \quad (5.6)$$

For thin emitters ($X_j \leq 0.5$ µm), it is observed that the variation of Hypergeometric function is confined to 1.0~1.15 for each component of the generation terms (corresponds to each a_i and b_i). Since thin emitter is common for practical cells, taking Hypergeometric function to be 1 is a valid assumption for typical solar cells. As evident from the fig. 5.29 below, the Hypergeometric function shows maximum value at the front surface (at x=0) and for the first component of the generation term (a_1 and b_1).

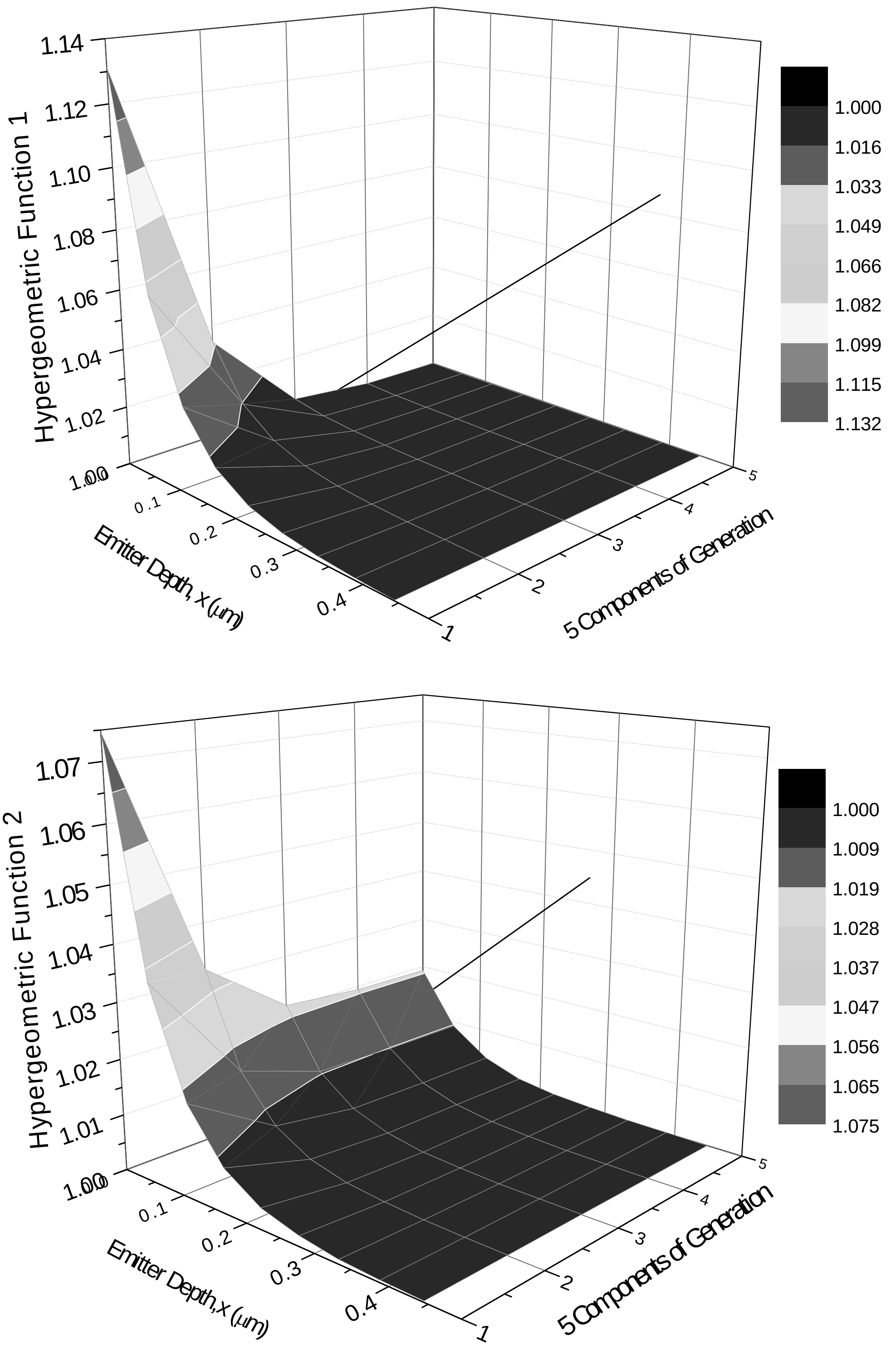

Fig 5.30. Variation of Hypergeometric terms $_1F_2$ (z) in the generation expression of minority carrier concentration. For each of 5 components of approximated carrier generation G, the maximum value of Hypergeometric function is limited to 1.

Replacing the Hypergeometric function with 1 will make the expression of carrier concentration much simpler, as presented below –

$$P(z) = \underbrace{C_1\ z^A I_\nu(\beta z) + C_2\ z^A I_{-\nu}(\beta z)}_{\text{Dark Component}}$$

$$\underbrace{-\sum_{i=1}^{5} \frac{E_i \pi}{2\sin(\pi\nu)} \times z^A \left[I_\nu(\beta z) \frac{2^\nu (\beta z)^{\gamma-\nu}}{(\gamma-\nu)\Gamma(-\nu+1)} - I_{-\nu}(\beta z) \frac{2^{-\nu} (\beta z)^{\gamma+\nu}}{(\gamma+\nu)\Gamma(\nu+1)} \right]}_{\text{Illumination Component}}$$

To compare this above simplified solution with the full expression, same thin emitter is taken into consideration. From fig. 5.30, it can be observed that the approximation can predict the actual expression correctly over most of the device, but it overestimates the concentration near the front surface. This can be easily explained from previous fig. 5.29. Since both the Hypergeometric functions gradually exceed 1.0 near the front surface, it is expected the approximation will introduce more error at x=0.

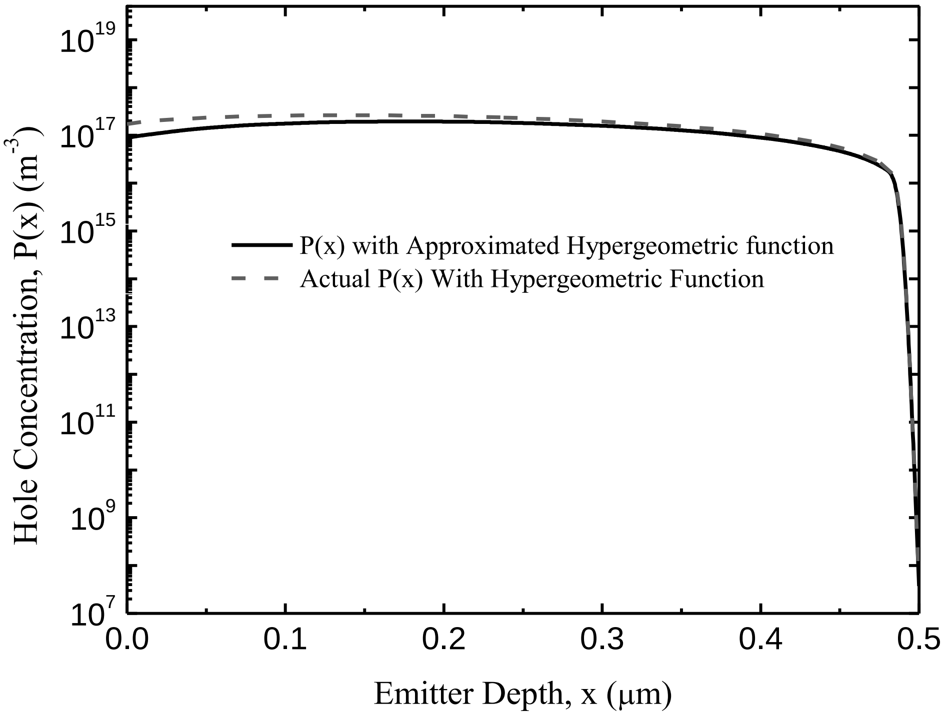

Fig 5.31. Comparison of minority carrier profile between actual P(x) where Hypergeometric terms $_1F_2$ exists in expression (3.19) and approximated P(x) where Hypergeometric terms $_1F_2$ is assumed to be zero. Device Dimensions: 0.5μm thick emitter; Surface Recombination Velocity = 5 × 10^4 cm/s; Bias, V = 0.

To observe how this simplification affects the total current density (and their constituting components), fig. 5.31 calculates current density for both cases. It is promising that the current density has very good match all over the device. The drift current density is same before and after the approximations. This is obvious since drift component does not contain any Hypergeometric terms. The diffusion current component has slight mismatch near the front surface. The reason for this expected difference just has been explained. The matched values obtained for total current density with and without approximation conclude that the simplification can describe the device current accurately enough and without the need for calculating the complex Hypergeometric function. To understand how close the match is between them, the absolute error between the cases is calculated, as illustrated in fig. 5.32. It is seen that the maximum error in total current density is only 3.05%, which is acceptable. Besides, the error is maximum only at surface, but zero for almost rest of the device. Since for obtaining the current-voltage characteristics of solar cell, traditionally the current at junction-edge ($x=x_j$) is taken into account. Hence, instead of actual current density in equation (3.53)-(3.54), the approximated J_{Total} can be used to describe the J-V characteristics without introducing any error at all. This is obviously a useful finding towards our attempt of reducing mathematical complexity.

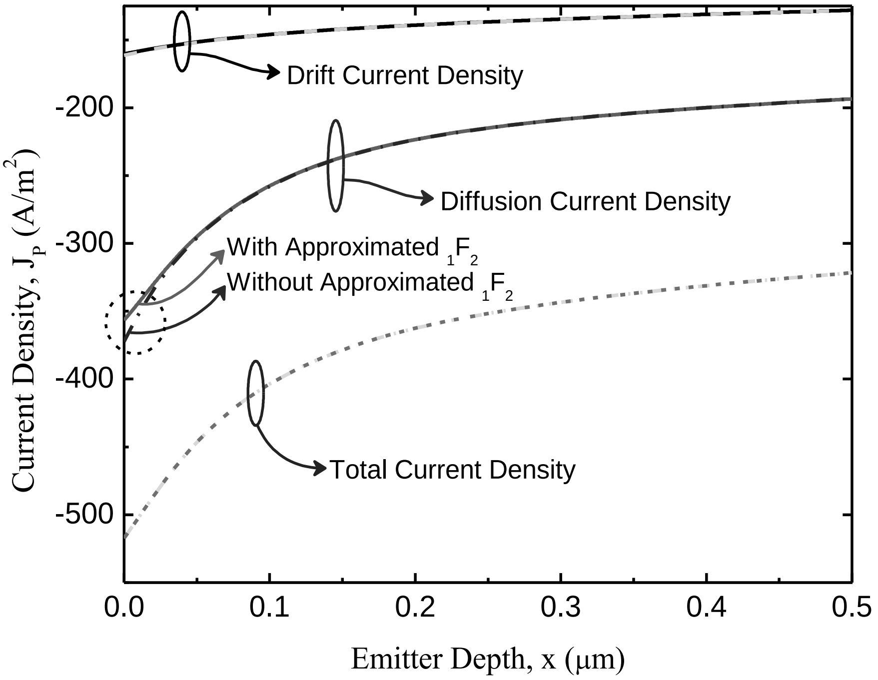

Fig 5.32. The effect of approximating Hypergeometric function on minority carrier current density and their components. Solid lines represent approximated Hypergeometric function and dotted line indicates current from actual expression.

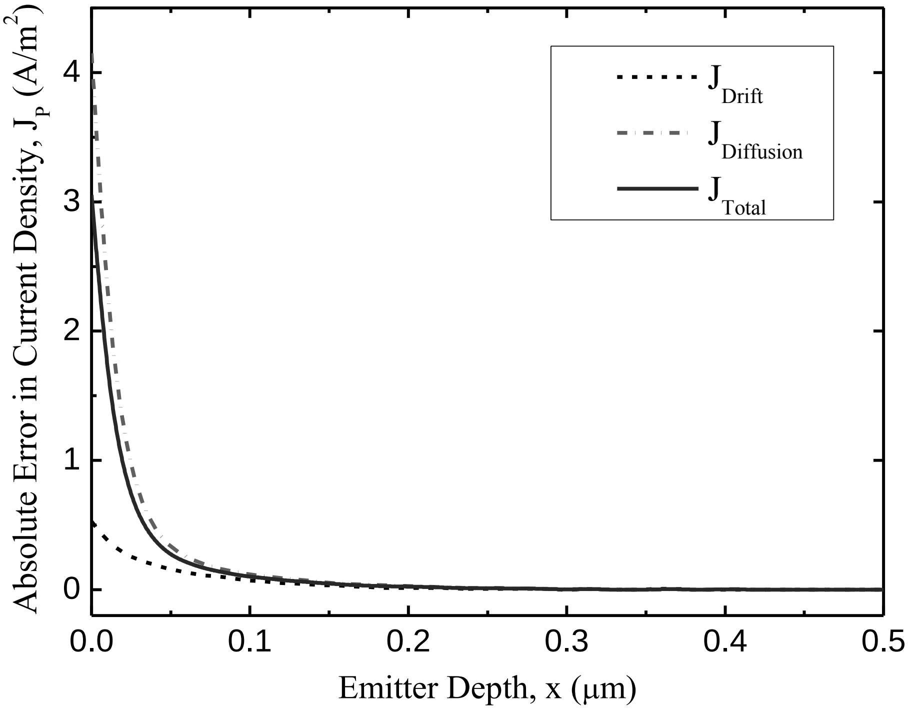

Fig 5.33. Absolute error of minority carrier current density and their components. The error analysis is for comparing the effect of approximation in Hypergeometric function.

The validity range of applying this approximated Hypergeometric function is the next obvious question. As seen from the illustration in fig. 5.33, the value of $_1F_2$ increases too fast when emitter is not shallow. For a 2 μm emitter, the value of Hypergeometric function at the top surface exceeds 2×10^5. For such high values, replacing Hypergeometric function with 1 will certainly introduce huge error. Hence for thick emitters, there is no alternative but to use the original solution.

It has been found that the simplified solution will work for emitter having thickness less than 0.5 μm. After that, complete solution of section 3.1 should be used. Figure 5.34 shows this limit.

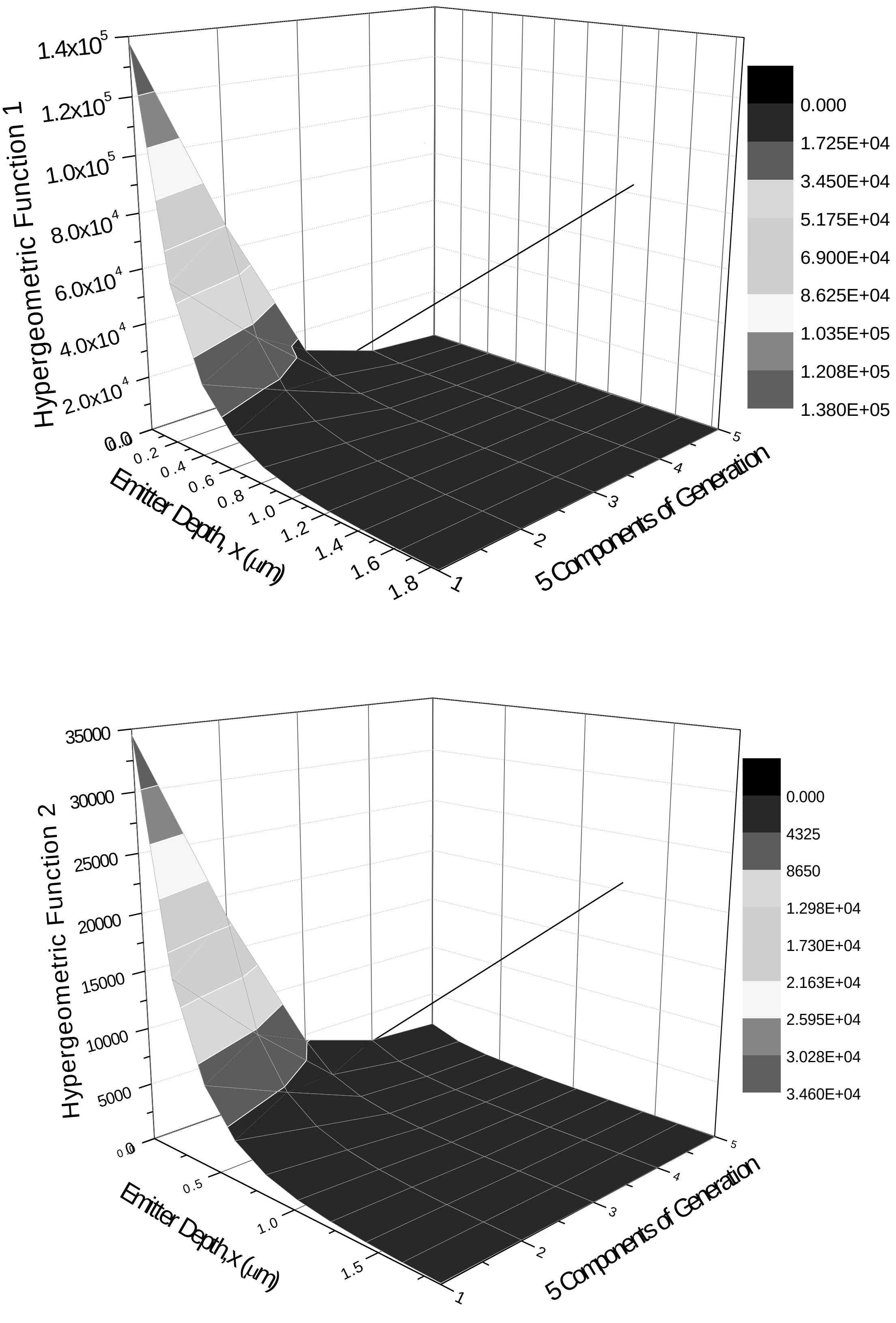

Fig 5.34. Variation of Hypergeometric terms $_1F_2$ (z) for a thick emitter (10μm)

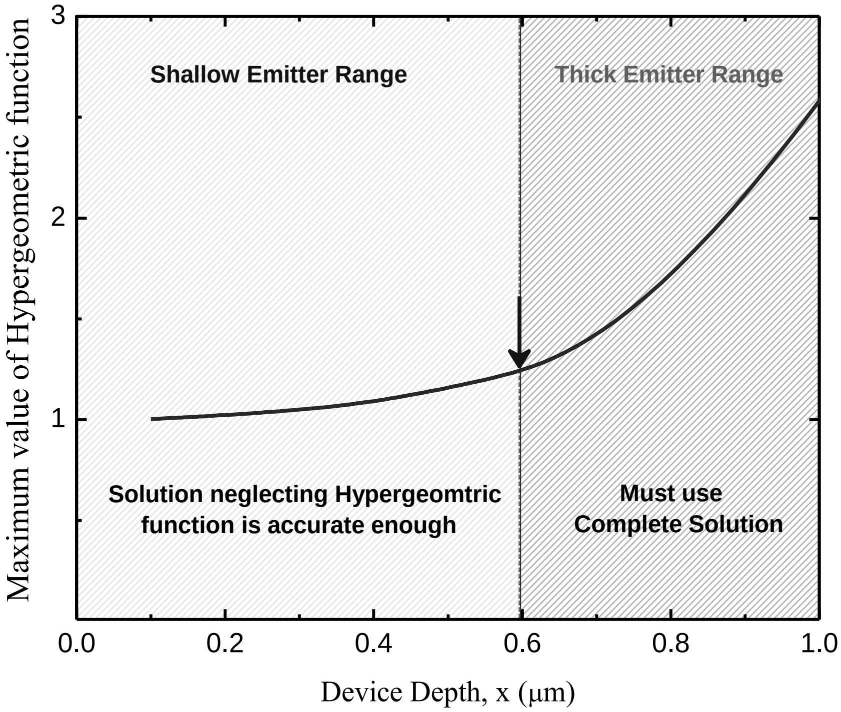

Fig 5.35. Variation of Hypergeometric terms $_1F_2$ (z) with device thickness. The arrow indicates after which thickness the approximation in Hypergeometric function will gradually become erroneous and complete solution should be used.

5.9. Convergence Issues of Hypergeometric Function

It is necessary to look at one property of Hypergeometric function more closely. The convergence of Hypergeometric function needs to be considered. Standard convergence technique dictates that the last argument of $_1F_2$ has to obey the following criterion –

$$\left|\frac{\beta^2 z^2}{4}\right| < 1$$

Making use of (3.13) in the above condition results in –

$$\underbrace{\left(\frac{{N_{d0}}^{m+k}}{KMV_T\alpha^2(m+k)^2}\right)}_{\text{Constant}} \times \underbrace{\left|\exp^{-\alpha(m+k)x}\right|}_{\text{Gradually Decreasing Term}} < 1 \qquad (5.7)$$

This criterion is an important relation that needs further attention. The first term is a constant which depends on peak doping (N_{d0}), doping gradient constant (α) and, lifetime and mobility constants (m, M, k, K). The second term is an exponentially decreasing term that has maximum value (1) at the surface (x=0). So the second term is actually helping in satisfying the abovementioned condition as x increases along the depth of the device. Hence if the condition is met at the front surface, it will certainly be valid for the rest of the region. The criterion then effectively reduces as follows,

$$\left(\frac{{N_{d0}}^{m+k}}{KMV_T\alpha^2(m+k)^2} \right) < 1 \tag{5.8}$$

Typical values of N_{d0} is 10^{20} cm^{-3} is quite common. The maximum values for K, k, M, m are 5.5×10^{30}cm^{-6}/s, 2, 1.4×10^{9} cm$^{0.86}$V^{-1}s^{-1} and m = 0.38 respectively. α depends on the peak doping and junction doping. The left side of the condition is checked in fig 5.25 below for several emitter thickness and different junction doping, N_d (at x=X_j). The fig. reveals a notable sitation of hypergeometric convergence. The shaded portion is the allowed region where hypergeometric function will converge for all values of x. If the junction doping is high (e.g. 6×10^{18}cm^{-3}), then the solution will converge upto 1.47µm thick emitter. On the other hand, for low junction doping like 10^{16} cm^{-3} (which means doping varies widely from 10^{20} cm^{-3} to 10^{16} cm^{-3}), the condition is valid upto 5µm emitters. The curve below can also be described from the viewpoint of doping gradient α. It is evident from fig. 5.35 below, if the doping gradient is large (wide range of doping variation), then the solution will converge for thicker emitter too. On the contrary, if any uniform doping profile is approximated by exponential doping (with very small gradient α), this solution runs the risk of getting out of convergence region. Since for most of the practical thin-film emitters, thickness is near 0.5µm, the convergence is certainly ensured for most of the common solar cells.

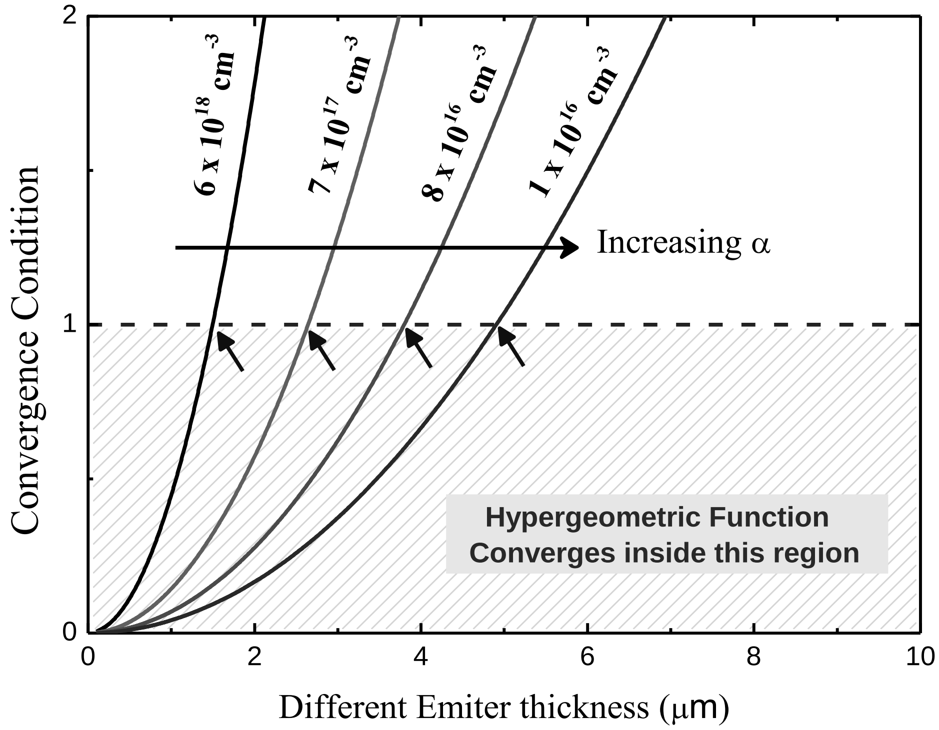

Fig 5.36. The convergence region of Hypergeometric function over several emitter thickness for various doping concentration and doping profiles

5.10. Comparison With Previous Models

The model is compared with the previous work [8] of solar cell. The analytical model of Verhoef *et al.* [8] has been derived for dark conditions only. Since our model becomes a dark current model when illumination term P_3 is 0 (as only dark response remains), the results from this model should match with Dark current model of [8].

As evident from fig. 5.36, good agreement for $P_1(x)$ component is observed. But there is slight mismatch in 2nd term of Complementary function, $P_2(x)$. This mismatch in P_2 can be explained using the theory of Bessel function [61]. As evident from the theory behind *Bessel's modified equation* [62], both (I_ν, $I_{-\nu}$) and (I_ν, K_ν) are valid solutions of 2nd order differential equations (for details, see Appendix B: Section B.2). When ν is a non-integer (like in our case), they represent independent set of solutions. K_ν and $I_{-\nu}$ are related by the following identity [63]:

$$K_\nu(x) = \frac{\pi}{2}\left(\frac{I_{-\nu}(x) - I_\nu(x)}{\sin(\pi\nu)}\right) \tag{5.9}$$

In this work, we have used the 1st set of independent solution (namely, I_v & I_{-v}), where the 2nd set (namely, I_v & K_v) is used in [8]. Hence, according to equation (5.9), there is an expected deviation when plotting the parts of solutions, since I_{-v} and K_v are related but not same function. If one complete device is solved for same boundary conditions (with C_1 and C_2 calculated from BCs), both sets of solution (I_v, I_{-v} or, I_v, K_v) will give same result.

To demonstrate the validity of this argument, we can take a simple p-n junction under dark condition and exact same boundary conditions. The doping is varied exponentially from 10^{20} cm^{-3} to 6×10^{18} cm^{-3} for both models. As seen in fig. 5.37, the dark-response part of our solution in equation (3.19), matches perfectly with dark model in [8].

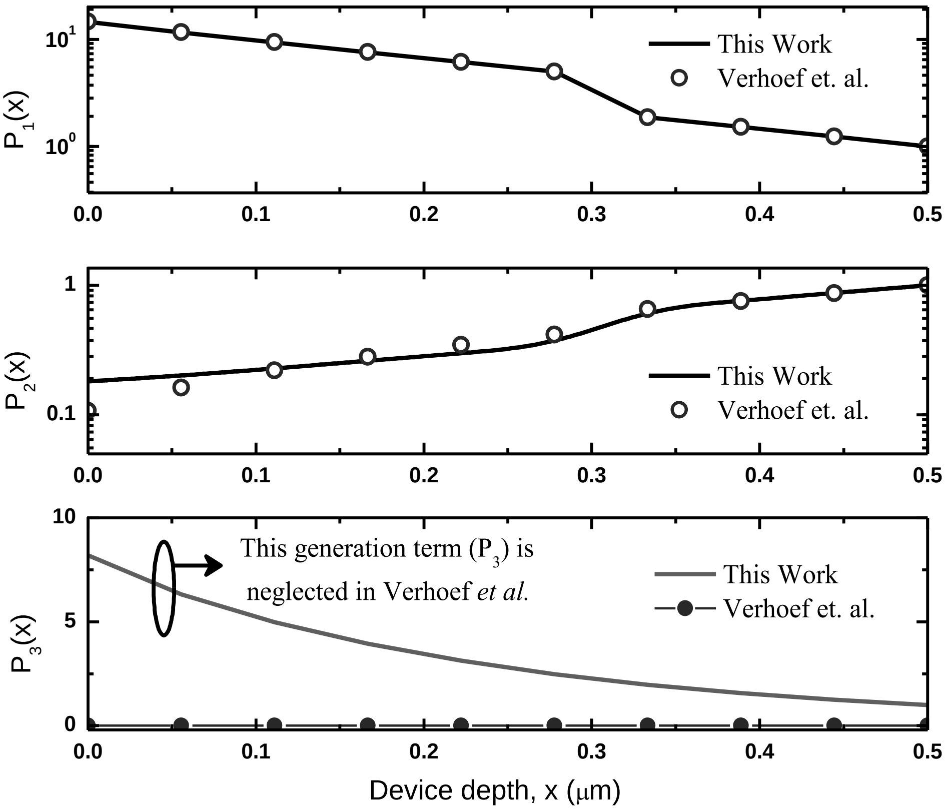

Fig 5.37. Comparison of our solution with that of [8] **(a)** $P_1(x)$ normalized to $P_1(W)$, **(b)** $P_2(x)$, normalized to $P_2(W)$ and **(c)** $P_3(x)$, normalized to $P_3(W)$, P_3 term is completely neglected in [8].

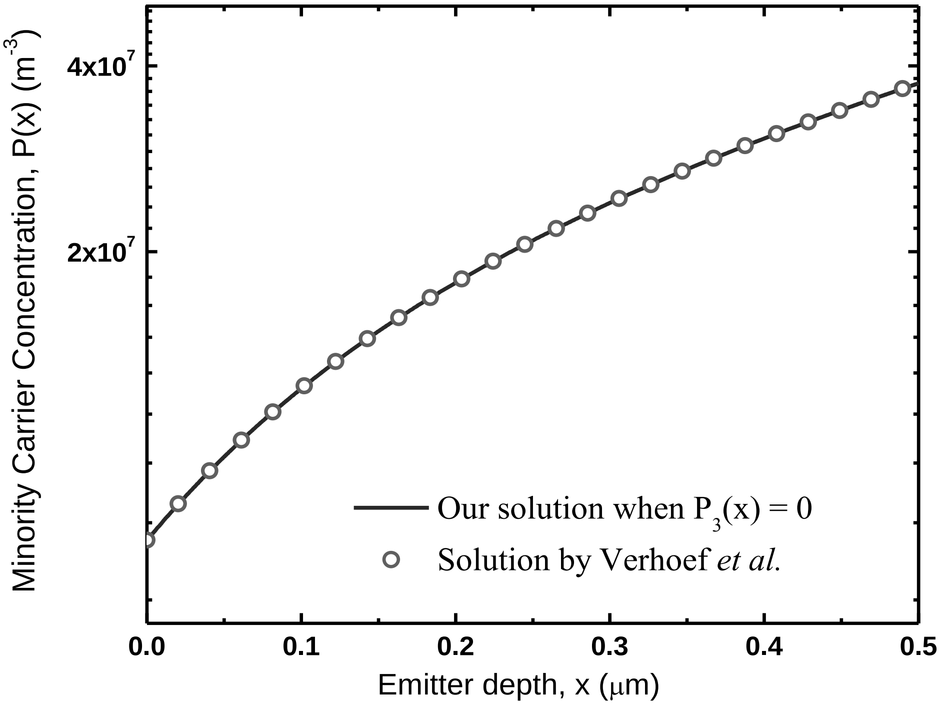

Fig 5.38. Comparison of our solution under dark condition with [8]: The light is incident on 0.5μm emitter. The front surface is characterized by recombination velocity of 5×10^4 cm/s. The hole conc. at the junction is given by (n_i^2/N_D).

5.11. Summary

This chapter presents a detailed analysis of the analytical model developed in chapter 3. After rigorously testing the proposed model for several devices, the model is established firmly for wide variations of device parameters. The numerical solar cell models in ATLAS and COMSOL Multiphysics have been used to verify whether our model can predict the effect of all the parameter changes. Moreover, the comparison with existing literature has shown good agreement with our model. In short, the range, validity, robustness, limitation, success and expansions of the proposed model are explored and confirmed in this chapter.

CHAPTER 6

CONCLUSIONS

6.1. Discussions and Conclusion

A complete analytical model for single-junction solar cell has been presented in this thesis. This model presents a unique relationship of carrier concentration with the transport physics and incident spectrum. The solution technique is based on empirical expression of lifetime and mobility. The initial solution is constructed on the approximation of carrier generation rate, which can offer quite accurate result of solar cell under actual solar spectrum. Nonetheless, the solution is further expanded to a more general level with actual carrier generation. Along with that, the model is also expandable to other photovoltaic materials and other arbitrary spectrums.

It is found from the analysis that the derived model can explain the minority carrier (both electron and hole) concentration. To verify the mathematical approaches, two numerical models have been developed in this thesis. A COMSOL Multiphysics equation-based model is constructed using the Finite Element Method (FEM). Good agreement with the COMSOL model has ensured that our analytical solution is mathematically correct. Another renowned device simulator (TCAD) Silvaco/ATLAS is also used to test the validity of the proposed model. Concentration-dependent parameters (mobility, SRH etc.), Heavy doping effects (like BGN, Fermi-Dirac Statistics) are included on the TCAD solar cell model. It is observed that our analytical solution is in good agreement with ATLAS simulation. There is slight mismatch with the TCAD solution which can be attributed to the error in empirical expression of lifetime and mobility. From both mathematical and TCAD point of view, it is concluded that the solution is very robust.

The solution has been tested for several surface conditions. For wide variation of surface recombination velocity, it is found that the model is very successful in predicting the trend of carrier concentration. The effect of BGN is also investigated using this model. BGN increases the carrier concentration, but the increase is not that significant.

The compact expression of current density is derived and also examined carefully. From these equations, the individual contributions of the drift and diffusion current, as well as the illumination and dark current components are studied both separately and simultaneously. Comparing the current density with TCAD models gives satisfactory match.

One of the strength of our model is its ability to predict the optical behavior under actual solar spectrum. Since the solution has the provision to add any spectrum by using the approximated generation rate, the effect of AM1.5G and AM1.5D spectrum is observed. It is seen that the spectrum has very little effect on carrier concentration because they are almost-identical terrestrial spectrum. The approximation taken for carrier generation is tested also. When compared to the ATLAS model, it is found that the traditional values for the approximation coefficients are not fitted closely. Hence, as a detour, a new set of approximated generation rate is proposed and good matching is obtained for the carrier concentration.

The effect of biasing on the carrier concentration and current density is also investigated. Along with that, the J-V curve and power density characteristics are calculated. It is observed that this compact model is very good in calculating the key parameters of solar cells (e.g. efficiency, FF, V_{OC}, I_{SC}, and so on).

The effect of Emitter depth is tested on five different emitters for two possible scenarios. For all cases, the minority carrier concentration remains constant at the boundary due to fixed SRV and biasing, and the concentration at the middle just spreads over the device. Similar spreading is observed for the current density profile.

One major limitation of our model is the approximated generation rate. Hence, attempt is taken to overcome this limitation and a more general model is proposed that makes use of individual contributions of the solar spectrum. It includes the photon absorption and photon intensity in the final expression. From the analysis of the general solution, it is found that this solution gives slightly accurate result when compared to the previous solution of approximated generation rate. Hence, the later solution will suffice for most of the practical cases. But if monochromatic light source is incident on the solar cell or the effect of certain frequency band is of interest, then the former general solution has no alternative.

The solution, albeit its success, is complex in nature. The complexity arises from the Hypergeometric function. Therefore, another simple solution, derived from the previous general solution, has been proposed. This approach depends on the mathematical simplification of Hypergeometric function by replacing it with a constant value. Detailed analysis shows that the simplified solution shows maximum 3% error for swallow emitters, but gives unacceptable errors when thick emitters are used. An acceptable thickness range is specified beyond which this approximated solution should not be used.

The convergence criterion of the Hypergeometric function is also explored for the completeness of the thesis. A relationship with doping and width is established after which the Hypergeometric function becomes too large to compute.

Although the proposed model has been compared with COMSOL and ATLAS a lot of times, the model is also tested with existing analytical model in the literature. When the incident spectrum is turned off, this model has shown excellent match with the dark current models proposed by previous authors.

6.2. Suggestion for future Work

The mathematical model of this thesis has very rich potential. This analytical model will ensure better optimization of solar cell dimensions and make the study of calculating the individual contributions easier. Some suggestions for the future developments are –

- The model is easily expandable to power-law doping profile. To incorporate this type of arbitrary doping profile, exponential-approximated doping profile can be used.

- The model can be used for new photovoltaic materials (Other than those already mentioned here). Simply tailoring the transport constants K, k, M, m will make this model as invaluable tool to study the possibility of using different materials as solar cell.

- Although this model is developed for common solar cells, the same modeling approach can be employed for p-i-n and CIGS (Copper Indium Gallium Selenide) solar cell. The techniques and mathematics used in this thesis will be helpful in deriving the compact models for these solar cells too.

- Effect of series and shunt resistance is not included in this study. Their effects can be added to the general expression to predict the deterioration in performance caused by them.

- Effect of surface texturing is another factor that can increase the applicability of this model to more complex surface geometry. The existing numerical and semi-analytical models of textured solar cell can be extended using the mathematical methods used for this work.

In future, these extensions and upgrades will be explored and analyzed. That will be the focus of our future publications.

REFERENCES

[1] Hamel, J. S., "Simplified analytical quasi-transparent solution for minority carrier transport in non-uniformly doped quasi-neutral semiconductor regions," *Electron Devices, IEEE Transactions on,* vol. 43, pp. 104-109, 1996.

[2] Daliento, S. and Mele, L., "Approximate Closed-Form Analytical Solution for Minority Carrier Transport in Opaque Heavily Doped Regions Under Illuminated Conditions," *Electron Devices, IEEE Transactions on,* vol. 53, pp. 2837-2839, 2006.

[3] Burgers, A. R., Leguijt, C., Lolgen, P., and Sinke, W. C., "New analytical expressions for dark current calculations of highly doped regions in semiconductor devices," *Electron Devices, IEEE Transactions on,* vol. 44, pp. 171-179, 1997.

[4] Cuevas, A. and Balbuena, M. A., "Review of analytical models for the study of highly doped regions of silicon devices," *Electron Devices, IEEE Transactions on,* vol. 36, pp. 553-560, 1989.

[5] Cuevas, A. and Rinaldi, N., "Comment on modeling of minority-carrier transport in nonuniformly doped silicon regions with asymptotic expansions [with reply]," *Electron Devices, IEEE Transactions on,* vol. 42, pp. 1200-1202, 1995.

[6] Bisschop, F. J., Verhoef, L. A., and Sinke, W. C., "An analytical solution for the collection efficiency of solar-cell emitters with arbitrary doping profile," *Electron Devices, IEEE Transactions on,* vol. 37, pp. 358-364, 1990.

[7] Rinaldi, N., "Modeling of minority-carrier transport in nonuniformly doped silicon regions with asymptotic expansions," *Electron Devices, IEEE Transactions on,* vol. 40, pp. 2307-2317, 1993.

[8] Verhoef, L. A. and Sinke, W. C., "Minority-carrier transport in nonuniformly doped silicon-an analytical approach," *Electron Devices, IEEE Transactions on,* vol. 37, pp. 210-221, 1990.

[9] Daliento, S., Mele, L., Bobeico, E., Lancellotti, L., and Morvillo, P., "Analytical modelling and minority current measurements for the determination of the emitter surface recombination velocity in silicon solar cells," *Solar Energy Materials and Solar Cells,* vol. 91, pp. 707-713, 5/4/ 2007.

[10] Selvakumar, C. R., "Simple general analytical solution to the minority carrier transport in heavily doped semiconductors," *Journal of Applied Physics,* vol. 56, pp. 3476-3478, 1984.

[11] del Alamo, J. A. and Swanson, R. M., "The physics and modeling of heavily doped emitters," *Electron Devices, IEEE Transactions on,* vol. 31, pp. 1878-1888, 1984.

[12] Basore, P. A., Rover, D. T., and Smith, A. W., "PC-1D version 2: enhanced numerical solar cell modelling," in *Photovoltaic Specialists Conference, 1988., Conference Record of the Twentieth IEEE*, 1988, pp. 389-396 vol.1.

[13] Sanders, M. H., "Modeling of Operating Temperature Performance of Triple Junction Solar Cells Using Silvaco's Atlas," M. Sc. Thesis, Department of ECE, Naval Postgraduate School Monterey, CA, 2007.

[14] Crespin, A. L., "A novel approach to modeling the effects of radiation in Gallium-Arsenide solar cells using Silvaco's Atlas software," M. Sc. Thesis, Dept. of ECE, Naval Postgraduate School, Monterey, California, 2004.

[15] Park, J., x, Sik, Neugroschel, A., and Lindholm, F. A., "Systematic analytical solutions for minority-carrier transport in semiconductors with position-dependent composition, with application to heavily doped silicon," *Electron Devices, IEEE Transactions on,* vol. 33, pp. 240-249, 1986.

[16] Mertens, R. P., de Man, H. J., and M., v. O. R., "Calculation of the emitter efficiency of bipolar transistors," *IEEE Transaction on Electron Devices, IEEE Transactions on,* vol. ED-20, p. 7, 1973.

[17] Kuzmicz, W., "Modeling of minority carrier current in heavily doped regions of bipolar transistor," *IEEE Trans. Computer-Aided Design,* vol. CAD-5, pp. 204-214, 1986.

[18] Michael, S., Bates, A. D., and Green, M. S., "Silvaco ATLAS as a solar cell modeling tool," in *Photovoltaic Specialists Conference, 2005. Conference Record of the Thirty-first IEEE*, 2005, pp. 719-721.

[19] VanDyke, J. E., "Modeling laser effects on multi-junction solar cells using Silvaco ATLAS software for spacecraft power beaming applications," DTIC Document, 2010.

[20] Gelinas, R., "A Novel Approach Tomodeling Tunnel Junction Diodes Using Silvaco Atlas Software," M. Sc. thesis, Dept. of ECE, Naval Postgraduate School, Monterey, California, 2005.

[21] Baldomero Garcia, J., "Indium Gallium Nitride Multijunction Solar Cell Simulation Using Silvaco Atlas," M. Sc. Thesis, Dept. of ECE, Naval Postgraduate School, Monterey, California 2007.

[22] Sproul, A. B. and Green, M. A., "Parameters of laser grooved silicon solar cells determined from matching theoretical and experimental results," *Proc. 4th Int. Photovolt. Sci. Eng. Conf. (Sydney, Australia)* 1989.

[23] Dumke, W. P., "Minority camer injection and storage into a heavily doped emitter," *Solid-State Electron.,* vol. 24, p. 3, 1981.

[24] Amantea, R., "A new solution for minority-carrier injection into the emitter of a bipolar transistor," *IEEE Trans. Electron Devices,* vol. ED-27, p. 8, 1980.

[25] Selvakumar, C. R. and Roulston, D. J., "A new simple analytical emitter model for bipolar transistors," *Solid-state Electron.,* vol. 30, p. 3, 1987.

[26] de Graaff, H. C., Slotboom, J. W., and Schmitz, A., "The emitter efficiency of bipolar transistors: Theory and experiments," *Solid-State Electronics,* vol. 20, pp. 515-521, // 1977.

[27] Lampert, M. A. and Schilling, R. B., *Current injection in solids: The regional approximation method* vol. 6: New York: Academic Press, 1970.

[28] Shibib, M. A., Lindholm, F. A., and Therez, F., "Heavily doped transparent emitter regions in junction solar cells, diodes, and transistors," *IEEE Trans. Electron Devices.,* vol. ED-26, p. 7, 1979.

[29] van Overstraeten, R. J. and Mertens, R. P., "Heavy doping effects in silicon," *Solid-State Electron.,* vol. 30, p. 21, 1987.

[30] Alcubilla, R. and Pons, J., "The impurity dose, a useful parameter for emitter design," *Solid-state Electron.,* vol. 34, p. 5, 1991.

[31] Fossum, J. G. and Lee, D. S., "A physical model for the dependence of carrier lifetime on doping density in nondegenerate silicon," *Solid-State Electronics,* vol. 25, pp. 741-747, 8// 1982.

[32] Fossum, J. G. and Shibib, M. A., "An analytic model for minority-carrier transport in heavily doped regions of silicon devices," *Electron Devices, IEEE Transactions on,* vol. 28, pp. 1018-1025, 1981.

[33] Kleefstra, M., "A simple method of calculating the minority-carrier current in heavily doped silicon," *Solid-State Electron.,* vol. 28, p. 6, 1985.

[34] de Man, H. J., "The influence of heavy doping on the emitter efficiencv of a bipolar transistor," *IEEE Trans. Electron Devices.,* vol. ED-18, p. 3, 1971.

[35] Prince, M. B. and Wolf, M., "New developments in silicon photovoltaic devices," *Radio Engineers, Journal of the British Institution of,* vol. 18, pp. 583-594, 1958.

[36] Wolf, M., "Drift fields in photovoltaic solar energy converter cells," *Proceedings of the IEEE,* vol. 51, pp. 674-693, 1963.

[37] Wolf, M., "Limitations and Possibilities for Improvement of Photovoltaic Solar Energy Converters: Part I: Considerations for Earth's Surface Operation," *Proceedings of the IRE,* vol. 48, pp. 1246-1263, 1960.

[38] Cuevas, A., Merchan, R., and Ramos, J. C., "On the systematic analytical solutions for minority-carrier transport in nonuniform doped semiconductors: application to solar cells," *Electron Devices, IEEE Transactions on,* vol. 40, pp. 1181-1183, 1993.

[39] Rinaldi, N., "Validity range estimate of the asymptotic expansion approach for the modeling of minority-carrier injection into heavily doped emitters," *Electron Devices, IEEE Transactions on,* vol. 42, pp. 1011-1013, 1995.

[40] Sheoran, M., "Developement of high-efficiencysolar cells on thin silicon through design optimization and defect passivation " Ph. D. Thesis, Georgia Institute of Technology 2009

[41] Fonash, S. J., *Solar Cell Device Physics*: Academic Press, 2010.

[42] Schumacher, J. O., "Numerical simulation of Silicon cells with novel cell structure," PhD thesis, Fraunhofer-Institut für, 2000.

[43] Sze, S. M. and Ng, K. K., *Physics of Semiconductor Devices*, Third ed.: John Wiley & Sons, 2006.

[44] Neamen, D. A., *Semiconductor Physics And Devices*, 3rd ed. ed.: Tata McGraw-Hill Edition, 2002.

[45] Deceglie, M. G., "Advanced Silicon Solar Cell Device Physics and Design," Ph.D California Institute of Technology, Pasadena, California, 2013.

[46] Moon, P., "Proposed standard solar-radiation curves for engineering use," *Journal of the Franklin Institute,* vol. 230, pp. 583-617, 11// 1940.

[47] *ATLAS User's Manual*. SILVACO, Inc., Santa Clara, CA, 2010.

[48] Klaassen, D. B. M., "A unified mobility model for device simulation—I. Model equations and concentration dependence," *Solid-State Electronics,* vol. 35, pp. 953-959, 7// 1992.

[49] Stem, N. and Cid, M., "Studies of phosphorus Gaussian profile emitter silicon solar cells," *Materials Research,* vol. 4, pp. 143-148, 2001.

[50] Burk, D. E. and De La Torre, V., "An empirical fit to minority hole mobilities," *Electron Device Letters, IEEE,* vol. 5, pp. 231-233, 1984.

[51] Renshaw, J. S., "Numerical Modeling and Fabrication Of High Efficiency Crystalline Silicon Solar Cells," School of Physics, Georgia Institute of Technology, Georgia, 2013.

[52] Green, M. A., "Limits on the open-circuit voltage and efficiency of silicon solar cells imposed by intrinsic Auger processes," *Electron Devices, IEEE Transactions on,* vol. 31, pp. 671-678, 1984.

[53] del Alamo, J., Swirhun, S., and Swanson, R. M., "Measuring and modeling minority carrier transport in heavily doped silicon," *Solid-State Electronics,* vol. 28, pp. 47-54, 1985.

[54] Shockley, W. and Queisser, H. J., "Detailed Balance Limit of Efficiency of p-n Junction Solar Cells," *Journal of Applied Physics,* vol. 32, pp. 510-519, 1961.

[55] Rinaldi, N. F., "Modeling of small-signal minority-carrier transport in bipolar devices at arbitrary injection levels," *Electron Devices, IEEE Transactions on,* vol. 45, pp. 1501-1510, 1998.

[56] Michael, S. and Michalopoulos, P., "Application of the SILVACO/ATLAS software package in modeling and optimization of state-of-the-art photovoltaic devices," in *Circuits and Systems, 2002. MWSCAS-2002. The 2002 45th Midwest Symposium on*, 2002, pp. 651-654.

[57] Furlan, J. and Amon, S., "Approximation of the carrier generation rate in illuminated silicon," *Solid-State Electronics,* vol. 28, pp. 1241-1243, 1985.

[58] Hsieh, H. C., Hu, C., and Drowley, C. I., "A new method of analyzing the short-circuit current of silicon solar cells," *Electron Devices, IEEE Transactions on,* vol. 27, pp. 883-885, 1980.

[59] Chowdhury, M. M. and Debnath, B., "Approximation of carrier generation rate in common solar cells and studies for optimization of n+p silicon solar cell for AM1.5G and AM1.5D," in *7th International Conference of Electrical & Computer Engineering (ICECE)*, 2012, pp. 327-330.

[60] Rinaldi, N., "Modeling and optimization of shallow and opaque heavily doped emitters for bipolar devices," *Electron Devices, IEEE Transactions on,* vol. 42, pp. 1126-1133, 1995.

[61] Bell, W. W., *Special Functions for Scientists and Engineers*: Dover Publication, 2004.

[62] Korenev, B. G., *Bessel Function and their Application*, 2002.

[63] Lebedev, N. N., *Special functions and their applications*: PRENTICE-HALL,INC., 1965.

[64] Mousty, F., Ostoja, P., and Passari, L., "Relationship between resistivity and phosphorus concentration in silicon," *Journal of Applied Physics,* vol. 45, pp. 4576-4580, 1974.

[65] Rajkanan, K., Singh, R., and Shewchun, J., "Absorption coefficient of silicon for solar cell calculations," *Solid-State Electronics,* vol. 22, pp. 793-795, 9// 1979.

[66] *Reference Solar Spectral Irradiance: Air Mass 1.5*. Available: rredc.nrel.gov/solar/spectra/am1.5/

[67] Guoxin, L., Neugroschel, A., Sah, R. L. Y., Hemmenway, D., Rivoli, T., and Maddux, J., "Analysis of bipolar junction transistors with a Gaussian base-dopant impurity-concentration profile," *Electron Devices, IEEE Transactions on,* vol. 48, pp. 2945-2947, 2001.

[68] Garfrerick, A. R., "Modeling Heterogeneous Carbon Nanotube Networks For Photovoltaic Applications Using Silvaco Atlas Software," M. Sc. Thesis, Dept. of ECE, Naval Postgraduate School, Monterey, California, 2012.

[69] Michalopoulos, P., "A novel approach for the development and optimization of state-of-the-art photovoltaic devices using Silvaco," M. Sc. Thesis, Department of ECE, Naval Postgraduate School, Monterey, California, 2002.

[70] McCloy, D. J., "High Efficiency Solar Cells: A model in Silvaco," M. Sc. thesis, Department of Electrical and Computer Engineering, Naval Postgraduate School 1999.

[71] *http://www.comsol.com/*.

[72] *SOPRA Database*. Available: www.sopra-sa.com

[73] Slotboom, J. W., "The pn-product in silicon," *Solid-State Electronics,* vol. 20, pp. 279-283, 4// 1977.

[74] Slotboom, J. W. and de Graaff, H. C., "Measurements of bandgap narrowing in Si bipolar transistors," *Solid-State Electronics,* vol. 19, pp. 857-862, 10// 1976.

[75] *Comsol Multiphysics: User's Guide*: COMSOL Inc., 2011.

[76] Easwarakhanthan, T., Bottin, J., Bouhouch, I., and Boutrit, C., "Nonlinear Minimization Algorithm for Determining the Solar Cell Parameters with Microcomputers," *International Journal of Solar Energy,* vol. 4, pp. 1-12, 1986.

[77] Prince, M. B., "Silicon Solar Energy Converters," *Journal of Applied Physics,* vol. 26, pp. 534-540, 1955.

[78] Luke, Y. L., *The Special Functions and Their Approximations* vol. I: Academic Press, 1969.

[79] Pearson, J., "Computation of Hypergeometric Functions," M. Sc., Mathematical Modelling and Scientic Computing, University of Oxford, 2009.

[80] "Standard Solar Spectra."

[81] *American Society for Testing and Materials* Available: http://www.astm.org/

[82] *ASTM Standard Reference Spectra* Available: http://www.astm.org/Standards/G173.htm

[83] *Solar Spectra: Air Mass Zero*. Available: http://rredc.nrel.gov/solar/spectra/am0/am0_index.html#spectrum

[84] *Global Horizontal Radiation*. Available: https://eosweb.larc.nasa.gov/cgi-bin/sse/global.cgi?

Appendix A

Detailed Mathematical Derivation

A.1 Calculating Particular Integral Containing Bessel Function

The reduced form of differential equation (see chapter 3) that is obtained after the mathematical manipulation of basic semiconductor differential equations.

$$z^2\frac{d^2u}{dz^2}+z\frac{du}{dz}-\left(\beta^2z^2+\nu^2\right)u=-\sum_{i=1}^{5}C_iz^{\gamma} \tag{A.1}$$

Solving the above equation is crucial in our thesis. The homogeneous counterpart of equation (A.1) is –

$$z^2\frac{d^2u}{dz^2}+z\frac{du}{dz}-\left(\beta^2z^2+\nu^2\right)u=0$$

The solution of the above homogeneous part $u_h(z)$ is easy to derive (see Chapter 3 and appendix B).

$$\mathrm{u_h}\left(\mathrm{z}\right)=C_1I_\nu(\beta z)+C_2I_{-\nu}(\beta z)$$

The particular integral is not that much straightforward. To find the particular part, variation of parameter can be employed. To apply this technique, equation (A.1) is modified for $\omega = \beta z$.

$$\frac{d^2u}{d\omega^2}+\left(\frac{1}{\omega}\right)\frac{du}{d\omega}-\left(1+\frac{\nu^2}{\omega^2}\right)u=f(\omega)=-\sum_{i=1}^{5}E_i\omega^{\gamma-2}$$

Now applying the variation of parameters, the particular solution will be –

$$u_{\mathrm{p}}(\omega)=\underbrace{-I_\nu(\omega)\int\frac{I_{-\nu}(\omega)}{\varpi\left\{I_\nu(\omega),I_{-\nu}(\omega)\right\}}f(\omega)d\omega}_{u_{P_1}}+\underbrace{I_{-\nu}(\omega)\int\frac{I_\nu(\omega)}{\varpi\left\{I_\nu(\omega),I_{-\nu}(\omega)\right\}}f(\omega)d\omega}_{u_{P_2}} \tag{A.2}$$

Here ϖ represents the Wronskian of Bessel function (I_ν and $I_{-\nu}$), which is $-2\sin(\nu\pi)/(\omega\pi)$ [62]. Considering the 1st part,

$$
\begin{aligned}
u_{\mathrm{p}1}(\omega) &= -I_{\nu}(\omega)\int \frac{I_{-\nu}(\omega)}{\varpi\left\{I_{\nu}(\omega),I_{-\nu}(\omega)\right\}} f(\omega)\,d\omega \\
&= -I_{\nu}(\omega)\sum_{i=1}^{5}\frac{E_i\pi}{2\sin(\pi\nu)}\int \omega^{\gamma-1}I_{-\nu}(\omega)\,d\omega
\end{aligned}
\tag{A.3}
$$

Hence, the integration of term containing Bessel function has to be determined first. For this purpose, the definition of Bessel function will be used in equation (A.3). The definition of modified Bessel function of first kind is available in any standard Math books [61, 63].

$$
I_{\pm\nu}(z)=\sum_{r=0}^{\infty}\frac{1}{r!\lceil r\pm\nu+1}\left(\frac{z}{2}\right)^{2r\pm\nu}
\tag{A.4}
$$

Using the definition (A.4) in the integration part of (A.3), it is straightforward to obtain,

$$
\int \omega^{\gamma-1}I_{\pm\nu}(\omega)d\omega = 2^{\mp\nu}\,\omega^{\pm\nu+\gamma}\underbrace{\sum_{r=0}^{\infty}\frac{1}{\left(2r\pm\nu+\gamma\right)r!\lceil r\pm\nu+1}\left(\frac{\omega}{2}\right)^{2r}}_{\text{Reducible to Hypergeometric Function}}
\tag{A.5}
$$

The last part of (A.5) can be replaced by the Hypergeometric function (See Appendix C), as given in (A.6).

$$
\sum_{r=0}^{\infty}\frac{1}{\left(2r\pm\nu+\gamma\right)r!\lceil r\pm\nu+1}\left(\frac{\omega}{2}\right)^{2r}=\left(\frac{1}{\left(\pm\nu+\gamma\right)\lceil \pm\nu+1}\right){}_1F_2\left(\frac{\pm\nu+\gamma}{2};\nu+1,\frac{\pm\nu+\gamma+2}{2};\frac{\omega^2}{4}\right)
\tag{A.6}
$$

Replacing (A.6) back into (A.2) will give the particular solution for z = (ω/β).

$$
\begin{aligned}
u_P(z) &= -\sum_{i=1}^{5}\frac{E_i\pi}{2\sin(\pi\nu)}\times z^{A} \\
&\left[I_{\nu}(\beta z)\frac{2^{\nu}\left(\beta z\right)^{\gamma-\nu}}{\left(\gamma-\nu\right)\lceil -\nu+1}\,{}_1F_2\left(\frac{\gamma-\nu}{2};-\nu+1,\frac{\gamma-\nu+2}{2};\frac{\beta^2z^2}{4}\right)\right. \\
&\left.-I_{-\nu}(\beta z)\frac{2^{-\nu}\left(\beta z\right)^{\gamma+\nu}}{\left(\gamma+\nu\right)\lceil \nu+1}\,{}_1F_2\left(\frac{\gamma+\nu}{2};\nu+1,\frac{\gamma+\nu+2}{2};\frac{\beta^2z^2}{4}\right)\right]
\end{aligned}
\tag{A.7}
$$

A.2 Derivatives of Particular Integral

The complete solution of carrier concentration is –

$$p(z) = \underbrace{C_1 I_\nu(\beta z) + C_2 I_{-\nu}(\beta z)}_{\text{Complementary Function}} + \underset{\text{Particular Integral}}{u_P(z)} \tag{A.8}$$

Where, $u_P(z)$ is defined in (A.7). For evaluating the current boundary condition, the derivatives of p(z) is necessary. Since p(z) contains both Bessel and Hypergeometric function, the derivatives will also contain this functions.

To consider the derivatives of Bessel function, the identity from the Appendix B will be helpful. The derivatives of complementary function in (A.8) can be easily derived using the identity below –

$$\frac{d}{dz}\left[z^A I_{\pm\nu}(\beta z)\right] = A z^{A-1} I_{\pm\nu}(\beta z) + z^A \left(\frac{\beta}{2}\right)\left[I_{\pm\nu-1}(\beta z) + I_{\pm\nu+1}(\beta z)\right] \tag{A.9}$$

Now to obtain the derivatives of particular integral of (A.8), both differentiation of Bessel and Hypergeometric function are necessary. Taking help from Appendix C, the derivatives of z dependent part in (A.7) can be obtained as follows –

$$\begin{aligned}
&\frac{d}{dz}\left[I_\nu(\beta z) z^{\gamma-\nu+A}\, {}_1F_2\left(\frac{\gamma-\nu}{2}; -\nu+1, \frac{\gamma-\nu+2}{2}; \frac{\beta^2 z^2}{4}\right)\right] \\
&= z^{\gamma-\nu+A}\, {}_1F_2\left(\frac{\gamma-\nu}{2}; -\nu+1, \frac{\gamma-\nu+2}{2}; \frac{\beta^2 z^2}{4}\right)\left[\beta I_{\nu+1}(\beta z) + I_\nu(\beta z)\left(\frac{\gamma+A}{z}\right)\right] \\
&+ I_\nu(\beta z) z^{\gamma-\nu+A}\, {}_1F_2\left(\frac{\gamma-\nu+2}{2}; -\nu+2, \frac{\gamma-\nu+4}{2}; \frac{\beta^2 z^2}{4}\right)\frac{(\gamma-\nu)(-\nu+1)}{2(\gamma-\nu+1)}\left(\frac{\beta^2 z}{2}\right)
\end{aligned} \tag{A.10}$$

Combining the above derivatives (A.9)–(A.10) will results in [dp(z)/dz] of the complete solution p(z).

Appendix B

Bessel Function

The theory of Bessel functions is intimately connected with the theory of a certain type of differential equation of the first order, known as Ricatti's equation. In fact, Bessel function is usually defined as a particular solution of a linear differential equation of the second order (known as Bessel's equation) which is derived from Ricatti's equation by an elementary transformation. This type of differential equation is quite common in advance scientific and engineering problems. Bessel function is often encountered when solving boundary value problems, such as separable solutions to Laplace's equation or the Helmholtz equation, especially when working in cylindrical or spherical coordinates.

B.1 Bessel Function of the First Kind

Let us consider the following second-order differential equation,

$$z^2 u''(\mathrm{z}) + \mathrm{zu}'(\mathrm{z}) + \left(\mathrm{z}^2 - \nu^2\right) u(\mathrm{z}) = 0 \tag{B.1}$$

This is known as the Bessel's equation. ν is an unrestricted (real or complex) number that is called the order of the Bessel equation.

The Bessel differential equation can be solved by adopting an infinite series solution. By taking $u(r,\nu) = \sum_{r=0}^{\infty} a_r z^{r+\nu}$ as a solution of equation (B.1) and evaluating the constant a_r, it is straightforward to obtain the solution of Bessel equation [61]. The solution is known as Bessel function and has the following mathematical form,

$$J_\nu(\mathrm{z}) = \sum_{r=0}^{\infty} \frac{(-1)^{\mathrm{r}}}{r!\,\overline{|r+\nu+1}} \left(\frac{z}{2}\right)^{2r+\nu} \tag{B.2}$$

Since equation (B.1) is a second order differential equation, there must be two linearly independent solutions. Typically the general solution is given as (B.3).

$$u(z) = C_1 J_\nu(\mathrm{z}) + C_2 Y_\nu(\mathrm{z}) \tag{B.3}$$

Here, second solution $Y_\nu = [J_\nu(z)\cos(\nu\pi) - J_{-\nu}(z)]/\sin(\nu\pi)$ and C_1, C_2 are constants. In summary,

$J_\nu(x)$	Bessel functions of the first kind, which are finite at x=0 for all real values of ν
$Y_\nu(x)$	Bessel functions of the second kind, (also known as Weber or Neumann functions) which are singular at x=0

B.2 Modified Bessel Function of First Kind

The equation that is encountered in this thesis is slightly different than equation (B.1).

$$z^2u''(z)+zu'(z)-\left(z^2+\nu^2\right)u(z)=0 \tag{B.4}$$

This is known as modified Bessel equation. Comparing (B.4) with (B.1), the solution for the modified Bessel equation can be derived by a simple change of variable from z to iz ($i=\sqrt{-1}$),

$$u(z)=C_1J_\nu(i\,z)+C_2Y_\nu(i\,z) \tag{B.5}$$

Defining $I_\nu(z)=i^{-\nu}J_\nu(iz)$, the solution becomes real function of z,

$$I_\nu(z)=\sum_{r=0}^{\infty}\frac{1}{r!\,\Gamma(r+\nu+1)}\left(\frac{z}{2}\right)^{2r+\nu} \tag{B.6}$$

$$K_n(z)=\frac{\pi}{2}\left(\frac{I_{-\nu}(z)-I_\nu(z)}{sin(\pi\nu)}\right) \tag{B.7}$$

I_ν and K_ν are the modified Bessel function of 1st and 2nd kind of order ν. The functions are exponentially growing and decaying function, as shown in fig. B.1.

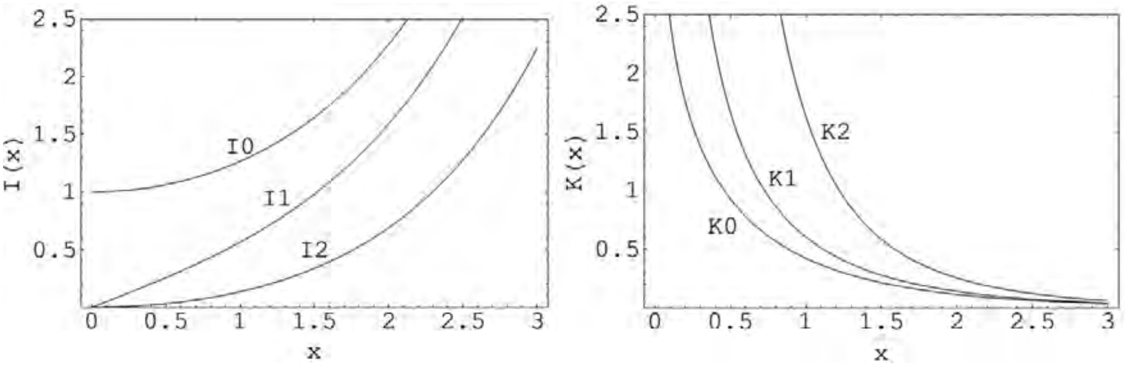

Fig. B.1 The plot of modified Bessel function of 1st and 2nd kind, for integer order

It should be mentioned here that I_ν and K_ν are not the only solution set of (B.4). I_ν and $I_{-\nu}$ can also be the solutions of (B.4)[63]. This is evident from the relationship in (B.7). When ν is a non-integer order, I_ν and $I_{-\nu}$ represent the independent solution; while for integer ν, $I_{-\nu}(z) = I_\nu(z)$.

B.3 Recurrence Relationship of Modified Bessel Functions

Several identities of modified Bessel function exists in literature [61]. This thesis has amply used some of these relations, when necessary.

$$I_{\nu+1}(\mathrm{z}) = I_{\nu-1}(\mathrm{z}) - \left(\frac{2\nu}{z}\right) I_{\nu}(\mathrm{z})$$
$$I'_{\nu}(\mathrm{z}) = \frac{1}{2}\left[I_{\nu-1}(\mathrm{z}) + I_{\nu+1}(\mathrm{z})\right]$$
$$I'_{\nu}(\mathrm{z}) = I_{\nu-1}(\mathrm{z}) - \left(\frac{\nu}{z}\right) I_{\nu}(\mathrm{z})$$
$$I'_{\nu}(\mathrm{z}) = \left(\frac{\nu}{z}\right) I_{\nu}(\mathrm{z}) + I_{\nu+1}(\mathrm{z})$$
$$\frac{d}{dz}\left[z^{\nu} I_{\nu}(\mathrm{z})\right] = z^{\nu} I_{\nu-1}(\mathrm{z})$$
$$\frac{d}{dz}\left[z^{-\nu} I_{\nu}(\mathrm{z})\right] = z^{-\nu} I_{\nu+1}(\mathrm{z})$$

$$K_{\nu+1}(\mathrm{z}) = K_{\nu-1}(\mathrm{z}) + \left(\frac{2\nu}{z}\right) K_{\nu}(\mathrm{z})$$
$$K'_{\nu}(\mathrm{z}) = -\frac{1}{2}\left[K_{\nu-1}(\mathrm{z}) + K_{\nu+1}(\mathrm{z})\right]$$
$$K'_{\nu}(\mathrm{z}) = -K_{\nu-1}(\mathrm{z}) - \left(\frac{\nu}{z}\right) K_{\nu}(\mathrm{z})$$
$$K'_{\nu}(\mathrm{z}) = \left(\frac{\nu}{z}\right) K_{\nu}(\mathrm{z}) - K_{\nu+1}(\mathrm{z})$$
$$\frac{d}{dz}\left[z^{\nu} K_{\nu}(\mathrm{z})\right] = -z^{\nu} K_{\nu-1}(\mathrm{z})$$
$$\frac{d}{dz}\left[z^{-\nu} K_{\nu}(\mathrm{z})\right] = -z^{-\nu} K_{\nu+1}(\mathrm{z})$$

B.4 Approximation of Modified Bessel Function

The modified Bessel function can be approximated by some functional forms. These functional relationships are applicable for certain types of argument (z) and order (ν). This thesis has briefly explored the ways of simplifying the derived analytical equations using some specific mathematical approximations. Hence, a short summary of approximating the Bessel function is added here to help that discussion.

A. Integral representation of I_{ν}:

This representations are valid for both integer and non–integer values of ν.

$$I_{\nu}(\mathrm{z}) = \frac{1}{\pi}\int_{0}^{\pi} \cos(\mathrm{n}\,\theta)\exp(\mathrm{x}\cos\theta)\,\mathrm{d}\,\theta$$

$$K_{\nu}(\mathrm{z}) = \frac{\sqrt{\pi}\,(\mathrm{x}+2)^{\nu}}{\left\lceil \nu + \frac{1}{2} \right.}\int_{0}^{\infty} \sinh^{2\nu}(t)\exp(-\mathrm{x}\cosh t)\,\mathrm{d}\,t; \quad \text{for } \mathrm{x} > 0$$

$$K_{\nu}(\mathrm{z}) = \int_{0}^{\infty} \cosh\left(nt\right) \exp(-\mathrm{x}\cosh t)\,\mathrm{d}\,t; \qquad \text{for x} > 0$$

B. Asymptotic approximation of modified Bessel Function:

This approximation is valid for large values of z.

$$I_{\nu}(\mathrm{z}) = \frac{e^{x}}{\sqrt{2\pi z}}\left[1-\frac{4\nu^{2}-1^{2}}{1(8\,\mathrm{z})}\left(1-\frac{4\nu^{2}-3^{2}}{2(8\,\mathrm{z})}\left(1-\frac{4\nu^{2}-5^{2}}{3(8\,\mathrm{z})}(1-...)\right)\right)\right]$$

C. Power series expansion of Modified Bessel Function

This expansion is valid for positive order ν,

$$I_{\nu}(z) = \sum_{r=0}^{\infty}\frac{1}{r!\overline{\left|r+\nu+1\right.}}\left(\frac{z}{2}\right)^{2r+\nu}$$

$$= \frac{1}{\overline{\left|1+\nu\right.}}\left(\frac{x}{2}\right)^{\nu}\left\{1+\frac{(\mathrm{x}/2)^{2}}{1(1+\mathrm{v})}\left(1+\frac{(\mathrm{x}/2)^{2}}{2(2+\mathrm{v})}\left(1+\frac{(\mathrm{x}/2)^{2}}{3(3+\mathrm{v})}(1+...)\right)\right)\right\}$$

Similarly for negative ν,

$$I_{-\nu}(z) = \sum_{r=0}^{\infty}\frac{1}{r!\overline{\left|r+\nu+1\right.}}\left(\frac{z}{2}\right)^{2r-\nu}$$

$$= \frac{1}{\overline{\left|1-\nu\right.}}\left(\frac{x}{2}\right)^{-\nu}\left\{1+\frac{(\mathrm{x}/2)^{2}}{1(1-\mathrm{v})}\left(1+\frac{(\mathrm{x}/2)^{2}}{2(2-\mathrm{v})}\left(1+\frac{(\mathrm{x}/2)^{2}}{3(3-\mathrm{v})}(1+...)\right)\right)\right\}$$

D. Alternate Power series expansion of Modified Bessel Function

This is another representation of Modified Bessel Function,

$$I_{\nu}(\mathrm{z}) = \frac{z^{\nu}}{\nu!}\left[1+\frac{z^{2}}{1(\nu+1)}\left(1+\frac{z^{2}}{2(\nu+2)}\left(1+\frac{z^{2}}{3(\nu+3)}\left(1+\frac{z^{2}}{4(\nu+4)}(1+...)\right)\right)\right)\right]$$

$$K_{\nu}(\mathrm{z}) = \left(\frac{\pi}{2z}\right)^{\frac{1}{2}} e^{-z}\left[1+\frac{4\nu^{2}-1^{2}}{1(8\,\mathrm{z})}\left(1+\frac{4\nu^{2}-1^{2}}{1(8\,\mathrm{z})}\left(1+\frac{4\nu^{2}-3^{2}}{2(8\,\mathrm{z})}\left(1+\frac{4\nu^{2}-5^{2}}{3(8\,\mathrm{z})}(1+...)\right)\right)\right)\right]$$

Appendix C

Hypergeometric Function

C.1 Definition of Hypergeometric function

To introduce the Hypergeometric function, first Pochhammer symbol $(\alpha)_r$ needs to be defined as follows –

$$(\alpha)_r = \alpha(\alpha+1)\ldots(\alpha+r-1) = \frac{\Gamma(\alpha+r)}{\Gamma(\alpha)} \quad ;\ (\text{r is positive}) \qquad (C.1)$$

Here, $(\alpha)_0 = 1$. The general Hypergeometric function is defined using the Pochhammer symbol of (C.1), as shown in equation (C.2).

$$ {}_{\mathrm{p}}\mathrm{F}_{\mathrm{q}}\left(\alpha_1,\alpha_2,\ldots,\alpha_{\mathrm{p}};\beta_1,\beta_2,\ldots,\beta_{\mathrm{q}};\ \mathrm{x}\right) = \sum_{r=0}^{\infty} \frac{(\alpha_1)_r(\alpha_2)_r(\alpha_3)_r\ldots..(\alpha_{\mathrm{p}})_r}{(\beta_1)_r(\beta_2)_r(\beta_3)_r\ldots..(\beta_{\mathrm{q}})_r}\left(\frac{x^r}{r!}\right) \qquad (C.2)$$

The derivatives of general Hypergeometric function is given by –

$$\begin{aligned} &\frac{d}{dx}\left[{}_{\mathrm{p}}\mathrm{F}_{\mathrm{q}}\left(\alpha_1,\alpha_2,\ldots,\alpha_{\mathrm{p}};\beta_1,\beta_2,\ldots,\beta_{\mathrm{q}};\ \mathrm{x}\right)\right] \\ &= \frac{\alpha_1\alpha_2\alpha_3\ldots\alpha_{\mathrm{p}}}{\beta_1\beta_2\beta_3\ldots\beta_{\mathrm{q}}}\left[{}_{\mathrm{p}}\mathrm{F}_{\mathrm{q}}\left(\alpha_1+1,\alpha_2+1,\ldots,\alpha_{\mathrm{p}}+1;\beta_1+1,\beta_2+1,\ldots,\beta_{\mathrm{q}}+1;\ \mathrm{x}\right)\right] \end{aligned} \qquad (C.3)$$

The general Hypergeometric function that is used in this thesis is ${}_1F_2$, which can be calculated using the general relationship of equation (C.2).

$${}_1F_2(\alpha;\beta_1,\beta_2;z) = \sum_{r=0}^{\infty}\frac{(\alpha)_r}{(\beta_1)_r(\beta_2)_r}\left(\frac{z^r}{r!}\right) \qquad (C.4)$$

C.2 Convergence Criteria of Hypergeometric Function

The convergence of Hypergeometric function depends on the values of p and q. If α_r and β_r in (C.3) are not non-positive integers for any r, then the **Ratio Test** [78] can provide the necessary convergence criteria for the Hypergeometric function.

Table C.1 Convergence Criteria of generalized Hypergeometric function

Condition for ${}_pF_q(\cdot)$	**Convergence Criteria**
$p \le q$	The ratio of coefficients of z^r in the Taylor series of Hypergeometric function tends to 0 as $r \to \infty$. Hence *the radius of curvature is* ∞ *and the series converges for all values of* $\lvert z \rvert$. For example, the radius of curvature for ${}_0F_1$ and ${}_1F_1$ is ∞.
$p = q + 1$	The ratio of coefficients of z^r in the Taylor series of Hypergeometric function tends to 1 as $r \to \infty$. So *the radius of convergence is 1, i.e. the series converges only for* $\lvert z \rvert < 1$. For example, the radius of curvature for ${}_2F_1$ is 1.
$p > q + 1$	The ratio of coefficients of z^r tends to ∞ as $r \to \infty$. So *the radius of curvature is 0 and the series does not converge for any values of* $\lvert z \rvert$.

According to the table C.1, ${}_1F_2$ Hypergeometric function will converge for all values of |z|. Since z is defined as exponentially decaying function of x (see chapter 3), the maximum values of z is 1 (non-negative integer).

C.3 Computing Hypergeometric Function

For computing the Hypergeometric function, this work has used MATLAB, Wolfram MATHEMATICA Kernel and MAPLE Math Engine. MATLAB routine for computing Hypergeometric functions, "hypergeom", is generally slow but tolerable for all parameter and variable values (MATLAB usually took around 5-12 seconds to compute Hypergeometric function the first time after loading the program). Hence MAPLE math Engine Toolbox is incorporated in MATLAB to achieve faster calculation ${}_1F_2$. Along with that, similar program is developed in MATHEMATICA to check the validity of the MATLAB Hypergeometric function.

The methods to calculate Hypergeometric function by MATLAB and MATHEMATICA are not released publicly. But some authors have developed some excellent package of program/routines, which are published as open-source [79].

Appendix D

Standard Solar Spectrum

D.1 Terrestrial Solar Spectrum

The energy from the Sun is distributed, in ways that depend on variables like latitude, time of day, and atmospheric conditions, over different wavelengths. The various distributions that are possible are called solar spectra. Due to the variation of solar spectrum with weather, season, time of day, and location, standard spectra are needed to be defined universally. Having standard spectra allows the experimental solar cell performance of one device to be compared to that of other devices and to be judged fairly, since the cells can be exposed to the same agreed-upon spectrum. The comparisons can be done even in the laboratory since standard distributions can be duplicated using solar simulators [41].

The two spectrums that are relevant on the earth's surface are referred to as the AM1.5G and the AM1.5D spectrum. The AM1.5G spectrum includes direct and diffused radiation and has an integrated power density of 1000 W/m^2. This spectrum is relevant for flat panel photovoltaic cells. The AM1.5D spectrum consists of only direct radiation from the sun and is applicable to concentrator photovoltaic cells. It has an integrated power density of 900W/m^2 [80].

The standardization of the solar spectrum is recognized by the photovoltaic (PV) industry, the American Society for Testing and Materials (ASTM) [81] and government research and development laboratories. Only AM1.5G and AM1.5D are the terrestrial solar spectral irradiance distributions those are defined as standard. The current Standard Reference Spectra (ASTM G173) can be obtained from [82] and has presented in fig. D.1.

Standard Direct Normal Spectral Irradiance	Direct component contributing to the total global (hemispherical) spectrum
Standard Total Spectral Irradiance	Global, hemispherical, within 2π Steradian field of view of the tilted plane

The standard terrestrial spectral irradiance is for a surface of specified orientation under specific set of atmospheric conditions. The power distributions as a function of wavelength provide a single common reference for evaluating spectrally selective PV materials with respect to performance measured under varying natural and artificial sources of light with various spectral distributions. The specified atmospheric conditions are [66]:

- The 1976 U.S. Standard Atmosphere with temperature, pressure, aerosol density (rural aerosol loading), air density, molecular species density specified in 33 layers
- An absolute air mass of 1.5 (solar zenith angle 48.19°s)
- Angstrom turbidity (base e) at 500 nm of 0.084 c
- Total column water vapor equivalent of 1.42 cm
- total column ozone equivalent of 0.34 cm
- Surface spectral albedo (reflectivity) of Light Soil as documented in the Jet Propulsion Laboratory ASTER Spectral Reflectance Database

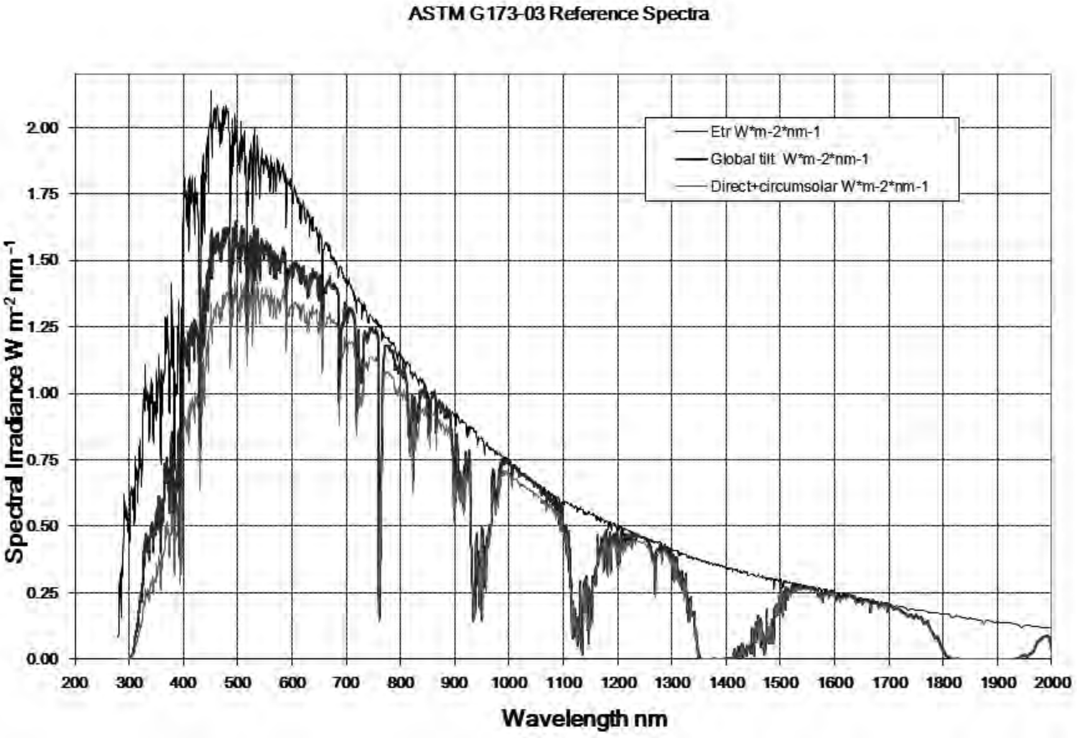

Fig. D.1 ASTM G173 standard solar spectrums: AM1.5G, AM1.5D, AM0 [66]

D.2 Extraterrestrial Solar Spectrum

The spectrum of available energy from the sun at the outer edge of the earth's atmosphere is referred to as the air mass zero (AM0) spectrum. This spectrum has an integrated power density of 1366.1 W/m^2.

ASTM has developed this AM0 reference spectrum (ASTM E-490) using the data from satellites, space shuttle missions, high-altitude aircraft, rocket soundings, ground-based solar telescopes, and modeled spectral irradiance [83]. This spectral irradiance is specifically suitable for the aerospace community. Figure D.1 shows the irradiance profile of AM0 extraterrestrial spectrum.

D.3 Global Solar Energy Distribution

The annual power from the sun depends on the location over the Earth and in average, the energy to the Earth's surface is 730,000 Trillion KWh [84]. The global distribution of solar radiation is shown in fig. D.2.

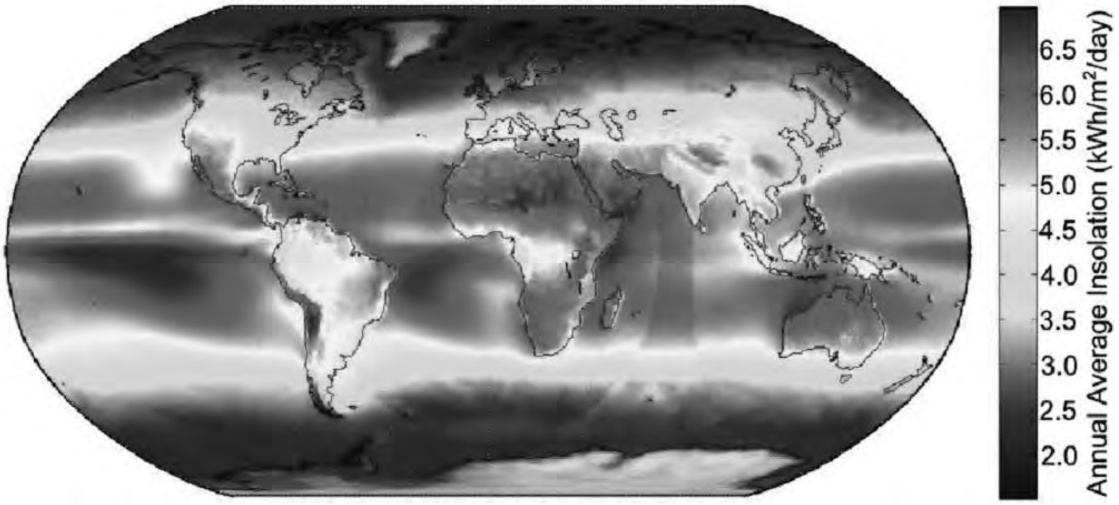

Fig. D.2 Global average annual insolation. Data from NASA [84].

Appendix E

Silvaco/Atlas Code

E.1 Simple P^+N Solar Cell

```
GO ATLAS

MESH AUTO

X.MESH LOC=0.0 SPACING=0.1

X.MESH LOC=2.0 SPACING=0.1


Y.MESH LOC=0.0 SPACING=0.01

Y.MESH LOC=0.5 SPACING=0.01

Y.MESH LOC=2.0 SPACING=0.2


REGION NUM=1 MATERIAL=SILICON Y.MIN=0.00 Y.MAX=2

ELECTRODE NUM=1 NAME=ANODE X.MIN=0 X.MAX=0.5 Y.MAX=0.0 MATERIAL=ALUMINUM

ELECTRODE NUM=2 NAME=CATHODE Y.MIN=1 MATERIAL=ALUMINUM

MATERIAL MATERIAL=ALUMINUM SOPRA=AL.NK

DOPING P.TYPE CONC=5E18 UNIFORM
DOPING N.TYPE Y.MIN = 0 Y.MAX = 0.5 ASCII INFILE=EXPONENTIAL_DOPING

CONTACT NAME=ANODE SURF.REC VSURFP=5E2
SAVE OUTF=SOLAR.STR

# SET LIGHT BEAM USING SOLAR SPECTRUM FROM EXTERNAL FILE
BEAM NUM=1 X.ORIGIN=1.0 Y.ORIGIN=-1.0 ANGLE=90.0 AM1.5

# SAVES OPTICAL INTENSITY TO SOLUTION FILES
# OUTPUT OPT.INT

# MODELS SRH CONMOB FERMI NI.FERMI BGN OPTR AUGER
MODEL PRINT SRH CONMOB BGN OPTR AUGER

SOLVE INIT
SOLVE PREV

#
# TURN ON THE SUN.
#
SOLVE B1=0.0
STRUCTURE OUTF = PN_SUN.STR
TONYPLOT PN_SUN.STR
```

E.2 General 2D Solar Cell Code

```
GO ATLAS

TITLE 2-D SOLAR CELL SIMULATOR, by B. DEBNATH, 2014

#       THE LIGHT IS INCIDENT ON INTERFACE AT Y = 0 OVER n+ REGION
#       DEVICE IS CONSTRUCTED ALONG +Y DIRECTION

# ---------------------- < DEVICE PARAMETERS   >-----------------------

# DEVICE LENGTH (ALONG X)
  SET LENGTH = 100
  SET HALF_LENGTH = 50

# N+P METALURGICAL JUNCTION
  SET NP_JUNCTION = 0.5

# P REGION WIDTH FROM N+P JUNCTION
  SET P_WIDTH = 50

# DOPING PROFILE
       # N+ REGION CONCENTRATION (PER cm-3)
         SET N_DOPING = 5.0E+19
       # P REGION CONCENTRATION (PER cm-3)
         SET P_DOPING = 1.5E+16

# FRONT SURFACE
       # ELECTRODE THICKNESS
         SET ELECTRODE_THICKNESS = 0.100
       # OXIDE THICKNESS
         SET OXIDE_THICKNESS = 0.050
       # FRONT SURFACE RECOMBINATION VELOCITY (cm/s)
         SET FRONT_RECOM_VELOCITY = 5e2
       # ELECTRODE LENGTH
         SET ELECTRODE_HALF_LENGTH = 2
# BACK SURFACE
       # BACK SURFACE RECOMBINATION VELOCITY (cm/s)
         SET BACK_RECOM_VELOCITY = 2e5


# LIGHT SOURCE
       # AIR MASS 1.5 (THETA = 45 DEGREE)
         SET THETA = 90.0
       # LIGHT POSITION
         SET LIGHT_X = $HALF_LENGTH
         SET LIGHT_Y = -1
       # LIGHT INTENSITY (W/SQ.cm)
         SET LIGHT_INTENSITY = 1


# ----------< DERIVED DEVICE PARAMETERS  >--------------------

# DEPLETION WIDTH (0.28273 um)
  SET DEPLETION_WIDTH = 0.300

# FOR FINE MESHING BEFORE DEPLETION REGION
  SET DEPLETION_START = $NP_JUNCTION - 0.100

# END OF FINE MESHING INSIDE DEPLETION REGION
  SET DEPLETION_END = $NP_JUNCTION + $DEPLETION_WIDTH + 1

# TOTAL DEVICE WIDTH
  SET DEVICE_WIDTH = $NP_JUNCTION + $P_WIDTH

# END OF DEVICE ALONG Y
```

```
  SET END_OF_DEVICE = $DEVICE_WIDTH + $ELECTRODE_THICKNESS


# TRANSPARENT ELECTRODE WINDOW STARTING X (INACTIVE)
  SET ELECTRODE_WINDOW_START = $HALF_LENGTH - $ELECTRODE_HALF_LENGTH

# TRANSPARENT ELECTRODE WINDOW ENDING X (INACTIVE)
  SET ELECTRODE_WINDOW_END = $HALF_LENGTH + $ELECTRODE_HALF_LENGTH

# ELIMINATION BOUNDARY Y => ELIMINATE MESHING UPTO THIS Y FROM DEPLETION END
  SET ELIMINATION_BOUNDARY_Y = $END_OF_DEVICE - 5

# FINE GRID STARTING FOR THE SILICON LAYER NEAR ANODE
  SET ANODE_GRID_STARTING = $ELIMINATION_BOUNDARY_Y + 1

# ---------------------- < MESHING >------------------------
MESH          SPACE.MULT = 3
X.MESH        LOC = 0                         SPAC = 0.1
X.MESH        LOC = 0.5                       SPAC = 1
X.MESH        LOC = $HALF_LENGTH              SPAC = 10
X.MESH        LOC = $LENGTH                   SPAC = 20


Y.MESH        LOC = -$ELECTRODE_THICKNESS     SPAC = 0.050
Y.MESH        LOC = -$OXIDE_THICKNESS         SPAC = 0.050
Y.MESH        LOC = 0                         SPAC = 0.050
Y.MESH        LOC = 0.25                      SPAC = 0.050
Y.MESH        LOC = $NP_JUNCTION              SPAC = 0.05
Y.MESH        LOC = $DEPLETION_START          SPAC = 0.05
Y.MESH        LOC = $DEPLETION_END            SPAC = 0.1

Y.MESH        LOC = $ELIMINATION_BOUNDARY_Y   SPAC = 5
Y.MESH        LOC = $ANODE_GRID_STARTING      SPAC = 0.5
Y.MESH        LOC = $DEVICE_WIDTH             SPAC = 0.1
Y.MESH        LOC = $END_OF_DEVICE            SPAC = 0.1

# ELIMINATION IN NEUTRAL REGION FOR FAST CALCULATION
ELIMINATE X.DIR X.MIN = 1 X.MAX = $LENGTH Y.MIN = $DEPLETION_END Y.MAX =
$ELIMINATION_BOUNDARY_Y
ELIMINATE Y.DIR X.MIN = 1 X.MAX = $LENGTH Y.MIN = $DEPLETION_END Y.MAX =
$ELIMINATION_BOUNDARY_Y

# ---------------------- < REGIONS >------------------------
# SILICON LAYER
REGION NUM = 1 Y.MIN = 0 Y.MAX = $DEVICE_WIDTH X.MIN = 0 X.MAX = $LENGTH
MATERIAL = SILICON

# TOP AIR REGION
REGION NUM = 2 Y.MIN = -$ELECTRODE_THICKNESS Y.MAX = 0 X.MIN = 0 X.MAX =
$LENGTH MATERIAL = AIR

# ALUMINUM STRIP OVER n+ MATERIAL
# REGION NUM = 4 Y.MIN = -$ELECTRODE_THICKNESS Y.MAX = 0 X.MIN =
$ELECTRODE_WINDOW_START \
#                     X.MAX = $ELECTRODE_WINDOW_END  MATERIAL = ALUMINUM



# ---------------------- < SET THE ELECTRODES  >------------------------
# TOP ELECTRODE OVER n+ MATERIAL
ELECTRODE NAME = ANODE Y.MIN = -$ELECTRODE_THICKNESS Y.MAX = 0 X.MIN = 0 \
                      X.MAX = 0.1 MATERIAL = ALUMINUM

# BOTTOM ELECTRODE BELOW P+ MATERIAL
ELECTRODE NAME = CATHODE Y.MIN = $DEVICE_WIDTH Y.MAX = $END_OF_DEVICE \
                      X.MIN = 0 X.MAX = $LENGTH MATERIAL = ALUMINUM
```

```
# ---------------------- < DOPING PROFILE >-----------------------
# N+ DOPING
DOPING UNIFORM N.TYPE CONC = $N_DOPING Y.MIN = 0 Y.MAX = $NP_JUNCTION \
                                 X.MIN = 0 X.MAX = $LENGTH

# N+ DOPING
# DOPING GAUSS N.TYPE CONC = $N_DOPING PEAK = 0.0 CHAR = 0.1 X.LEFT = 0
X.RIGHT = $LENGTH


# P DOPING
DOPING UNIFORM P.TYPE CONC = $P_DOPING Y.MIN = $NP_JUNCTION \
             Y.MAX = $DEVICE_WIDTH X.MIN = 0 X.MAX = $LENGTH


# ---------------------- < MATERIALS >-----------------------
# ELECTRODE
# MATERIAL MATERIAL = ALUMINUM IMAG.INDEX = 1


# FOR AMORPHOUS SILICON
# MATERIAL MATERIAL = SILICON MUN = 20 MUP = 1.5

MATERIAL MATERIAL=ALUMINUM SOPRA=AL.NK

# --------------------- < SPECIFY CONTACT TYPE >--------------------
CONTACT NAME = ANODE       SURF.REC      VSURFP = $FRONT_RECOM_VELOCITY
CONTACT NAME = CATHODE     SURF.REC      VSURFN = $BACK_RECOM_VELOCITY


# ---------------------- < SAVE STRUCTURE >-----------------------
STRUCTURE OUTFILE = SOLAR_CELL_2D.STR
# TONYPLOT SOLAR_CELL_2D.STR


# --------------------- < LIGHT SOURCE >-----------------------------
BEAM NUM = 1 X.ORIGIN = $LIGHT_X Y.ORIGIN = $LIGHT_Y ANGLE = 90.0 AM1.5 \
rays = 10


# --------------------- < SPECIFY MODELS >------------------------------
# SAVE OPTICAL INTENSITY TO SOLUTION FILE
OUTPUT OPT.INT
OUTPUT BAND.PARAM CON.BAND
MODELS FLDMOB SRH CONMOB BGN OPTR PRINT
METHOD TRAP MAXTRAP = 10

# DO NOT USE CONMOB FOR POLYSILICON SELECTION
# OTHERWISE, IT WILL REPLACE LOW MUN, MUP
# MODELS CONMOB
SOLVE

SOLVE B1 = 1
SAVE OUTFILE = SOLAR_CELL_WITH_BEAM.STR
TONYPLOT SOLAR_CELL_WITH_BEAM.STR



# ---------------------- < ANALYSIS > --------------------------------

# --- < I-V CURVE > --
SOLVE B1 = 1
SOLVE VCATHODE = -1 VSTEP = 0.05 VFINAL = 0.1 NAME = CATHODE

LOG OUTFILE = Id_Vd.LOG
SOLVE VCATHODE=0 VSTEP = 0.005 VFINAL = 0.6 NAME = CATHODE
TONYPLOT Id_Vd.LOG
LOG OFF
```

```
# --- < SHORT CIRCUIT CURRENT (MAX CURRENT OF CATHODE CURRENT)> ---
LOG OUTFILE = SHORT_CIRCUIT.LOG
SOLVE B1 = $LIGHT_INTENSITY
SAVE OUTFILE = SOLAR_CELL_SHORT_CIRCUIT.STR


# --- < OPEN CIRCUIT VOLTAGE (MAX OF CATHODE INTERNAL VOLTAGE) > --
SOLVE INIT
CONTACT NAME = CATHODE CURRENT
SOLVE ICATHODE = 0 B1 = $LIGHT_INTENSITY
SAVE OUTFILE = SOLAR_CELL_OPEN_CIRCUIT.STR


# --------< SPECTRAL EFFICIENCY WITH A MONOCROMATIC LIGHT SOURCE >------
BEAM NUM = 1 X.ORIGIN = $LIGHT_X Y.ORIGIN = $LIGHT_Y ANGLE = 45.0 RAYS = 30

SOLVE INIT B1 = 0
LOG OUTFILE=SPECTRAL_EFFICIENCY.LOG
SOLVE B1 = 1 LAMBDA = 0.1
SOLVE B1 = 1 LAMBDA = 0.2
SOLVE B1 = 1 LAMBDA = 0.3
SOLVE B1 = 1 LAMBDA = 0.4
SOLVE B1 = 1 LAMBDA = 0.5
SOLVE B1 = 1 LAMBDA = 0.6
SOLVE B1 = 1 LAMBDA = 0.7
SOLVE B1 = 1 LAMBDA = 0.8
SOLVE B1 = 1 LAMBDA = 0.9
```

E.3 General 3D Solar Cell Code

```
GO ATLAS

TITLE 3-D SOLAR CELL SIMULATOR, by B. DEBNATH, 2014

#       THE LIGHT IS INCIDENT ON INTERFACE AT y = 0 OVER n+ REGION
#       DEVICE IS CONSTRUCTED ALONG +y DIRECTION

# ---------------------- < DEVICE PARAMETERS   >-----------------------

# DEVICE LENGTH (ALONG X)
  SET LENGTH = 2

# DEVICE WIDTH (ALONG Z)
  SET WIDTH = 2

# SILICON LAYER WITH DONOR DOPING (n TYPE)
      # THICKNESS
        SET SI_N_THICKNESS = 0.5
      # DOPING
        SET SI_N_DOPING   = 5e+19

# SILICON LAYER WITH ACCEPTOR DOPING (P TYPE)
      # THICKNESS
        SET SI_P_THICKNESS = 2
      # DOPING
        SET SI_P_DOPING   = 1.5e+16

# FRONT SURFACE
      # ELECTRODE FINGER
        SET FNGER_NUMBER = 5
      # ELECTRODE THICKNESS
        SET ELECTRODE_THICKNESS = 0.005
```

```
       # FRONT SURFACE RECOMBINATION VELOCITY
         SET FRONT_RECOM_VELOCITY = 1e2

# BACK SURFACE
       # BACK SURFACE RECOMBINATION VELOCITY
         SET BACK_RECOM_VELOCITY = 1e5


# LIGHT SOURCE
       # LIGHT INTENSITY (G)
         SET LIGHT_INTENSITY = 1.0
       # LIGHT POSITION
         SET LIGHT_X = 1
         SET LIGHT_Z = 1
       # LIGHT HEIGHT FROM DEVICE SURFACE Y = 0
         SET LIGHT_Y = 1


# ------------------ <     DERIVED DEVICE PARAMETERS  >-----------------------
       # DEVICE THICKNESS
         SET DEVICE_THICKNESS = $SI_P_THICKNESS + $SI_N_THICKNESS
       # BOTTOM OF DEVICE
         SET BOTTOM_OF_DEVICE = $DEVICE_THICKNESS + $ELECTRODE_THICKNESS
       # SET BOUNDARY REGION BELOW P TYPE WHERE COARSE MESHING WILL BE APPLIED
         SET COURSE_MESH_BOUNDARY = $SI_N_THICKNESS + 0.05


# ---------------------- < MESHING >------------------------
MESH THREE.D

X.MESH       LOC = 0                     SPAC = 0.5
X.MESH       LOC = $LENGTH               SPAC = 0.5

Y.MESH       LOC = -$ELECTRODE_THICKNESS       SPAC = 0.3
Y.MESH       LOC = 0                     SPAC = 0.05
Y.MESH       LOC = $SI_N_THICKNESS       SPAC = 0.5
Y.MESH       LOC = $DEVICE_THICKNESS     SPAC = 1
Y.MESH       LOC = $BOTTOM_OF_DEVICE     SPAC = 0.3

Z.MESH       LOC = 0                     SPAC = 0.5
Z.MESH       LOC = $WIDTH                SPAC = 0.5


# ---------------------- < REGIONS >------------------------
# TOP SILICON LAYER - N TYPE
REGION NUM = 1 X.MIN = 0 X.MAX = $LENGTH Y.MIN = 0 Y.MAX = $SI_N_THICKNESS \
             Z.MIN = 0 Z.MAX = $WIDTH MATERIAL = SILICON

# TOP OXIDE LAYER
REGION NUM = 2 X.MIN = 0 X.MAX = $LENGTH Y.MIN = -$ELECTRODE_THICKNESS \
Y.MAX = 0 Z.MIN = 0 Z.MAX = $WIDTH MATERIAL = OXIDE

# BOTTOM LAYER - P TYPE
REGION NUM = 3 X.MIN = 0 X.MAX = $LENGTH Y.MIN = $SI_N_THICKNESS Y.MAX =
$DEVICE_THICKNESS Z.MIN = 0 Z.MAX = $WIDTH MATERIAL = SILICON

# ALUMINUM LAYER - TOP ELECTRODE
REGION NUM = 4 X.MIN = 0 X.MAX = 0.25 Y.MIN = -$ELECTRODE_THICKNESS   Y.MAX =
0 Z.MIN = 0 Z.MAX = 0.25 MATERIAL = ALUMINUM


# ---------------------- < SET THE ELECTRODES  >------------------------
# TOP ELECTRODE OVER n+ MATERIAL
ELECTRODE NAME = ANODE X.MIN = 0 X.MAX = 0.25 Y.MIN = -$ELECTRODE_THICKNESS \
Y.MAX = 0 Z.MIN = 0 Z.MAX = 0.25 MATERIAL = ALUMINUM

# BOTTOM ELECTRODE BELOW P+ MATERIAL
```

```
ELECTRODE NAME = CATHODE X.MIN = 0 X.MAX = $LENGTH Y.MIN = $DEVICE_THICKNESS \
Y.MAX = $BOTTOM_OF_DEVICE  Z.MIN = 0 Z.MAX = $WIDTH


# ---------------------- < DOPING PROFILE >------------------------
DOPING UNIFORM N.TYPE CONC = $SI_N_DOPING Y.MIN = 0 Y.MAX = $SI_N_THICKNESS \
                    X.MIN = 0 X.MAX = $LENGTH  Z.MIN = 0 Z.MAX = $WIDTH
DOPING UNIFORM P.TYPE CONC = $SI_P_DOPING Y.MIN = $SI_N_THICKNESS \
Y.MAX = $DEVICE_THICKNESS X.MIN = 0 X.MAX = $LENGTH  Z.MIN = 0 Z.MAX = $WIDTH


# ---------------------- < SAVE STRUCTURE >------------------------
STRUCTURE OUTFILE = SOLAR_CELL.STR


# ---------------------- < NUMERICAL ANALYSIS>------------------------
# ELECTRODE
MATERIAL MATERIAL=ALUMINUM IMAG.INDEX = 1 region = 4


# --------------------- < LIGHT SOURCE >------------------------------

BEAM NUM = 1 X.ORIGIN = $LIGHT_X Y.ORIGIN = -$LIGHT_Y Z.ORIGIN = $LIGHT_Z \
PHI = 90 THETA = 0 NX = 3 NZ = 3 BACK.REFL FRONT.REFL XMIN = -$LENGTH \
XMAX = $LENGTH ZMIN = -$WIDTH ZMAX = $WIDTH AM1.5
SOLVE B1 = 0.1
SAVE OUTFILE = SOLAR_CELL_WITH_BEAM.STR


# --------------------- < SPECIFY MODELS >------------------------------

# SAVE OPTICAL INTENSITY TO SOLUTION FILE
OUTPUT OPT.INT
MODELS CONMOB FLDMOB SRH
SOLVE


# --------------------- < ANALYSIS >------------------------------

# ---> SHORT CIRCUIT CURRENT (MAX CURRENT OF CATHODE CURRENT)
LOG OUTFILE = SHORT_CIRCUIT.LOG
SOLVE B1 = 1.5
SAVE OUTFILE = SOLAR_CELL_SHORT_CIRCUIT.STR

# ---> OPEN CIRCUIT VOLTAGE (MAX OF CATHODE INTERNAL VOLTAGE)
SOLVE INIT
CONTACT NAME = CATHODE CURRENT
SOLVE ICATHODE = 0 B1 = 1
SAVE OUTFILE = SOLAR_CELL_OPEN_CIRCUIT.STR


# ---> SPECTRAL EFFICIENCY WITH A MONOCROMATIC LIGHT SOURCE
BEAM NUM = 1 X.ORIGIN = $LIGHT_X Y.ORIGIN = -$LIGHT_Y Z.ORIGIN = $LIGHT_Z \
PHI = 90 THETA = 90
OUTPUT OPT.INT
MODELS CONMOB FLDMOB SRH PRINT

SOLVE INIT B1 = 0
LOG OUTFILE=SPECTRAL_EFFICIENCY.LOG
SOLVE B1 = 1 LAMBDA = 0.1
SOLVE B1 = 1 LAMBDA = 0.2
SOLVE B1 = 1 LAMBDA = 0.3
SOLVE B1 = 1 LAMBDA = 0.4
SOLVE B1 = 1 LAMBDA = 0.5
SOLVE B1 = 1 LAMBDA = 0.6
SOLVE B1 = 1 LAMBDA = 0.7
SOLVE B1 = 1 LAMBDA = 0.8
SOLVE B1 = 1 LAMBDA = 0.9
```